CONSTRAINING ELECTRON-CAPTURE RATES USING (d,^{2}He) REACTION IN INVERSE KINEMATICS

By

Zarif Mubassir Rahman

A DISSERTATION

Submitted to
Michigan State University
in partial fulfillment of the requirements
for the degree of

Physics—Doctor of Philosophy

2025

ABSTRACT

This thesis describes the use of the $(d,^2\mathrm{He})$ reaction in inverse kinematics with rare-isotope beams to constrain electron-capture rates, which are important for accurately simulating the heating and cooling processes in neutron star crusts. Electron-capture rates are calculated from Gamow-Teller (GT) strengths, which can be extracted experimentally in a model-independent way using charge-exchange reactions at intermediate energies. Following a successful pilot study with the $^{14}\mathrm{O}(d,^2\mathrm{He})$ and $^{13}\mathrm{N}(d,^2\mathrm{He})$ reactions in inverse kinematics using the Active-Target Time Projection Chamber with the S800 spectrometer at the Facility of Rare Isotope Beam, a second experiment was performed to investigate the $^{33}\mathrm{Al}(d,^2\mathrm{He})$ and $^{32}\mathrm{Mg}(d,^2\mathrm{He})$ reactions using an identical setup.

The nuclei ^{33}Al and ^{32}Mg are located in or near the $N = 20$ "island of inversion," a region where shell evolution leads to the inversion of the sd and pf shells. These nuclei play an important role in understanding the Urca mechanism in neutron star crusts, where rapid cycles between electron capture and β^- decay result in significant cooling due to strong neutrino emission. This thesis presents the experimental setup, data analysis, and results for the extracted GT strengths from these reactions. GT strengths were extracted for one state in the $^{33}\mathrm{Al}(d,^2\mathrm{He})$ reaction and two states in the $^{32}\mathrm{Mg}(d,^2\mathrm{He})$ reaction. The results provide evidence that the assumption of a closed-shell structure is invalid for ^{33}Al and ^{32}Mg. Although the uncertainties in the extracted GT strengths are large, there is reasonable agreement with shell-model calculations that include contributions from both the sd- and pf-shell configurations.

In addition to the experimental work, weak interaction rates and their impact on neutron star crusts were examined for nuclei in the sd and pf shells, for which precise shell-model calculations are already established. Neutron star crust simulations utilized three different sets of weak interaction rates: (1) rates derived solely from Quasiparticle Random Phase Approximation (QRPA) calculations, (2) shell-model rates for sd and pf shell nuclei, combined with QRPA rates for all other nuclei, and (3) experimental data for sd and pf shells when available, supplemented by shell-model calculations, with QRPA rates used for all other nuclei. The inclusion of experimental data for weak interaction rates leads to a suppression of both heating and cooling effects, and the

results align more closely with the rates from shell-model calculations than with those from QRPA calculations.

The results from this work underscore the importance of precise weak interaction rates for realistic neutron star modeling and demonstrate the effectiveness of the (d,^{2} He) reaction in inverse kinematics as a tool for extracting essential nuclear data.

ACKNOWLEDGEMENTS

Thank you, Remco and Simon.

TABLE OF CONTENTS

CHAPTER 1

BACKGROUND AND INTRODUCTION

1.1 Neutron Stars

Neutron stars stand out as the smallest and densest known stellar entities in our universe [1, 2]. Baade and Zwicky first proposed in 1934 that a neutron star could arise from the aftermath of a massive star ($\geq 8M_{\odot}$) explosion [3]. As a massive star exhausts its fuel generated through fusion in its core, it collapses under its own gravitational pressure and explodes into a supernova [4]. The cataclysmic eruption leaves behind a sphere of extremely dense matter. These remnants form what we call a neutron star that have radii in the order of 10 km and mass in the range of 1.17 to 2.35 solar masses [5, 6]. The neutron star is so dense that the atomic electrons collapse from their quantum orbits into the depths of the atomic nuclei fusing with protons to form neutrons. The neutrons are tightly packed in these conditions resulting in a high neutron degeneracy pressure due to the Pauli exclusion principle counteracting the force of gravity and supporting the neutron star against collapsing further [7].

Neutron stars can be divided into five major regions: atmosphere, ocean, crust, mantle and core. Fig. 1.1 shows different layers of a neutron star with approximate depth of each layer. The atmosphere is composed of normal atoms, but the temperature is not high enough for nuclear reactions to take place. The ocean, consisting of free electrons and ionized nuclei, is situated beneath the atmosphere and plays a role in transportation and release of thermal energy from the surface of the star. The atmosphere and the ocean are collectively referred to as the envelope. The crust forms the next region of the neutron star and is made of primarily ionized nuclei and electrons. The crust is sometimes divided into inner crust and outer crust based on the density. Between the crust and the core is a 1 km thick mantle composed primarily of neutrons, protons, and electrons [8]. This layer plays an important role in dynamics of the neutron star and serves as the transition between the crust and the core. The composition of the core is not well established, but it is speculated that the outer core is formed of nucleons, electrons, and muons whereas the inner core is formed of exotic particles such as hyperons, pions, or kaons [9]. Presence of a quark

condensate has also been suggested to be found in the center of a neutron star [1].

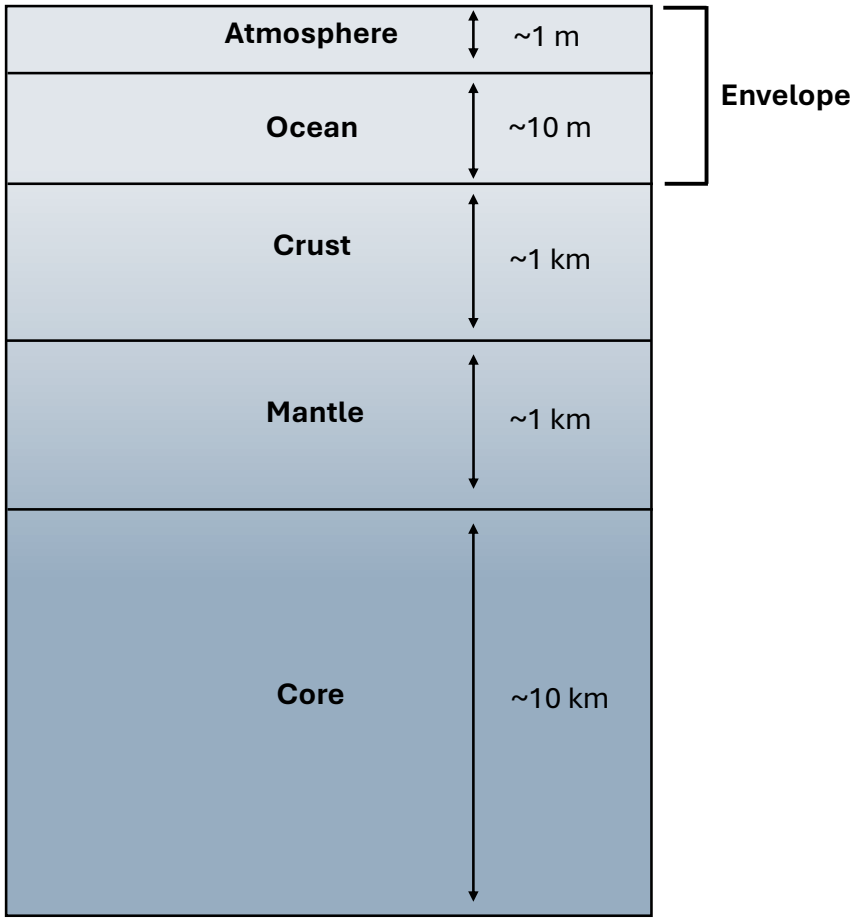

Figure 1.1 Regions of a neutron star with their approximate depths. Note that the depths of different layers are not drawn to scale.

Neutron stars have been observed both in isolation and in binary systems. In the binary systems, the neutron stars are in orbit with a companion star. The companion star can be any star, a black hole, or another neutron star. When the neutron star is in a binary system with a white dwarf or a main sequence star, it may start accreting mass. The mass transfer results in highly variable X-ray emissions [2]. Continual accretion can result in recurrent X-ray bursts that are periodic and rapidly increase in luminosity, peaking in the X-ray regime of the electromagnetic spectrum. There are also soft X-ray transients which emit X-rays for some time but then turn off for extended period of

times [10]. Instabilities in the accretion process are suggested as a reason for such emission. On the extreme end, there can also be superbursts which are long and more energetic X-ray bursts [11]. The surface temperature of these accreting neutron stars can be deduced from the observation of these X-ray photons.

Continuous accretion of matter onto a neutron star fuels thermonuclear burning on its surface. The ashes from these surface reactions are gradually compressed into the crust. At shallow depths in the crust, the Fermi energy (E_F) is smaller than the absolute value of the electron-capture (EC) $Q-$value, $|Q_{EC}|$, as illustrated by Fig. 1.2(a). In this region, the electron capture is energetically suppressed [12].

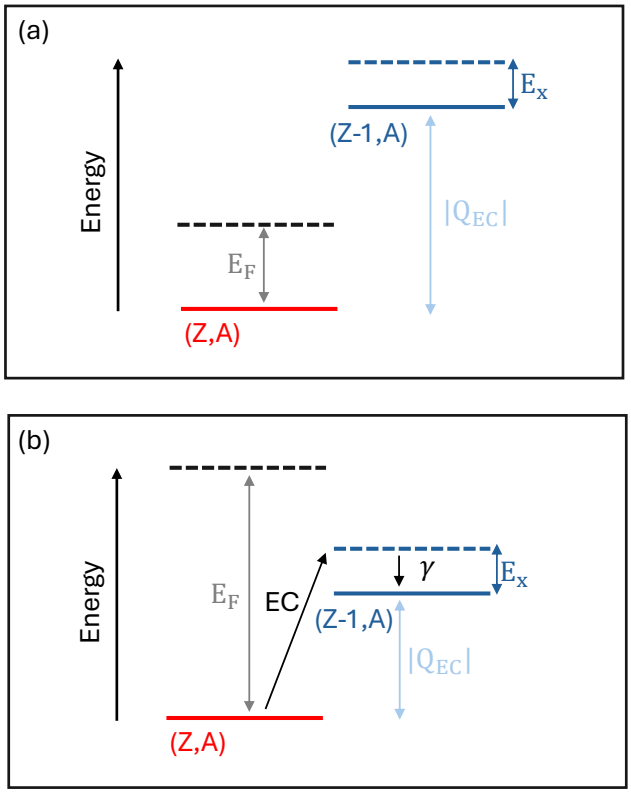

Figure 1.2 (a) Electron capture is suppressed at shallow depths because the reaction Q-value is higher than the available Fermi energy. (b) At greater depths, the higher Fermi energy allows electron capture, but the reverse β^- decay is not possible. If the Fermi energy is high enough, electron capture can also occur to excited states, which then deexcite by emitting γ-rays that locally heat the crust.

At greater depths, where E_F is significantly higher than $|Q_{EC}|$ (as shown in Fig. 1.2(b)), EC has

occurred, but the phase space for electron emission via β^- decay is blocked by degenerate electrons. If $E_F > |Q_{EC}| + E_x$, the first EC transition will occur for an excited state in the daughter nucleus. E_x is the excitation energy of the lowest state in the daughter nucleus for which EC is allowed. The subsequent de-excitation of this nucleus via γ-ray emission deposits energy locally, contributing to heating. Due to odd-even staggering in nuclear binding energy, odd-odd nuclei have lower $|Q_{EC}|$ values than even-even nuclei. Consequently, EC often proceeds in pairs for even-mass nuclei, as illustrated in Fig. 1.3. When E_F greatly exceeds the Q_{EC} of the reaction for the odd-odd nucleus in the second step, the energy difference is split between the escaping neutrino and heat deposition into the crust [13]. These two-step EC processes are significant sources of heat in the neutron star crust.

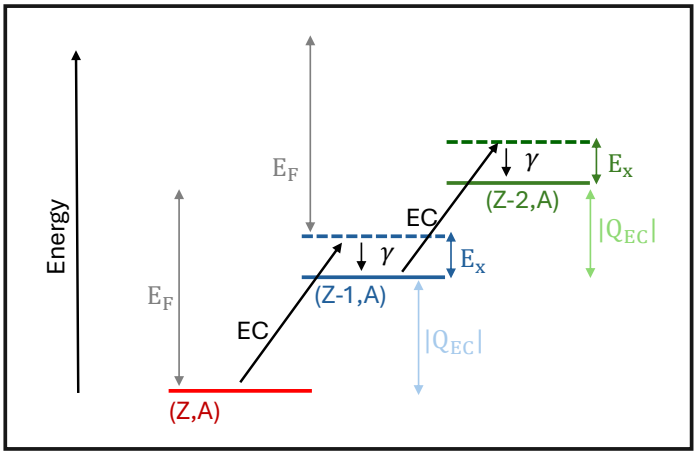

Figure 1.3 Two-step electron captures occur due to odd-even staggering in nuclear binding energy. Both reactions can proceed through excited states in the daughter nuclei, which deexcite by depositing heat locally. This makes two-step electron captures a significant heat source in neutron star crusts.

When $E_F \approx |Q_{EC}|$, β^- decay is not completely blocked at finite temperature. Therefore, both electron-capture and β^- decay can cycle back-and-forth via:

$$ {}^{A}_{Z}X + e^- -> {}^{A}_{Z-1}Y + \nu_e \tag{1.1} $$

$$ {}^{A}_{Z-1}Y -> {}^{A}_{Z}X + e^- + \nu_e \tag{1.2} $$

Both of these reactions emit neutrinos that carry away heat energy from the crust. The rapid cycling between EC and β^- decay, known as the Urca process [14], serves as a cooling mechanism for the star. The two nuclei involved in this process are known as the Urca pair. Fig. 1.4 illustrates schematic of the Urca process, where EC reaction occurs to the ground state of the daughter nucleus. However, if the E_F is sufficiently high, EC can also occur to a low-lying excited state.

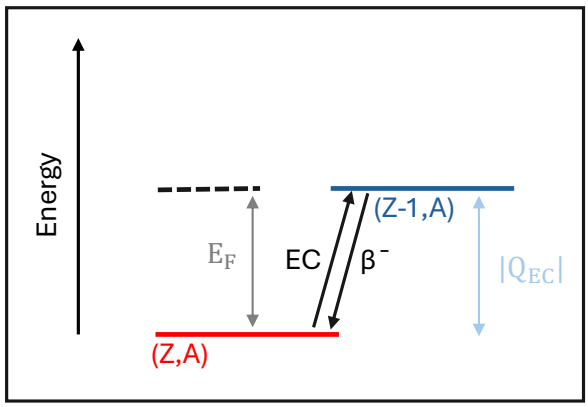

Figure 1.4 The Urca process occurs through cyclic electron capture and β^- decay at finite temperature, where the Fermi energy is close to the reaction Q-value. Both processes emit neutrinos, and their strong emission significantly contributes to neutron star crust cooling.

As EC in even-mass nuclei generally proceed in steps of two due to the odd-even staggering in the nuclear binding energy, the Urca process is inhibited. As a result, Urca cooling pairs are mostly formed by odd-mass nuclei as odd-even and even-odd nuclei allow for EC and β^- decay cycles at each step.

Heating and cooling in the neutron stars are governed by neutron-rich rare isotopes. It is important to have accurate EC rates for these isotopes in the neutron star crust simulation to determine the sources that cause change in heat energy. Nuclei in the $N = 20$ region, commonly known as the "island of inversion" are of particular interest for these simulations and calculations. Schatz et al. [12] used a full reaction network that included both EC and β^- decay rates to determine the Urca pairs that may play a significant role in the cooling of neutron stars. The reaction network incorporated weak interaction rates based on the Quasiparticle Random Phase Approximation (QRPA) formalism of Ref. [15]. However, Cole et al. [16] have shown that these

QRPA calculations are not well-suited to accurately predict transitions to individual low-lying final states. In contrast, shell-model calculations can provide more reliable results.

In this thesis, we build on the work of Cole et al., by using shell-model weak interaction rates for sd- and pf- shell nuclei in a neutron star crust simulation and compare results with the previous model. In addition, we extend our study to the so-called $N = 20$ "island of inversion" by experimentally studying two reactions: ^{33}Al(d,^{2}He)^{33}Mg and ^{32}Mg(d,^{2}He)^{32}Na and constraining EC rates in this region. The results are used to provide information for the development of new theoretical models and for understanding the uncertainties in state-of-the-art shell-model calculation models.

1.2 The Island of Inversion

The well-established nuclear shell model is a theoretical framework that aims to describe the nuclear structure in terms of shells much like the electron shells in atomic physics [17]. One fundamental difference between the atomic and nuclear shell model is that in an atom, the negatively charged electrons are bound by the Coulomb potential of the positively charged nucleus. However, in the nuclear shell model, the mean-field approximation describes the motion of individual nucleons as if they move independently within an average potential, which accounts for the collective influence of all other nucleons in the nucleus.

The foundation of the shell model comes from the observation of quantum magic numbers of nucleons, a phenomenon where certain numbers of nucleons are more tightly bound [18]. Relatively large energy gaps appear after the orbitals corresponding to the conventional magic numbers - 2, 8, 20, 28, 50, 82, and 126, as shown in Fig. 1.5 - for stable nuclei. However, far from the valley of stability, the shell structure evolves as neutrons are added to isotopic chains, sometimes leading to a reduction in the shell gap or inversion of shells.

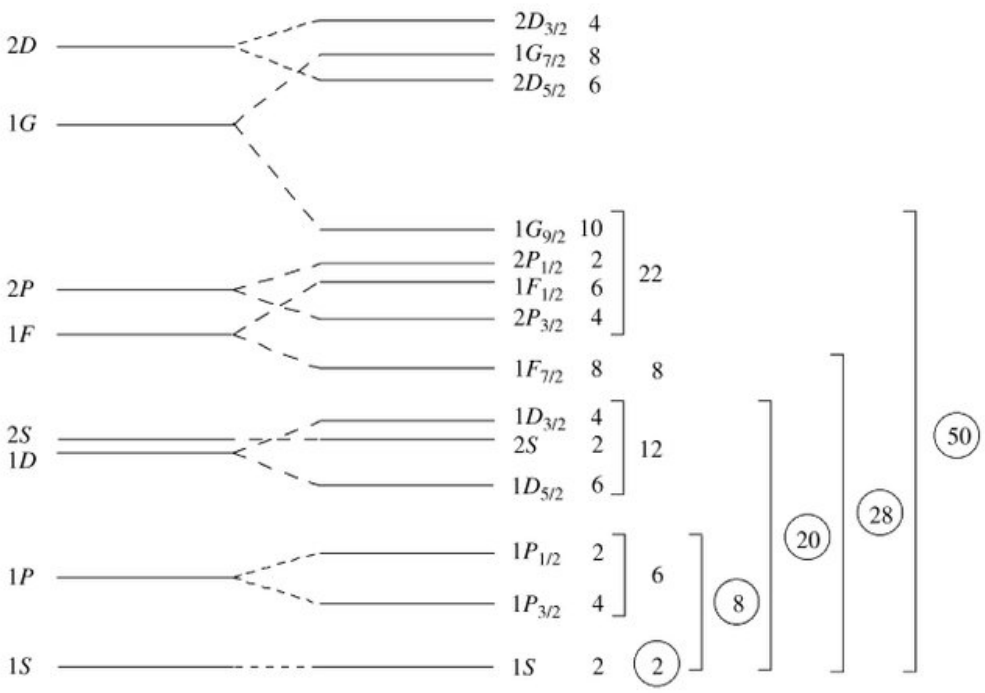

Figure 1.5 Low-lying energy levels shown for a single-particle shell model using Wood-Saxon plus spin-orbit potential. Figure has been taken from Ref. [19].

It has been well established that in the $N = 20$ region for $Z = 10 - 12$, as a result of the shell evolution, shell model orbitals can switch order for certain nuclei. The first observation of this phenomenon came from the mass measurement of ^{31}Na [20], which suggested the possibility of a breakdown in the magic number structure at $N = 20$. Theoretical calculations using both Hartree-Fock [21] and the shell model [22, 23, 24] reproduced these results by allowing neutron excitations from the sd shell to the pf shell, leading to a deformed ground-state configuration. Mass measurements in the $N = 28$ region have shown a similar pattern [25], where deformation of the ground state has also been predicted. Regions in the Segrè chart, a graphical representation of isotopes in a two-dimensional grid, where orbital inversions occur are referred to as islands of inversion. Fig. 1.6 shows the island of inversion in the $N = 20$ region in the Segrè chart. Note that the shores of the island of inversion are not firm; some of the surrounding nuclei are also impacted by the breaking of the $N = 20$ shell.

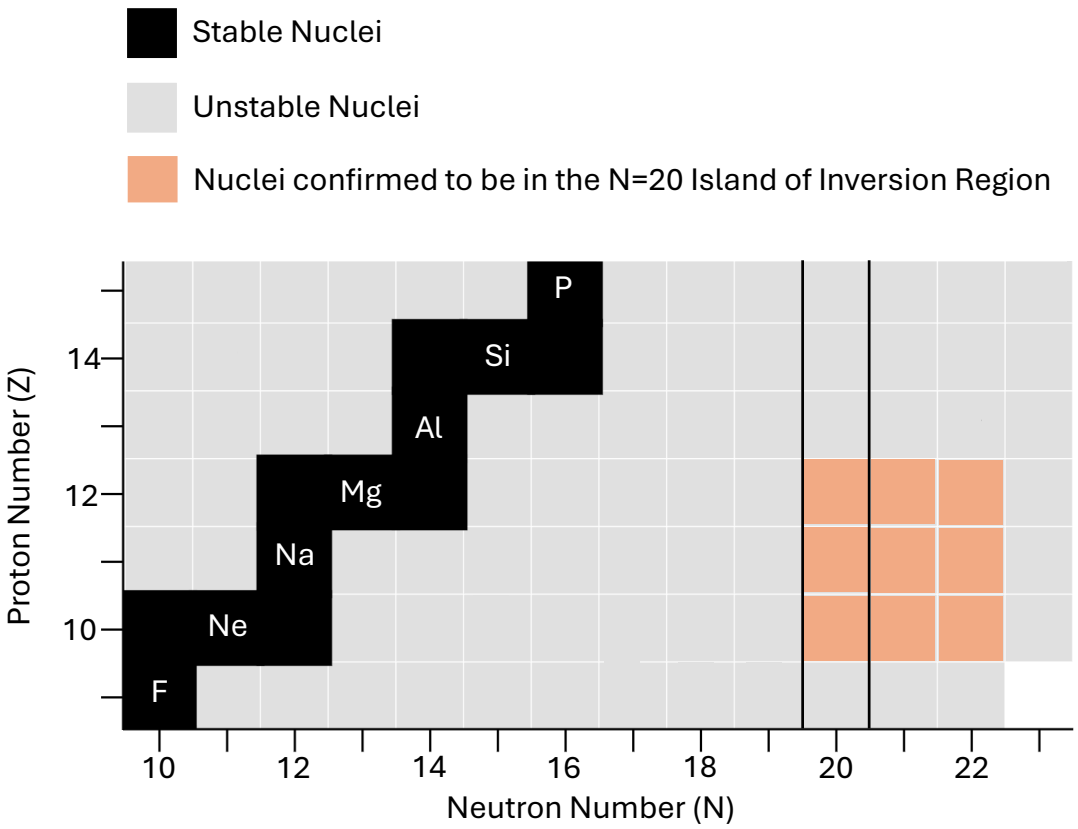

Figure 1.6 Island of inversion in the $N = 20$ region represented by the orange boxes in the Segrè chart.

The inversion occurs due to the properties of the nucleon-nucleon (NN) interaction, which can be further decomposed into three main terms: monopole, pairing, and all other components [26]. The largest contribution to the inversion of shells comes from the monopole component of the NN interaction induced by the tensor force. The monopole interaction induces shifts in the orbital energies, thereby triggering alterations in shell configurations. The energy shifts create varying energy gaps as Z and N change, with large energy gaps leading to the emergence of new magic numbers while potentially causing the disappearance of some traditional magic numbers. The pairing component involves interactions between protons and neutrons with total angular momentum $J^{\pi} = 0^{+}$. All other terms account for remaining contributions e.g., the quadrupole interaction. Fig. 1.7 shows the contribution to ground-state energy of Mg isotopes with even number N. Mg istopes with $N = 8 - 20$ were calculated using shell model in the *sd* model space

and for ^{32}Mg, the $sd - pf$ shell model space was also used. The USD Hamiltonian interaction is used for up to $N = 18$ and SDPF-M interaction was used for $N = 20$. Two calculations are shown for the latter: a full calculation and one in which excitations from the sd to pf shell are switched off. It can be clearly seen that the monopole contribution is larger for $N = 20$ compared to other neutron numbers. Fig. 1.7 shows the ground-state expectation values of these components for the Mg isotopes with even N values ranging from 8 to 20, calculated using a shell model in the sd shell for $^{20-30}$Mg, and in the $sd - pf$ shell for ^{32}Mg.

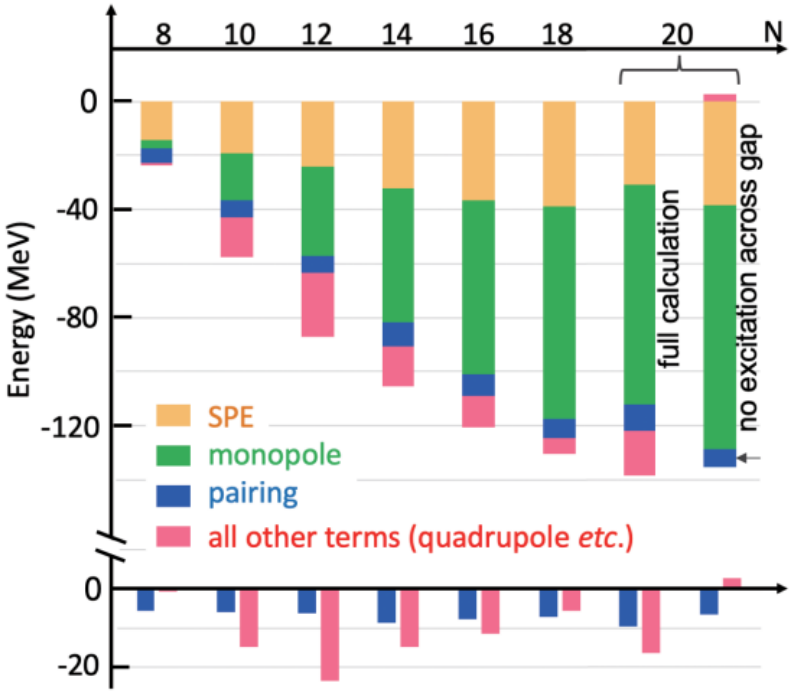

Figure 1.7 Contribution from NN interaction and single-particle energy (SPE) shown for the ground-state energy of Mg isotopes with even N. The NN interaction includes monopole, pairing, and other effects. The other effects are dominated by quadrupole interaction. Two calculations are shown for $N = 20$ - a full calculation with excitations across the gap to the pf shell and calculation without any such excitations. The calculation without across-gap excitations has a positive value for all other terms because of a repulsive contribution. Figure is taken from Ref. [27].

Several studies [28, 29, 30, 31, 32, 33, 34, 35] have reported presence of shape deformation around the $N = 20$ region for Z $\leq$ 12. Ref. [36] proposed 0p-0h and 2p-2h mixed configuration for ^{33}Al ground state based on shell-model calculations. Fig. 1.8(a) shows the "normal" configuration for ^{33}Al, which is a $N = 20$ nucleus. The normal configuration would mean that the sd shell

is full. However, in an “intruder" 2p-2h configuration, a pair of neutrons in the $N = 20$ shell closure is located in the pf shell, as illustrated in Fig. 1.8(b). Shell-model calculation shows that for many nuclei in this region, the intruder 2p-2h configuration has lower energies than normal configuration for nuclei with $20 \leq N \leq 22$ and $10 \leq Z \leq 12$. In fact, for ^{32}Mg, a sudden inversion has experimentally been observed between the states where the 2p-2h configuration is the ground state [37]. The inclusion of the pf shell extends the model beyond the closed shell structure, allowing the consideration of higher energy orbitals. This permits the possibility of higher-order excitations and interactions, which can enable Gamow-Teller (GT) transitions that were previously blocked in the closed-shell assumption.

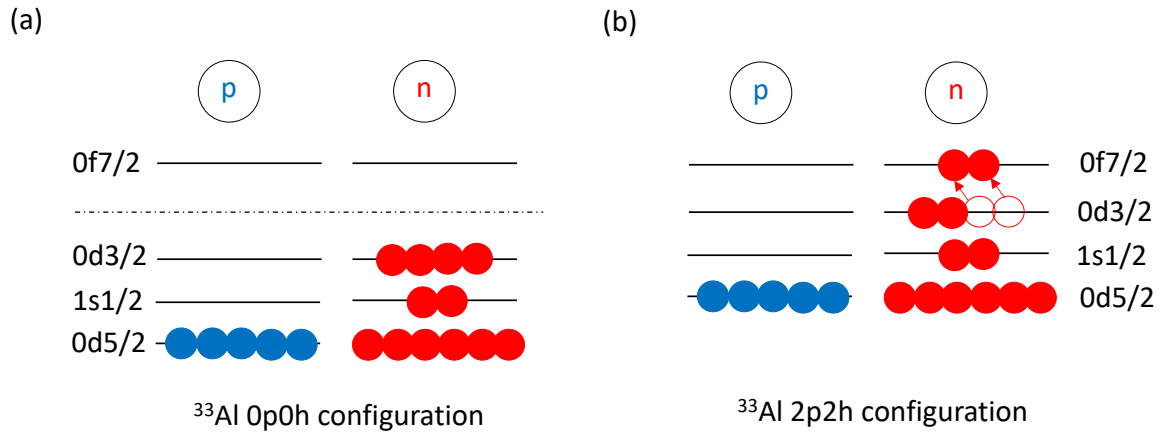

Figure 1.8 (a) The 0p-0h configuration for ^{33}Al, where no nucleons are excited across the energy gap (represented by the dashed line) between the sd and pf shells. In this configuration, all nucleons remain in the sd-shell orbitals. (b) The 2p-2h configuration, where two nucleons from the sd-shell are excited into the pf-shell, creating two particle-hole excitations. In this case, the shell gap has been reduced, making the 2p-2h configuration more energetically favorable. Although such configurations are typically associated with excited states, for certain nuclei in the $N = 20$ region, the 2p-2h configuration has been observed as the ground state.

The ground state of ^{33}Al is suggested to have a spin-parity of $(5/2)^+$ [38]. An allowed GT transition to ^{33}Mg would indicate that the ^{33}Al ground state does not exhibit a closed-shell structure and shows evidence of being in the $N = 20$ island of inversion. The first study of ^{33}Mg was conducted in 1984 through the β^- decay of ^{33}Na [39], but a detailed level scheme was not established until a 2001 investigation [40]. Despite multiple efforts to determine the spin-parity of

the ^{33}Mg ground state, it remains a subject of debate. A positive-parity state in ^{33}Mg could allow a GT transition from the ground state of ^{33}Al. Current evidence from hyperfine and nuclear magnetic resonances along with knockout reactions suggests that the spin-parity of the ^{33}Mg ground state is most likely $3/2^-$ [41, 42, 43]. However, the low $\log ft$ value of 5.6 established based on the study of β^- decay of ^{33}Mg suggested the possibility of a GT transition to a positive-parity $(5/2)^+$ ground state [36]. A state at 484 keV had been assigned a spin-parity of $(5/2)^-$ based on band assignments and Coulomb excitation data [44], but has been suggested to be $(3/2, 5/2)^+$ based on knockout reactions [43]. Theoretical calculations in Refs. [40] and [45] predict a spin-parity of $(3/2, 5/2)^+$ for a state at 705 keV, making it a candidate for a GT transition from the ^{33}Al ground state. In addition, Ref. [43] proposed spin-parities of $(1/2, 3/2)^-$ for the states at 1.24 MeV and 1.85 MeV.

A 2p-2h configuration has been experimentally observed for the ^{32}Mg ground state [37], and its spin-parity has been established as 0^+ [46]. While earlier studies suggested a spin-parity of $(3,4)^-$ for the ^{32}Na ground state [46], this assignment remains uncertain. Additionally, the excited states in ^{32}Na remain experimentally unconfirmed. The present study aims to provide new insights into these excited states, contributing to a deeper understanding of nuclear structure in the $N = 20$ region.

1.3 Electron-Capture Rates

Electron capture (EC) is a fundamental nuclear process mediated by the weak nuclear force. In an EC reaction, a nucleus captures an electron converting a proton into a neutron and produces an electron neutrino in the process. Through the process, the atomic number of the nucleus is reduced by 1, but the mass number is conserved. ECs play a vital role in various astrophysical processes, including the heating and cooling within neutron star crusts, as discussed earlier. It also plays an important role in the core-collapse phase of massive stars prior to a supernovae [47, 48, 49], final evolution of ONeMg cores in intermediate-mass stars [50, 51], nucleosynthesis of Type 1a supernovae, and many more [52, 53]. Several nuclei relevant to these astrophysical phenomena are neutron-rich and have negative Q-values, making direct study of these nuclei through EC experiments impossible. In addition, stellar ECs are different from laboratory EC as a result of

the high-temperature and/or high-density environment and, therefore, cannot usually be accessed through experiments directly. Additionally, in high-temperature stellar environments, transitions from excited states are possible. GT distributions obtained through experiments in the laboratory are typically limited to transitions from the ground state of the mother nucleus only. At relatively low temperatures and densities, EC rates are dominated by allowed GT transitions. At higher densities and temperatures, forbidden transitions also contribute [47, 48, 54, 55].

The following equation can be used to calculate EC rates [47]:

$$\lambda_{EC} = ln(2) \sum_{ij} f_{ij}(T, \rho, U_F) B(GT)_{ij}, \tag{1.3}$$

where $f(T, \rho, U_F)$ is the phase-space factor, which depends on the density (ρ), temperature (T), and chemical potential (U_F) and B(GT) is the GT strength. The rate is obtained by summing over the B(GT) distribution and is weighted by the phase-space factor. $(ft)_{ij}$ is related to B(GT) through the following relationship:

$$(ft)_{ij} = \frac{K}{g_A^2} \frac{1}{\mathrm{B(GT)}_{ij}} \tag{1.4}$$

where t is half-life of the transition $i \rightarrow j$, K is the weak interactions constant, g_A is the axial-vector coupling constant. K has the value of 6144 ± 2 s and g_A has the value of 1.2694 ± 0.0028 [56]. Additionally, ground-state $(ft)_{ij}$ in the EC direction can be calculated from the ground-state $(ft)_{ij}$ in the β^- direction using the following relationship:

$$(ft)_{\mathrm{EC}} = \frac{(ft)_\beta}{2J_\beta + 1} \cdot (2J_{\mathrm{EC}} + 1) \tag{1.5}$$

where J_{EC} and J_β are the spins for parent ground states.

For electrons, the phase space integral takes the following form [47]:

$$\sum_{ij} f_{ij}(T, \rho, U_F) = \int_{w_l}^{\infty} w^2 (q_R + w)^2 S_-(T, U_F(\rho)) dw, \tag{1.6}$$

where $w = \epsilon_e/m_e c^2$ and ϵ_e is total energy of the electron. The EC threshold energy is $w_l = |q_{g.s}|$ with $q_{g.s.} = Q_{g.s.}/m_e c^2$, where $Q_{g.s.} = m(A, Z, X) - m(A, Z-1, Y) - m_e c^2$ and m_N refers to the nuclear mass excess. q_R is obtained in the units of m_e from [47]:

$$q_R = Q_R/m_e c^2 = [E_{xj} - E_{xi} - Q_{g.s.}]/m_e c^2, \tag{1.7}$$

S_- is the Fermi-Dirac distribution function and can be given as the following:

$$S_- = \left(\exp\left(\frac{U - U_F}{kT}\right) + 1\right)^{-1} \tag{1.8}$$

where U is the kinetic energy and k is the Boltzmann constant. Since direct study of neutron-rich nuclei through EC is not feasible, an indirect method must be employed to investigate the GT transitions of excited states.

1.4 Charge-Exchange Reactions

Charge-exchange (CE) reactions provide an indirect method for extracting B(GT)s. Charge is transferred between the projectile and target, i.e. a neutron can be converted into a proton in the daughter nucleus, or vice versa. At intermediate beam energies ($E_{beam} \gtrsim 100$ MeV/A), CE reactions proceed through a single-step, direct reaction mediated by the strong nuclear force. As discussed below, by using CE reactions, GT transition strengths can be extracted, from which the EC rates are calculated (see Eq. 1.3).

CE reactions do not have a Q-value limitation, unlike EC or β^- decay, and they connect the same initial and final states as these processes. CE reactions in the (n, p) direction will involve the same parent and daughter nuclei as EC, as shown in Fig. 1.9. These reactions also share similar spin and isospin transfer operators [57]. In combination with a well established proportionality between B(GT) and CE cross sections [58] (see Sec. 1.4.1), CE reactions provide a valuable alternative to EC and β^- decay studies for the purpose of extracting B(GT). They reveal important information on transitions to states at excitation energies inaccessible through EC/β^- decay studies, which is important for astrophysical applications.

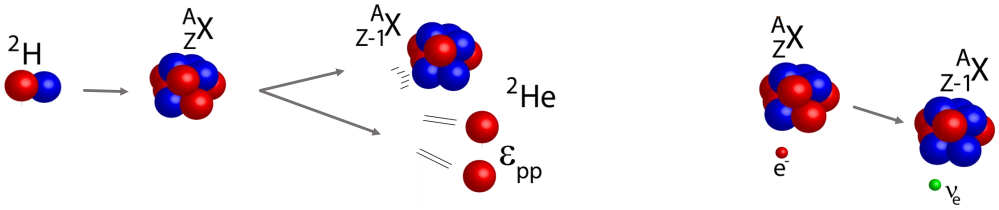

(a) Charge-Exchange Reaction (b) Electron Capture

Figure 1.9 Electron-capture and charge-exchange reactions are mediated by the weak force and strong force, respectively, but they connect the same initial and final states. (a) In the charge-exchange reaction shown using a (d,^{2}He) probe, a deuteron beam is used on a target resulting in recoiling nucleus with one less proton but same mass number. (b) An electron is captured by a nucleus and a proton is converted to a neutron releasing a neutrino and the mass number is conserved again.

CE reactions are characterized by an isospin transfer and are isovector transitions (ΔT = 1). Fermi (ΔS = 0) and GT (ΔS =1) transitions are differentiated by spin transfer and both can be studied with CE reactions. Both transitions see no change in angular momentum (ΔL = 0). Our interest lies in calculating EC rates that are dominated by GT transitions, characterized by the B(GT). Therefore, this work will focus only on GT transitions and the associated strength, B(GT).

1.4.1 Gamow-Teller Strength

The B(GT) can be experimentally extracted for both the (n, p) and (p, n) directions. GT transitions are described by the following operator:

$$O(GT) = g_A \sum_j \vec{\sigma}_j \tau_{\pm j}, \tag{1.9}$$

where σ represents the Pauli-spin matrix, and τ is the isospin transition matrix [57]. The following equation shows the relationship between the operator and the B(GT):

$$B(GT)_{\pm} = \frac{1}{2J+1} \left| \sum_j \langle \psi_F || \sigma_j \tau_j^{\pm} || \psi_I \rangle \right|^2 \tag{1.10}$$

where ψ_I and ψ_F are the wave functions of the initial and final nuclear states, respectively, and J is the total angular momentum of initial state.

As mentioned previously, the atomic number changes in charge-exchange reactions, whereas the mass number is conserved, which translates to a change in isospin projection, ΔT_z, of 1 or -1. The isospin projection of the target nucleus can be calculated by the following equation:

$$T_z = \frac{N - Z}{2} \tag{1.11}$$

For example, in the case of ^{32}Mg with $N = 20$ and $Z = 12$, the isospin projection is $T_z = 4$. In a (p, n)-type reaction ($\Delta T_z = -1$), the final nucleus becomes ^{32}Al with $N = 19$ and $Z = 13$, resulting in $T_z = 3$. Conversely, in an (n, p)-type reaction ($\Delta T_z = +1$), the final nucleus becomes ^{32}Na with N = 21 and Z = 11, leading to $T_z = 5$. For a parent nucleus in the ground state with isospin T_0, reactions in the (n, p) direction can populate states in the daughter nucleus with $T = T_0 + 1$, as this is the minimum allowed isospin for the residual nucleus at the new T_z. However, for reactions in the (p, n) direction, states with $T = T_0 - 1$, $T = T_0$, or $T = T_0 + 1$ can be populated.

Through a detailed investigation, Tadeucci et al. [58] established a proportional relationship between B(GT) and (p, n) cross-section at zero momentum transfer ($q = 0$):

$$\frac{d\sigma}{d\Omega}(q = 0) = \hat{\sigma}_{GT} B(GT), \tag{1.12}$$

where $\frac{d\sigma}{d\Omega}(q = 0)$ is the differential cross-section at zero momentum transfer ($q = 0$) and $\hat{\sigma}_{GT}$ is the unit cross-section. The $\hat{\sigma}_{GT}$ can be calibrated from transitions with known B(GT). In the Eikonal approximation, the $\hat{\sigma}_{GT}$ is a combination of three independent terms:

$$\hat{\sigma}_{GT} = K N^D |J_{\sigma\tau}|^2 \tag{1.13}$$

$K = \frac{E_i E_f k_f}{(\hbar^2 c^2 \pi) k_i}$ is a kinematical factor, where E_i and E_f are the reduced energies of incoming and outgoing channels, and k_i and k_f are the linear momenta of the projectile and ejectile, respectively. N^D is the distortion faction and $|J_{\sigma\tau}|^2$ is the volume integral of the central $\sigma\tau$ interaction.

The proportionality relationship between the CE differential cross-section and the B(GT) holds true under specific conditions: (i) the differential cross-section has to be extracted at $q = 0$ and (ii) intermediate beam energies ($E_{beam} \gtrsim 100$ MeV/u) are required to ensure a single step reaction

mechanism [59, 60]. The proportionality has shown to worsen for weaker transition strengths, caused by the interference between the transition amplitudes mediated by the $\sigma\tau$ and $T\tau$ (tensor-τ) components of the NN interaction [58, 61, 56].

The model-independent Ikeda sum-rule provides a relationship between the sum of B(GT) in either direction as follows [62]:

$$S(\beta^-) - S(\beta^+) = 3(N - Z), \tag{1.14}$$

where S(β^-) and S(β^+) are the summed B(GT)s in β^- and β^+ directions, respectively. Experimentally, only about 60% of the GT sum-rule strength is observed due to a phenomenon known as quenching [63, 64]. Several studies have established quenching for p, sd, and pf shells that are summarized in table 1.1:

Table 1.1 The quenching factors for p, sd, and pf shells. When applying the quenching factor to extract B(GT), the values from the table need to be squared. For example, for pf shell, the applied quenching factor should be $0.744^2 = 0.555$.

Region	Quenching Factor
p-shell	1-0.19 $\left(\frac{A}{16}^{0.35}\right)$ [65]
sd-shell	0.76 [66]
pf-shell	0.744 [67]

Several charge-exchange probes have been developed to extract B(GT) in the β^+ and β^- directions. In the β^+ direction, (n, p), $(d,^2\text{He})$, and $(t,^3\text{He})$ reactions have been primarily used to constrain EC rates. Experiments have primarily been performed in forward kinematics in which the target is the probed nucleus and the light particle serves as the beam, as illustrated in Fig. 1.10(a). The nuclei relevant for astrophysical studies are often unstable and short-lived that cannot be used as targets. As a result, the experiment has to be performed in inverse kinematics where the light particle is used as the target and the probed rare isotope is used as the beam as shown in Fig. 1.10(b). It is not feasible to make a sufficiently dense neutron target, so pursuing the (n, p) reaction in inverse kinematics is not realistic. Additionally, inverse reactions with light charged particles at $q \sim 0$

results in an ejectile that is emitted at very low kinetic energy (~ 1 MeV) and easily stops in solid target. The (^{7}Li,^{7}Be) reaction has been studied in inverse kinematics without the detection of ^{7}Be ejectile directly [68]. However, as the ^{7}Be ejectile is not detected, the measurement is limited to only relatively light nuclei (A<35) and excitation energies up to particle separation energies. The (d,^{2}He) reaction in inverse kinematics does not have the aforementioned limitations and is in principle a suitable tool to study rare isotopes across the nuclear chart. It was successfully used to study ^{14}O and ^{13}N to extract B(GT) in a pilot experiment at the National Superconducting Cyclotron Laboratory (NSCL) in 2020 [69, 70].

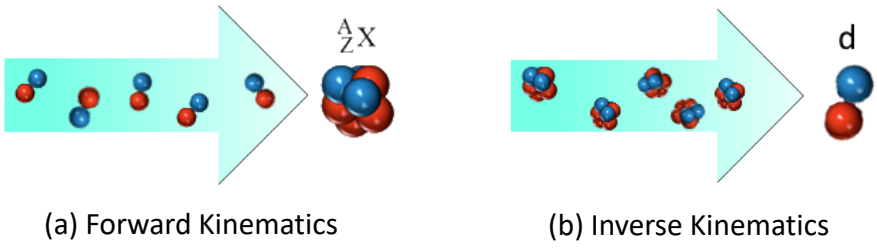

Figure 1.10 (a) In forward kinematics, the heavy isotope is used as the target and the light isotope which in this case is the deuteron is used as the beam. (b) In inverse kinematics, the unstable heavy isotope is used as the beam and impinged on the lighter isotope used as a target.

1.4.2 Application of (d,^{2}He) Probe in Inverse Kinematics

The (d,^{2}He) probe was first used at RIKEN for studies of light nuclei [71]. Using a deuteron beam energy of E_d = 260 MeV, the data demonstrated the one-step nature of the reaction and established a proportionality between B(GT) values and (d,^{2}He) cross-sections at 0°. A resolution of approximately 1 MeV was achieved in this study, primarily limited by the target thickness. The reaction probe was later successfully utilized at the Texas A&M Cyclotron Institute [72] and the Kernfysisch Versneller Instituut (KVI) [73]. At Texas A&M, three sd-shell nuclei and one pf-shell nucleus were investigated using a deuteron beam energy of E_d = 125.2 MeV, achieving a resolution of as low as 600 keV. At KVI, experiments conducted with a beam energy of E_d = 170 MeV achieved an excitation energy resolution of as low as 150 keV. The (d,^{2}He) reaction probe has been

well established in forward kinematics and is currently regarded as one of the most effective tools for studying B(GT)s in the β^+ direction.

The ^{2}He in the (d,^{2}He) reaction probe refers to a pair of unbound protons. The use of (d,^{2}He) probe requires the measurement of the two protons in order to reconstruct the ^{2}He particle. If the relative energy between the two protons (ϵ_{pp}) is small, it primarily has a $^1S_0$ configuration and contributions from higher partial waves are negligibly small [74]. The incident deuteron is predominantly in the $^3S_1$ state, so a pair of protons coupled to the $^1S_0$ state will ensure the reaction proceeds almost exclusively by spin transfer ($\Delta S = 1$). Thus, by constraining ϵ_{pp} to small values, it is possible to maximize the spin-transfer nature of the (d,^{2}He) reaction probe.

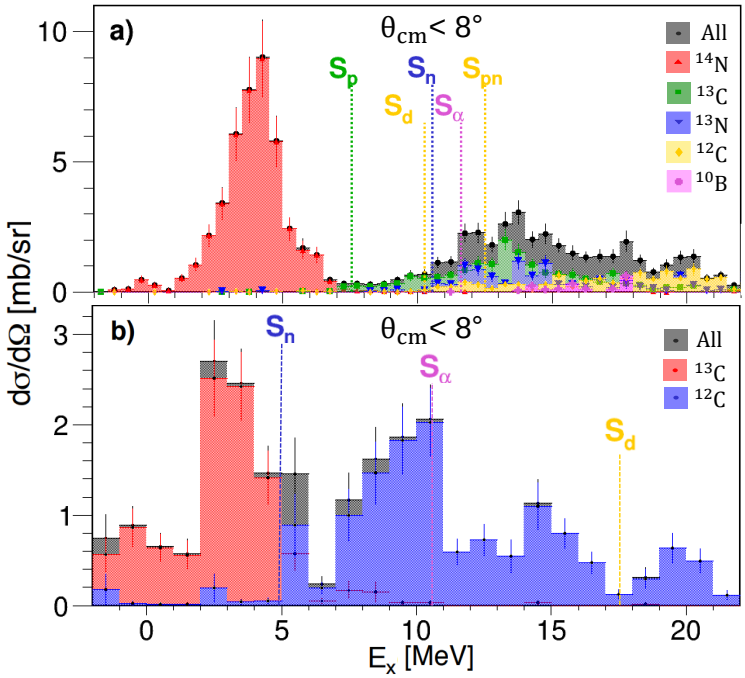

Figure 1.11 Differential cross-sections for the (a) ^{14}O(d,^{2}He) and (b) ^{13}N(d,^{2}He) reactions are depicted for $\theta_{\text{c.m.}} \leq 8°$. The dashed lines in the figure represent separation energy for different decay channels, while the different colors indicate which residual particle was detected in the S800, as labeled. Figure has been taken from Ref. [70].

The (d,^{2}He) probe was used in inverse kinematics in a pilot experiment in 2020 at NSCL to study rare isotopes [69, 70]. This experiment utilized the Active-Target Time Projection Chamber (AT-TPC) positioned at the target location of the S800 magnetic spectrometer. Figs. 1.11(a) and 1.11(b) show the differential cross-sections for for ^{14}O(d,^{2}He) and ^{13}N(d,^{2}He), respectively,

plotted as a function of their excitation energies obtained from the analysis of the two primary channels. Their decay products detected in the focal plane of the S800 were also analyzed to obtain the cross-sections up to high excitation energy.

For the ^{14}O channel, B(GT) values were determined up to an excitation energy of 22.5 MeV. The dominant peak at 3.95 MeV, shown in Fig. 1.11(a), has a known B(GT) of 2.73 from β-decay [75] and was used to determine the $\hat{\sigma}_{\mathrm{GT}}$. The B(GT) for the ground state in ^{14}N, resulting from ^{14}O β-decay, is known to be 2×10^{-4} [75, 76], which falls below the threshold for the proportionality between B(GT) and charge-exchange cross-sections [58, 77]. B(GT)s were obtained for the excitation energy range of 10–22.5 MeV, with a detailed discussion provided in Ref. [69].

For the ^{13}N channel, $\hat{\sigma}_{\mathrm{GT}}$ was determined using the peak at 3.68 MeV, shown in Fig. 1.11(b). The B(GT) for this state was extracted as 1.37 from the ^{13}C(^{3}He,t) experiment [78, 79]. The B(GT) for the ground state in ^{13}C was calculated to be 0.27 ± 0.07. Additionally, B(GT) values for the excitation energy regions 7-12 MeV and 13-17 MeV were determined to be 0.93 ± 0.05 and 0.19 ± 0.15, respectively. Further details of these results can be found in Ref. [70].

The results from both channels showed good agreement with previous experimental data and shell-model calculations. Following the successful implementation of the first (d,^{2}He) experiment in inverse kinematics, a second experiment using the same setup was conducted to investigate ^{33}Al and ^{32}Mg isotopes. The experimental and analytical methods for the second (d,^{2}He) experiment are similar to those of the first experiment and are detailed in Secs. 3 and 4.

CHAPTER 2

THEORETICAL CALCULATION

This chapter focuses on the theoretical calculations used in this thesis serving two main purposes: (1) to compare with experimental results in order to constrain and benchmark the theoretical models, and (2) to use these models to extract angular momentum components of interest from the experimental data- specifically, using theoretical cross-sections for transitions with different orbital angular momentum transfers to isolate the monopole ($\Delta L = 0$) contribution from the experimental differential cross-section through a multipole decomposition analysis (MDA) using the following equation [80, 81]:

$$\frac{d\sigma}{d\Omega} = a_0 \left.\frac{d\sigma}{d\Omega}\right|_{\Delta L=0} + a_1 \left.\frac{d\sigma}{d\Omega}\right|_{\Delta L=1} + a_2 \left.\frac{d\sigma}{d\Omega}\right|_{\Delta L=2} + \ldots \tag{2.1}$$

where a_0, a_1, and a_2 are fitting parameters. The left-hand side of this equation is the differential cross-section from the experimental data and on the right-hand side, the differential cross-sections are obtained from simulation for various ΔL contributions. By fitting data with simulation, we extract the $\Delta L = 0$ component of differential cross-section from experimental data.

This chapter will introduce the important computational tools used in the analysis: the shell-model code, NuShellX; the normal-mode code normod; and the Coupled-Channels Born Approximation code, accba. Rather than going into the detailed theoretical background of these codes, the focus will be on how they were applied in this study. For more detailed explanations of these tools, readers can refer to Ref. [82] for NuShellX, Ref. [83] for normod, and Ref. [84] for accba.

The theoretical differential cross-sections utilized in this analysis are obtained from accba. One-body transition densities (OBTDs) serve as inputs in the accba code and are obtained from NuShellX for $\Delta L = 0$ and $\Delta L = 2$ transitions and normod for $\Delta L = 1$ transitions. The OBTD connects the initial and final nuclear states through a one-body operator [85]. From the OBTDs, NuShellX also provides the shell-model predictions for the B(GT) distributions, which we compare our data with.

2.1 Shell-Model

The code NuShellX has been designed for performing shell-model calculations and is capable of handling Hamiltonian matrix calculations with very large basis dimensions. The formalism behind the code can be found in Ref. [82]. We used the shell-model code NuShellX to perform OBTD calculations for $\Delta L = 0$ and $\Delta L = 2$ transitions in the ^{33}Al(d,^{2}He)^{33}Mg and ^{32}Mg(d,^{2}He)^{32}Na reactions.

Conventional shell-model calculations often truncate configurations within the pf shell [86, 37, 87, 88], and therefore, these calculations cannot not include mixing between normal and intruder states [37, 88]. However, because the nuclei we are studying belong to the $N = 20$ island of inversion (see Sec. 1.2), Y. Utsuno used the $sdpf - m$ interaction within the $sdf7p3$ model space, which allows for mixing between these states. More information about the calculation of this interaction can be found in Ref. [89].

Fig. 2.1(a) and Fig. 2.1(b) show the shell-model predictions for the B(GT) transition from ^{33}Al to ^{33}Mg and ^{32}Mg to ^{32}Na, respectively. The shell-model calculations are performed by Y. Utsuno using the $sdpf - m$ interaction [90]. The model was truncated to include up to 6p-6h for ^{33}Mg and 6p-5h for ^{32}Na. The calculations were performed using the Lanczos strength function method. The shell-model calculations predict a strong GT state for both ^{33}Mg and ^{32}Na below 2 MeV.

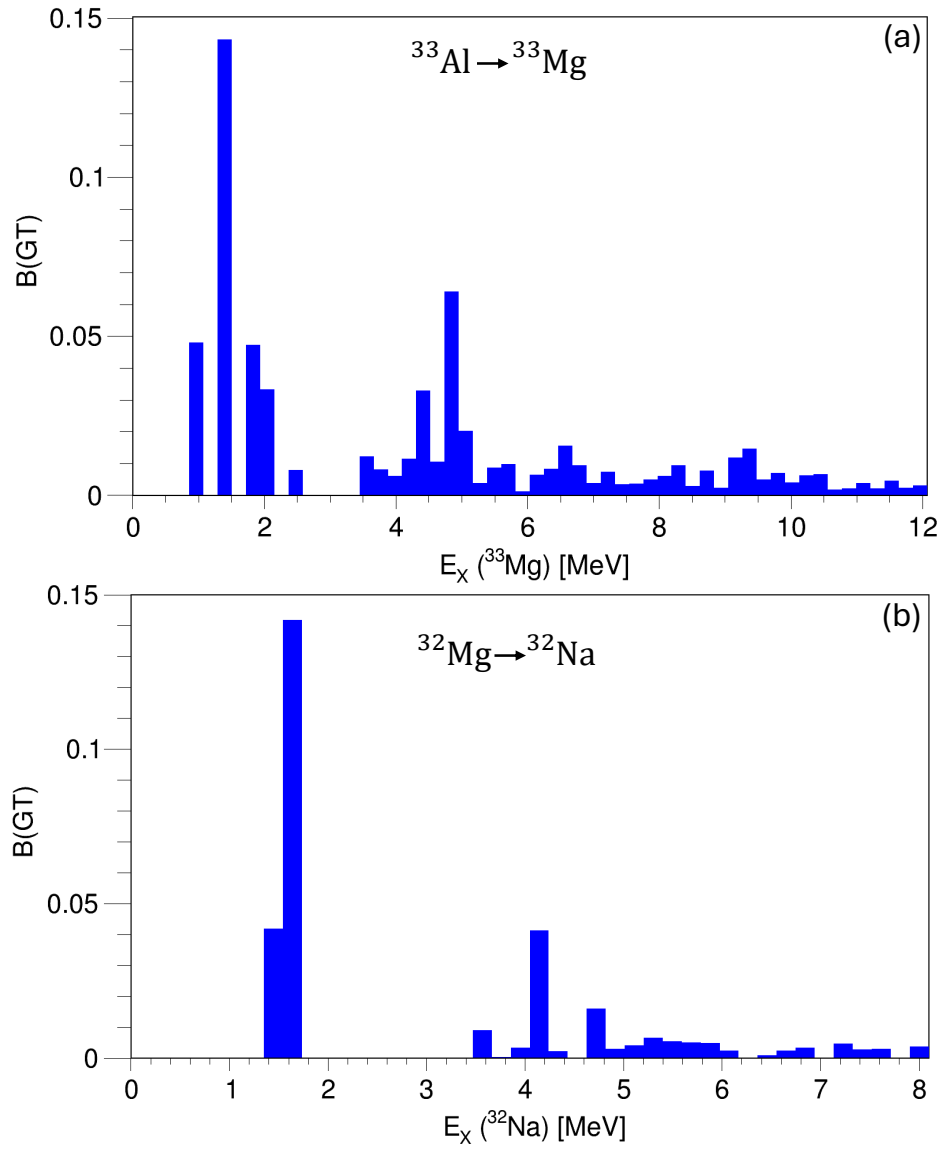

Figure 2.1 Shell-model calculation of the B(GT) for (a)^{33}Mg and (b)^{32}Na performed by Y. Utsuno using $sdpf - m$ interaction. The phenomenological quenching factor (see Section 1.4.1), which would reduce the strength to 55% of what is shown, has not been applied.

2.2 Normal-Mode calculation

For the dipole transitions involving a change in parity, the OBTD calculations were performed within the normal-mode formalism, as described in Ref. [83]. The NORMOD code [91] was utilized for these calculations. In the normal-mode formalism, OBTDs of 1p-1h transitions are constructed that are connected by a particular transition operator such that all these transitions interfere con-

structively and the transition strength is maximized. Therefore, the transition strength is associated with one excitation only, which serves as input for the ACCBA calculation. As we are only interested in the angular distribution of the dipole transition, which does not depend on the details of the wave functions, this relatively simple approach is sufficient.

For open-shell nuclei, occupation numbers must be properly considered. The states below the last closed shell are fully occupied, and the sum of the occupation numbers for the states above the last closed shell must match the number of available particles [92].

2.3 CCBA calculations

For calculating the differential cross sections, the Coupled-Channels Born Approximation was implemented using the code ACCBA. ACCBA has been written specifically for (d,^{2}He) reactions and has been well tested in forward-kinematics experiments. As noted previously, the ^{2}He system in these reactions is, in reality, a pair of protons, and the resulting three-body final state presents significant theoretical challenges.

In Ref. [93], Okamura et al. employed a one-step distorted-wave Born approximation (DWBA) to reproduce the low-lying discrete levels of the residual nucleus in (d,^{2}He) reactions. While the results were reasonably successful, some ambiguity remained due to the arbitrariness of the final scattering wave function, primarily caused by uncertainties in using a ^{2}He optical potential. To address this, Okamura et al. introduced a parameter-free method in Ref. [84], which employed an adiabatic approximation for treating the three-body dynamics. This approach simplifies the three-body dynamics by replacing the Hamiltonian of the two-proton system by the relative energy of the two protons. The coupling of ^{1}S and ^{1}D waves in the proton-proton ($p-p$) system is included in the calculation, along with contributions from the deuteron D-state. This coupling of partial waves is the basis of the "coupled channel" approach used in this analysis. This formulation resolves some of the ambiguities in previous treatments by providing a more robust framework for describing the final state interactions. This is especially important in (d,^{2}He) reactions where precise modeling of the final state significantly impacts the interpretation of experimental data. The ACCBA code calculates the differential cross-section as a function of the relative energies of the protons and

the center-of-mass scattering angle. This is crucial for performing acceptance corrections in the current work, as the cross-section depends sensitively on these variables.

2.3.1 Components of the ACCBA Code

This section describes the various inputs of the ACCBA code that need to be provided. The primary inputs of this code are comparable to that of other DWBA codes used for CE reactions at intermediate energies.

Fig. 2.2 shows a version of the code that was run for the ^{32}Mg(d,^{2}He) reaction. Lines 1-8 in Fig. 2.2 set the number of bins and integration limits for ϵ_{pp}. Line 10 is for the directory of the output file. Lines 13-46 are the skeleton of this code and need to be modified for each transition. All the numeric values in these lines are in free format and "\" can be used to write any comment. If any parameters are given after using a "\", it will be set to zero. Inputs for lines 13-46 are described below:

- **Line 13:** This line is for the title and is limited to 80 characters.
- **Line 14:** This line has three inputs: DWBA, point- projection, and triple-differential cross-section. For each of these parameters, there are only two options: T or F.
  - **DWBA**- Using "T" will treat the ^{2}He as a single particle and it is assumed that the optical potential acts on the center-of-mass of the $p-p$ system. Using "F" will generate the final scattering wave from proton optical potential by solving adiabatic coupled-channels equation.
  - **Point-projection**- "T" will treat the ^{2}He particle as a point particle and perform two-body calculation. "F" will treat the ^{2}He particle as unbound pair of protons and perform a three-body calculation.
  - **Triple differential cross-section**- "T" will provide a triple differential cross-section and "F" will generate double differential cross-section only.

- **Line 15:** This line sets the parameters for the angular distributions and also requires three inputs. The first and second input are the minimum and maximum angles, respectively, in degrees. The third input is the angular step size, also in degrees.

- **Line 16:** This line requires seven inputs detailing the reaction. The first three inputs are the mass number, atomic number, and spin of the target. As previously mentioned, ACCBA was written assuming forward kinematics, so the target is ^{32}Mg, as if it were in forward kinematics, even though for the experiment discussed here, ^{32}Mg was the beam. All cross-sections are calculated in the center-of-mass system making the distinction between target and beam irrelevant. The last four inputs in this line are of the residual nucleus (^{32}Na) spin, beam energy, Q value of the reaction, and the excitation energy of the final state. All the energy inputs in this line have to be in the units of MeV.

- **Line 17:** This line requires four inputs. The first parameter is the parity transfer. It can be either +1 or -1. The second parameter indicates the angular momentum transfer (ΔL). The third and fourth parameters are for the number of cases (n) with different total spin transfer (ΔJ) a calculation must be performed. For example, we can obtain results for $\Delta L = 0$ transition with the four parameters: +1 1 1 1 ($\Delta\pi$ ΔL n ΔJ).

- **Line 18:** This line consists of three parameters, which control details of the calculations. The first two parameters pertain to the integration range and the step size of the calculation over the distance between the target and the center-of-mass of $p-p$ system. The first parameter is the number of division for the range and must be even, and the second parameter is the step-size in units of fm. The third parameter on this line refers to the maximum number of partial waves in the DWBA calculation. This line can usually be left unchanged for $E_{beam} \sim 100$ MeV/μ.

- **Line 19:** This line consists of five parameters. The first three parameters pertain to the integration range over the relative coordinate in the $p-p$ system. The first two parameters, similar to those in line 18, are for the number of divisions and the step size. The number of

divisions is used for integrating the reaction T matrix, and the product of these two parameters determines the maximum radius for integration. The third parameter specifies the number of divisions for interpolation within the integration range. The product of this parameter with the first one is used in solving the $p-p$ scattering wave function. The last two parameters control whether the D-wave contribution should be included for the incident deuteron (which is the target in this experiment) and the outgoing $p-p$ system. Both parameters can take values of either 0 or 2. For the fourth and fifth parameters, 0 excludes the D-wave contribution from the deuteron and $p-p$ system, respectively, while 2 includes the D-wave contribution for both. This line can be left unchanged unless the inclusion of the D-wave contributions is desired.

- **Line 20:** This line provides three parameters related to ϵ_{pp}. The first parameter is for the step-size in ϵ_{pp} and the second and third parameters are for the integration minimum and maximum for ϵ_{pp}. The values for all these parameters are provided in MeV. The range of ϵ_{pp} was selected based on the detector system's acceptance for this experiment.

- **Lines 21-23:** The first line is for the optical potential for the deuteron-target and residual-proton systems taken from the Koning-Delaroche phenomenological potential [94], where the extended parametetrizations in the code TALYS were used [95]. Since in the adiabatic approximation, it is not possible to include the spin-orbital potential, the conventional optical potential was used to generate the incident-channel wave function [84].

  The eight parameters in line 21 are the potential depth (MeV), reduced radius (fm), and the diffuseness of the real potential (fm), depth of the volume (MeV), depth of the surface (MeV), the reduced radius (fm), and the diffuseness of the imaginary potential (fm), and the reduced radius of charge distribution (fm), respectively. Line 22 has three parameters: the depth (MeV), the reduced radius (fm), and the diffuseness (fm) of the spin-potential orbital. If the first parameter in line 14 is chosen as F, the optical potential must not include the spin-orbit part of the potential. The eight parameters in line 23 are the same ones as line 21, but for the

proton optical potential.

- **Lines 24-30:** These are the parameters of the Love-Franey effective nucleon-nucleon interaction based on nucleon-nucleon scattering observables. [60, 96].

- **Line 31:** This line details the parameters used for the potentials, which are used to generate the single-particle wave functions. The four parameters are the reduced radius (fm) and diffuseness (fm) of the single-particle potential, depth of the spin-orbit part of the potential (MeV), and the reduced radius of the charge distribution (fm). This line can be left unchanged.

- **Lines 32-38:** These lines provide the single-particle wave functions for the reaction. Each line has four parameters. The first parameter specifies the orbit and consists of four values. The first value denotes whether it is a neutron or proton ('n' for neutron and 'p' for proton), the second value provides the number of nodes of the wave function (starts at 0), the third value is for the orbital angular momentum, and the last value is for the total angular momentum expressed in fraction. On line 32, 'p0d5/2' corresponds to n=0, l=2, and j=5/2 orbit for the proton. The second parameters in these lines can either be 'V' or 'E'. 'V' implies the function is generated for fixed potential depth, V_0, and 'E' implies the wave function is generated by fixing the binding energy (BE) and varying the depth. We selected a fixed potential depth of 50 MeV for the system although using the "E" option did not alter the results. Since the potential depth is fixed, the fourth parameter becomes irrelevant in this case.

- **Lines 39-46:** These lines provide the one-body transition densities, which contain essential information that connect the initial and final states by the action of one-body operators. Of the three parameters, the first two are the orbits of the hole and the particle, respectively, and are written in the same manner as mentioned before. The last parameter is the OBTD. The value for these parameters are also obtained from the shell-model calculation using NuShellX.

```
#! /bin/bash

NeppBins="30"

for ((eppBin=0; eppBin<$NeppBins; eppBin++)) ; do

low=`echo "scale=3; 0.250*$eppBin" | bc`
up=`echo "scale=3; 0.250*($eppBin+1)" | bc`

file="output_ls_dl2/out$eppBin.dat"

grep -v '^ *#' <<EOF | ../../accba
32Mg(d,2He)32Na[1+;Ex=1.37] @ 173.2MeV
  F  F  F
  0  20  0.5
 32  12  0.0  1.0  173.2   -20.9  1.37
 +1 2 1 1
 300 0.05 150
  96 0.20 5 0 0
  10  $low $up
 56.81 1.176 0.673 16.975 3.845 1.292 0.537 1.307    /d+proj pot
  1.43 0.982 0.590
 31.85 1.176 0.673 9.09 2.63 1.292 0.535 1.307    /p + ejec pot
  1 1 1 1 3  3.21 0.71  397.50  2.5  -1720.00  4.00 / real central direct
  1 1 1 2 2             107.50  2.5  -126.10   4.00 / imag central direct
  1 1 3 1 4  58.2000 1.429  -377.400  1.818  2361.00  2.5  -15600.  4.0
  1 1 3 2 4  10.24   1.429  -115.900  1.818  844.6    2.5  -5897.0  4.0
  1 1 2 1 1  52.51  0 / real central exchange
  1 1 2 2 1 -29.88  0 / imag central exchange
 -1 /
 1.25 0.66 6 1.3
 'p0d5/2'   V   50.00   -18.009
 'p0d3/2'   V   50.00   -11.812
 'p1s1/2'   V   50.00   -14.514
 'n0d5/2'   V   50.00   -11.418
 'n0d3/2'   V   50.00   -5.550
 'n1s1/2'   V   50.00   -8.169
 'end' /
 'p0d5/2' 'n0d5/2'  0.01606
 'p0d5/2' 'n0d3/2'  -0.03801
 'p0d3/2' 'n0d5/2'  -0.16220
 'p0d3/2' 'n0d3/2'  0.04943
 'p0d3/2' 'n1s1/2'  -0.02407
 'p1s1/2' 'n0d3/2'  -0.05622
 'p1s1/2' 'n1s1/2'  0.03484
 'end' /
EOF
cp output.dat "$file"
rm output.dat
done
rm -f trip*.dat


exit
```

Figure 2.2 Input file for ACCBA.

2.3.2 Application of the ACCBA code

For the MDA, we used angular distributions for transitions with angular momentum transfer $\Delta L = 0, \Delta L = 1$, and $\Delta L = 2$. The input shown in Fig. 2.2 was used to obtain the theoretical cross section for the $\Delta L = 2$ transition in the ^{32}Mg(d,^{2}He) reaction. We ran the ACCBA code for the $\Delta L = 0$ and $\Delta L = 1$ transitions for ^{32}Mg(d,^{2}He) reaction after making the necessary modifications in the other inputs. Fig. 2.3 shows the differential cross-section calculated in the ACCBA code for the $\Delta L = 0$, 1, and 2 transitions of the ^{32}Mg(d,^{2}He)^{32}Na reaction at one particular excitation energy. From the ACCBA calculations, we observed a forward-peaking behavior for the $\Delta L = 0$ transition. The $\Delta L = 1$ transition showed a peak between 4° and 5°, while the angular distribution for the $\Delta L = 2$ transition appeared largely flat over the angular range covered. We repeated the same steps for the $\Delta L = 0$, 1, and 2 transitions for the ^{33}Al(d,^{2}He)^{33}Mg reaction.

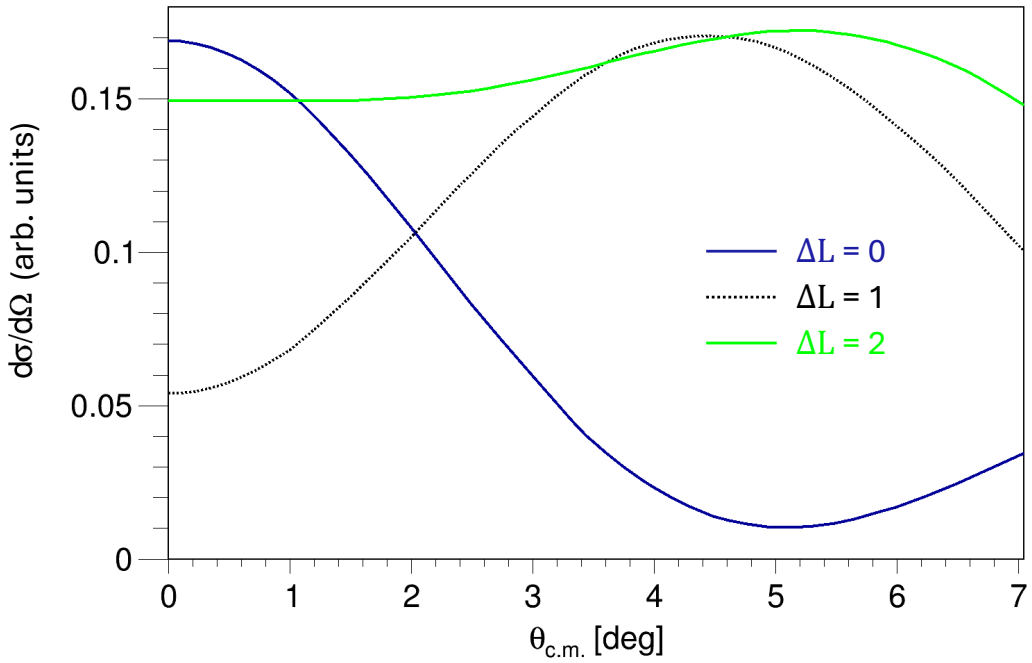

Figure 2.3 The differential cross-section obtained from ACCBA code for $\Delta L = 0$, ΔL =1, and ΔL = 2 components for the ^{32}Mg(d,^{2}He)^{32}Na reaction.

CHAPTER 3

EXPERIMENTAL SETUP AND PROPERTIES

The ^{33}Al, ^{32}Mg(d,^{2}He) experiment in inverse kinematics was performed at the Facility of Rare Isotope Beam (FRIB) at Michigan State University. This experiment was performed after the successful execution of the ^{14}O, ^{13}N(d,^{2}He) experiment [69, 70] at the NSCL at Michigan State University to study B(GT) distribution in the β^+ direction. The experimental setups for both the (d,^{2}He) experiments were identical.

3.1 Beam Production

A cocktail beam composed of primarily ^{33}Al (71%) and ^{32}Mg (22%), with minor quantities of other contaminants, was produced from a 150 MeV/u ^{48}Ca primary beam at FRIB impinged on a ^{12}C production target with a thickness of 5.0 mm. Two aluminum wedges with thicknesses of 1.5 and 2.8 mm were inserted into the Advanced Rare Isotope Separator (ARIS) fragment separator [97] to purify the components of the beam [98]. The beams were sent to the S800 mangnetic spectrometer [99], located in the S3 vault at FRIB, with a rigidity of 3.68 Tm. The ^{33}Al and ^{32}Mg beams had energies of 96.5 MeV/u and 88 MeV/u, respectively. The beam intensities used for this experiment were between 100 kpps and 140 kpps. During the experiment, the beam intensity was monitored in a scintillator placed at the object which is at the entrance of the beamline towards the S800. However, the transmission from the object scintillator to the AT-TPC was not 100%. The transmission of the beam to the AT-TPC was measured by comparing the event rate in the object scintillator to the event rate in the S800 focal plane scintillator when delivering the beam all the way to the S800 focal plane (unreacted beam setting). Since the acceptance of the S800 is large compared to that of the beamline from the object scintillator to the AT-TPC, this provides an accurate estimate of the transmission, which was determined to be 31.2%.

3.1.1 ARIS

The A1900 fragment separator [98] was used for the first (d,^{2}He) experiment, but ARIS was used for the second (d,^{2}He) experiment described in this work. ARIS has been designed to have a

large acceptance and transmission along with high suppression for undesired contaminants. This allows ARIS to provide high-intensity rare-isotope beams with desired purities. This fragment separator works in three stages (see Fig. 3.1). The first stage of the ARIS fragment separator, known as the preseparator, receives the beam from the production target and performs an initial separation of desired fragments from contaminants, delivering the rare-isotope beam to the second stage for further purification. This stage vertically bends the beam from the underground primary beamline to the above-ground levels of stages 2 and 3, using superferric magnetic dipoles for bending and magnetic quadrupoles for focusing, with higher-order magnetic elements correcting image aberrations. In stage 2, the beam undergoes horizontal separation and purification, where magnetic fields and a momentum-loss achromatic technique further separate fragments by mass-to-charge ratio, aided by a wedge degrader that compresses the momentum spread. Finally, in stage 3, a slit system in the focal plane reduces unwanted beam components, ensuring that only the rare-isotope beams of interest reach the experimental area with high purity.

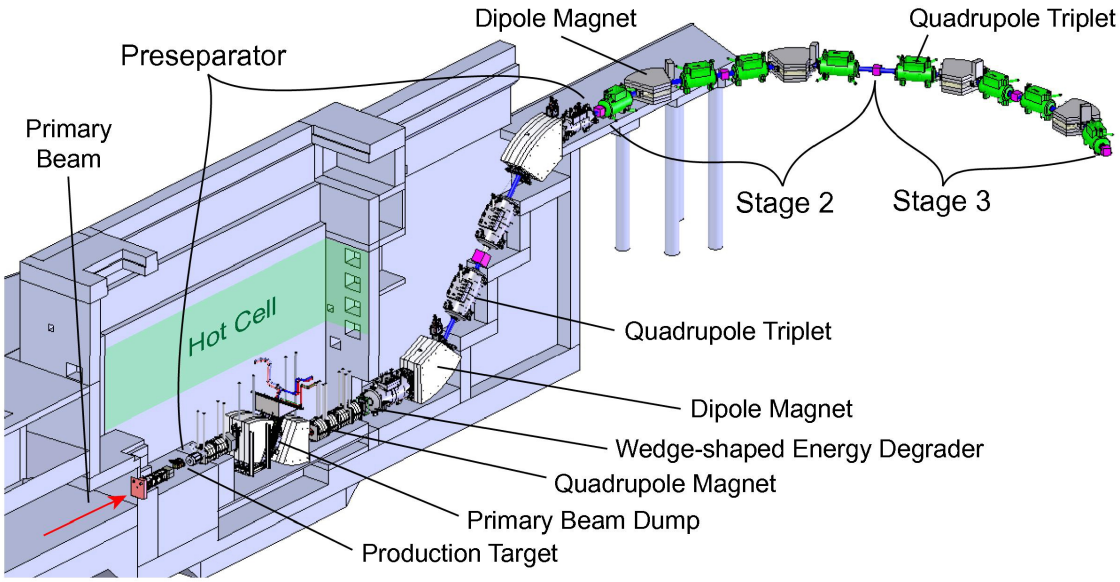

Figure 3.1 Schematic layout of ARIS consisting of three stages. The preseparator stage takes place underground whereas the second and third stage take place at ground. Figure has been taken from [97].

3.2 S800 Magnetic Spectrometer

The beam is transported to the S3 experimental vault through the transfer line after selection of the cocktail beam in the fragment separator. The S800 spectrometer and analysis line are located in the S3 vault (see Fig. 3.2). The S800 has two dipole and two quadrupole magnets that direct the reaction products towards the focal plane of the S800.

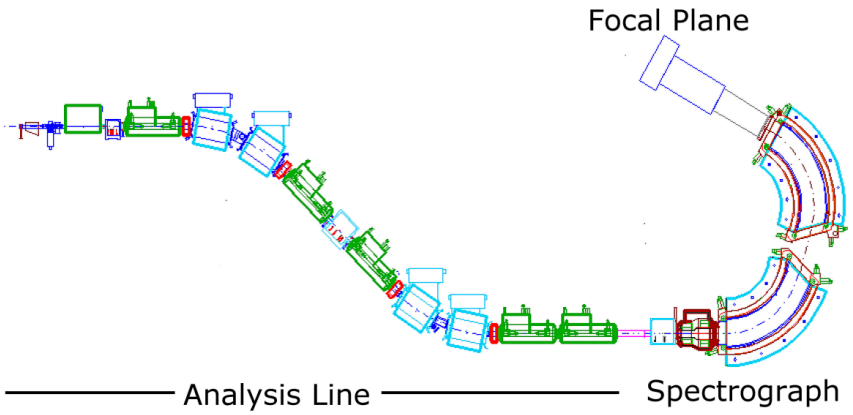

Figure 3.2 Schematic layout of the S800 analysis line and spectrometer in the S3 vault at FRIB. Figure adapted from [99].

The focal plane of the spectrograph has a number of detectors, shown in Fig 3.3, that are used for determining hit position, angle, energy loss, and time-of-flight (ToF). The momentum, scattering angle, and particle identity are determined from these parameters.

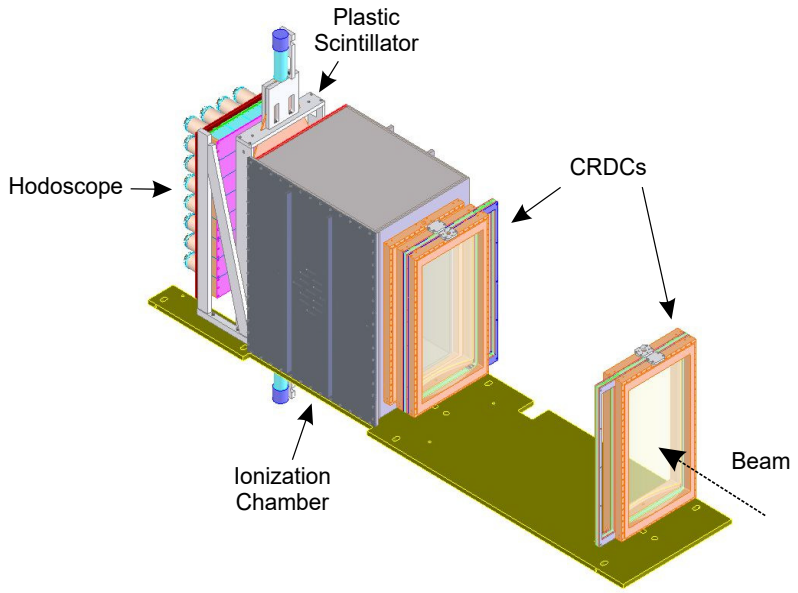

Figure 3.3 Schematic of the S800 analysis line and spectrometer in the S3 vault at FRIB. Figure has been taken from [100].

At the focal plane, there are two Cathode Readout Drift Chambers (CRDC) that are used for measuring the vertical and horizontal positions and angles of the fragments at the focal plane. The CRDCs consist of an active area of 60 cm in the dispersive direction by 30 cm in the non-dispersive direction [99]. The first CRDC is placed at the nominal optical focal plane and the second CRDC is located downstream separated from the first one by 1073 mm [101]. They are filled with 20% isobutane and 80% carbon tetrafluoride. Particles passing through the CRDCs ionize the gas mixture and the free electrons drift towards the cathode pads along the dispersive (x) axis. The image charge distribution on the pads allows determination of the dispersive position, as shown on Fig. 3.4. The drift time of the electrons, obtained from the difference between the S800 DAQ trigger time and the CRDC anode signal, provide information regarding the non-dispersive (y) position. The dispersive and non-dispersive angle measurements are obtained by combining the position measurements in the two CRDCs.

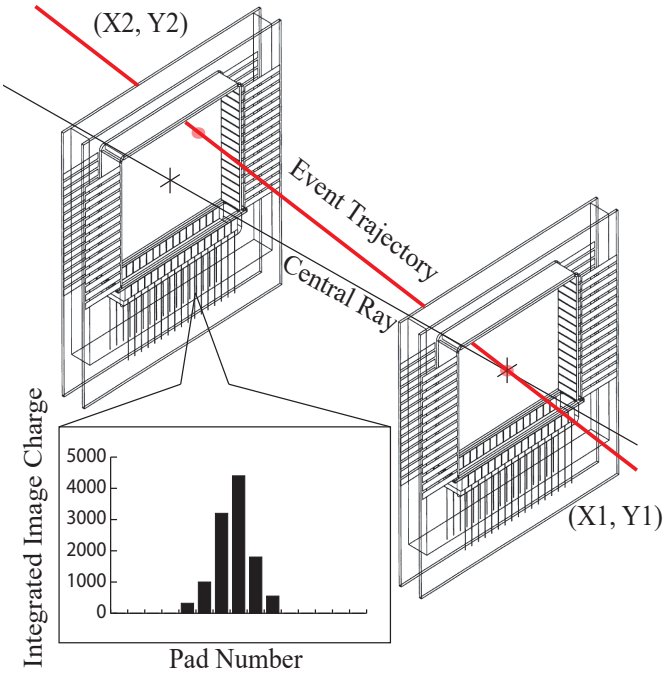

Figure 3.4 Schematic of the two CRDCs with the inset showing integrated image charge detected by the pads. An example event trajectory through the detectors is also shown. Figure was taken from Ref. [102].

.

A multi-segmented ionization chamber, filled with 90% argon and 10% methane, is placed after the CRDCs. The energy loss of the particles passing through the chamber allows for the indirect measurement of atomic number. The energy loss is proportional to the square of the charge of the particle according to the Bethe-Bloch formula [103]:

$$\frac{dE}{dx} = \frac{4\pi e^4 Z^2}{m_0 v^2} n_{abs} z_{abs} \left(\ln \frac{2m_0 v^2}{I} - \ln\left(1 - \frac{v^2}{c^2}\right) - \frac{v^2}{c^2} \right), \tag{3.1}$$

where Z is the charge of the incident particle. n_{abs}, z_{abs}, and I are the number density, atomic number, and average ionization potential of the absorbing material, respectively, m_0 is the electron's rest mass, and v is the velocity of the incident particle. Followed by the ionization chamber is a 3-mm thick plastic scintillator that provides the trigger for the S800 data acquisition system and is also used for particle identification by ToF measurement [99]. There is also a hodoscope at the focal plane of the S800 that measures the total kinetic energy of the ejectiles to identify different

charge states, but it was not used for this experiment.

3.3 Active-Target Time Projection Chamber

The active-target mode in Time Projection Chambers (TPC) are ideal for experiments with rare-isotope beams in inverse kinematics as the gas in the TPC serves as the tracking medium and the target with large solid-angle coverage and low-energy detection thresholds. The AT-TPC at FRIB has a cylindrical geometry with a length of 100 cm and a diameter of 50 cm [104]. The gas volume is enclosed by a field cage. A 3 cm diameter hole is made in the pad plane to allow the beam to enter. The active region of the AT-TPC is separated from the vacuum of the beam line and spectrometer by 12 um thick window. The AT-TPC has a symmetrical geometry and the beam comes in perpendicular to the pad plane on the side.

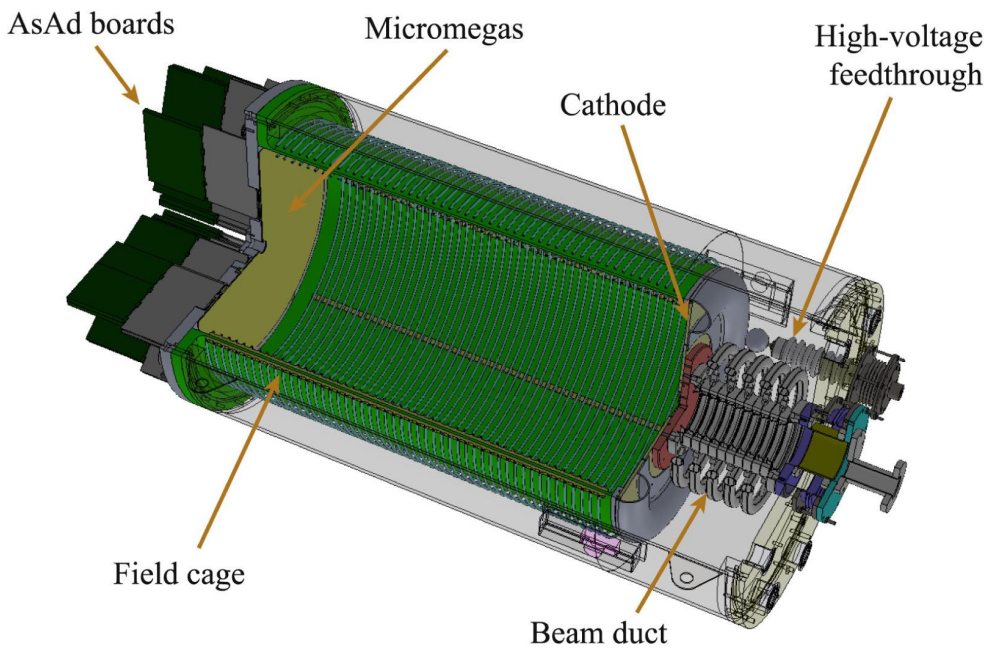

Figure 3.5 Mechanical drawing of the Active-Target Time Projection Chamber (AT-TPC) showing all the major components. Figure is taken from Ref. [104].

.

The charged particles from the beam pass through the chamber, stripping electrons from the gas and ionizing it. The electrons are then driven towards the anode end of the detector by a uniform

electric field applied along the beam axis. There is a sensory plane at the anode end consisting of 10240 triangular conductive pads. The plane is arranged in a hexagonal inner region of small pads with 0.5 cm triangular height surrounded by outer region of large pads with 1 cm triangular height. A Micromegas detector is installed on the pad plane that consists of a very fine conductive mesh. The mesh is biased with respect to the electrodes to create a relatively large electric field between the mesh and the pads. This divides the detector into a large drift region above the mesh and a small multiplication region below the mesh. When the electrons from the ionized gas pass the mesh and enter the multiplication region, the much larger electric field there cause the formation of an electron avalanche, amplifying the signal.

The AT-TPC uses advanced digital electronics developed by the Generic Electronics for Time Projection Chambers (GET) collaboration [105], providing a fully digital data acquisition (DAQ) system capable of digitizing and recording traces for all 10,240 channels in the detector. The system is organized into a hierarchy of modules, with the base level consisting of custom application-specific integrated circuits (ASICs) known as AGETs (ASIC for GET). An ASIC (Application-Specific Integrated Circuit) is a custom-designed chip tailored for specific applications. The AGET amplifies incoming signals using a variable-gain charge-sensitive preamplifier and performs pole-zero correction. Each AGET reads out 64 physics channels from the detector.

Each AsAd (ASIC Support and Analog-to-Digital Conversion) board houses four AGETs and includes a four-channel, 12-bit analog-to-digital converter (ADC) that digitizes sample outputs from the AGET chips and transmits the data through a serial link [106] when a trigger is issued. These AsAd boards are connected directly to the sensor plane to minimize the distance that analog signals must travel before being digitized, reducing capacitance and potential noise in the data. Ten Concentration Boards (CoBos) in the AT-TPC are each connected to four AsAd boards, collecting data, applying time stamps, and sending events over a 10 Gb/s fiber-optic link to a storage cluster [107]. The MuTAnT (Multiplicity, Trigger, And Time) board synchronizes CoBos and manages clock synchronization and global triggers. Fig. 3.6 represents a schematic of the GET electronics system.

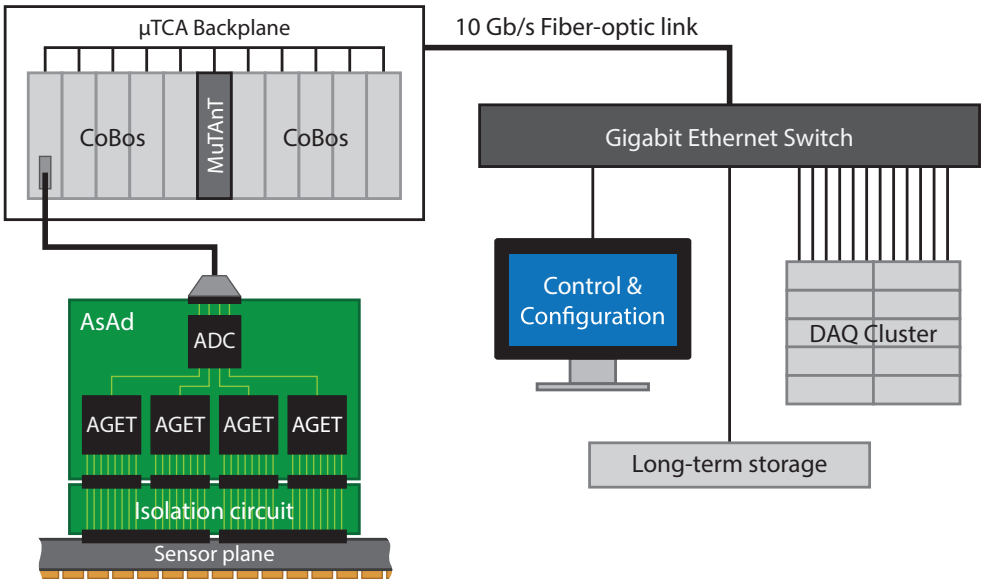

Figure 3.6 Schematic of GET electronics system. Only one out of 40 AsAd boards is shown here for clarity. Figure has been taken from Ref. [107].

.

At higher beam intensities, space-charge effects can be observed inside the AT-TPC [108]. The positive ions inside the AT-TPC volume move at a much slower pace compared to the electrons after the ionization has taken place. As a result, positive charge is accumulated in the beam region over time. The magnitude of this space charge is directly proportional the beam rate. For a constant beam rate, R, electron-ion pairs per unit volume have a production rate of [109]:

$$\dot{N} = \left(\frac{dE}{dx}\right)\frac{R}{wA}, \tag{3.2}$$

where $\left(\frac{dE}{dx}\right)$ is the beam stopping power in the gas, A is the beam spot area and w is the mean ionization energy of the gas. For D_2 gas, w = 37 eV. The space charge produces an electric field and affect the electron drift. Many electrons interact with nearby ions and recombine causing a loss in collected charge.

In this experiment, the AT-TPC was placed at the target location of the S800 (see Fig. 3.7) to allow measurements of heavy residues. The volume of the AT-TPC was filled with pure D_2 gas at a pressure of 530 Torr, corresponding to a target thickness of 11 mg/cm^2 and shielded from beamline

and S800 vacuum with PPTA windows. The deuterium gas served as the target and tracked the two protons from the unbound ^{2}He. A uniform electric field of 500 V/cm was applied to guide the electrons towards the Micromegas detector.

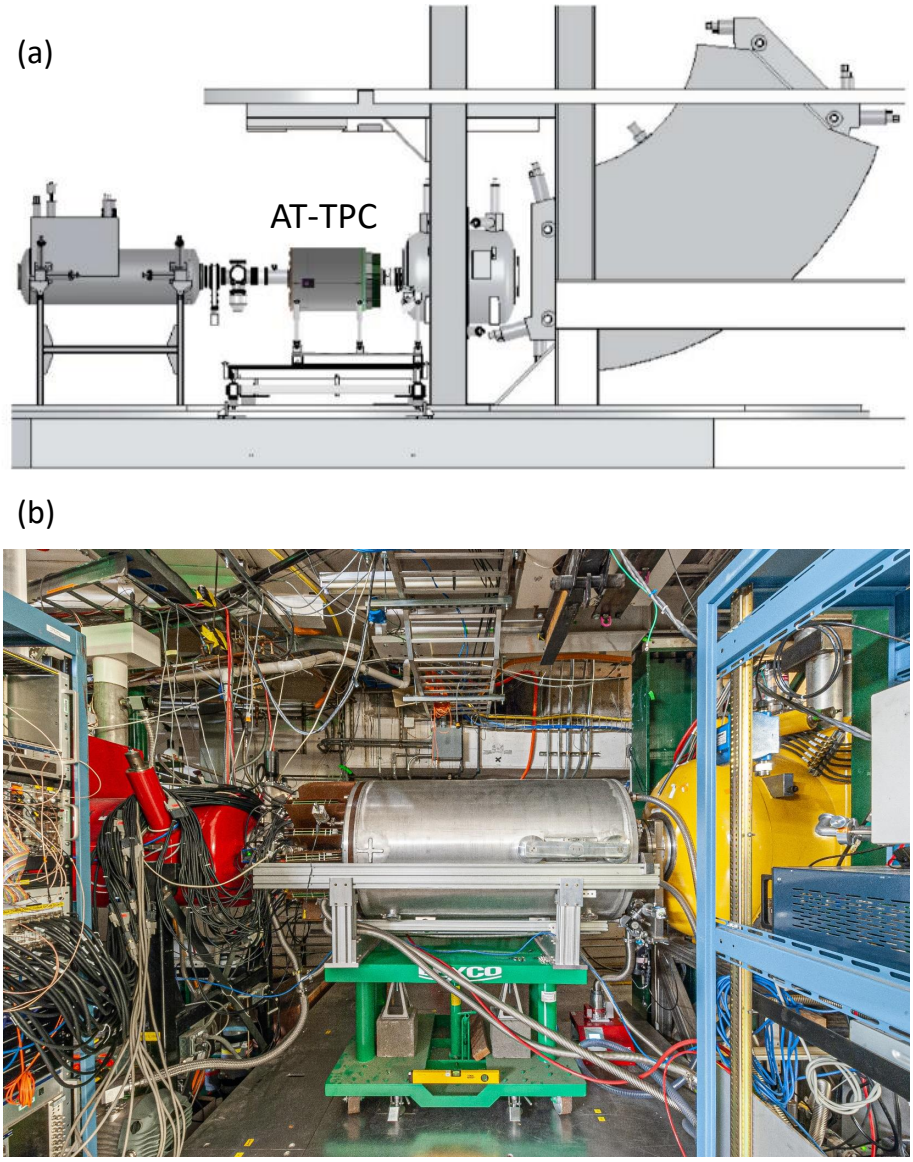

Figure 3.7 (a) Schematic layout of the AT-TPC at the target location of the S800 used for the experiment. Figure has been taken from [104]. (b) Picture of the AT-TPC at the target location of the S800 after installation of the cabling system prior to the start of the experiment.

.

The beam-like particles were transmitted through the AT-TPC to the S800 focal plane by 3 cm

exit hole in the cathode plane. Therefore, the particles, fast fragments, and their decay particles were not detected in the AT-TPC. Particle identification capabilities of the S800 allows the isolation of reactions with specific exit channels. The S800 has a clock that provides a timestamp, which is injected into one of the CoBos capable of accommodating an external clock. Meanwhile, the other clocks in the system use a common internal clock from the MuTAnt board, which records the timestamps of events in the AT-TPC. These timestamps from both systems are then matched to correlate the events recorded by the S800 and the AT-TPC. The trigger from the S800 is used to register events for the entire system. So, in principle, the number of events recorded by both DAQs should be identical. However, due to occasional event loss in either DAQ, precise timestamp matching becomes crucial for ensuring accurate data synchronization. Fig. 3.8 shows the comparison of AT-TPC and S800 timestamps for a sample of events from one run. The data points forming a line with a slope of 1 confirm that the timestamps are synchronized. The AT-TPC provided information for the two proton tracks correlated with the (d,^{2}He) reaction and decay products in the focal plane of the S800 from which the momentum of the ^{2}He particle can be reconstructed. The reconstruction process is discussed in detail in Sec. 4.7.

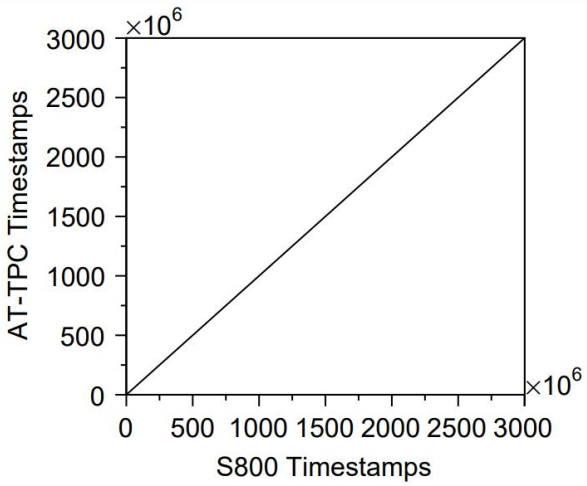

Figure 3.8 Correlation between the AT-TPC and S800 timestamps for a subset of events from a specific run. The data points align along a smooth line with a slope of 1, indicating a consistent match between the two sets of timestamps.

.

3.4 Magnetic Rigidity Setting

The S800 was tuned to an optimal magnetic rigidity (Bρ) setting for the recoil and decay products of the two major components of the beam, ^{33}Al and ^{32}Mg. The recoil products of ^{33}Al and ^{32}Mg are ^{33}Mg and ^{32}Na, respectively, which decay to ^{32}Mg and ^{31}Na through neutron emission. By gating on the one-neutron decay product within the chosen magnetic rigidity setting, we were able to reconstruct the excitation energy spectra of ^{33}Mg and ^{32}Na up to their two-neutron separation energies without losing any information. Table 3.1 provides the one- and two-neutron separation energies, as well as the separation energies for one proton, two protons, alpha, and deuteron for both nuclei.

Table 3.1 Separation energies for one neutron (S_n), two neutrons (S_{2n}), one proton (S_p), one deuteron (S_d), two protons (S_{2p}), and one alpha particle (S_α) for ^{32}Na and ^{33}Mg.

Reaction	S_n (MeV)	S_{2n} (MeV)	S_p (MeV)	S_d (MeV)	S_{2p} (MeV)	S_α (MeV)
^{32}Mg(d,^{2}He)^{32}Na*	1.68	5.98	19.8	19.98	44.9	45.49
^{33}Al(d,^{2}He)^{33}Mg*	2.28	8.06	20.97	22.64	40.8	26.93

As the excitation-energy spectra are obtained by measuring the recoil products and decay products up the two neutron separation energy, it is possible to study the main features of the low-lying B(GT)s in the distribution. Fig. 3.9(a) illustrates the Bρ settings optimized for the reaction products and their decay products from the ^{33}Al(d,^{2}He) and ^{32}Mg(d,^{2}He) reactions. The total rigidity spread of the 4 ejectiles is 5.2% and the rigidity acceptance of the S800 is 5.8%, so it was possible to study all the ejectiles of interest at the Bρ setting of 3.904 Tm. However, a fraction of the reaction product ^{32}Na was outside of the Bρ acceptance, which was taken into account during the analysis to obtain the differential cross-section. This occurred because the yield of reaction products was low and the cut-off in the ^{32}Na distribution was not identified during the experiment.

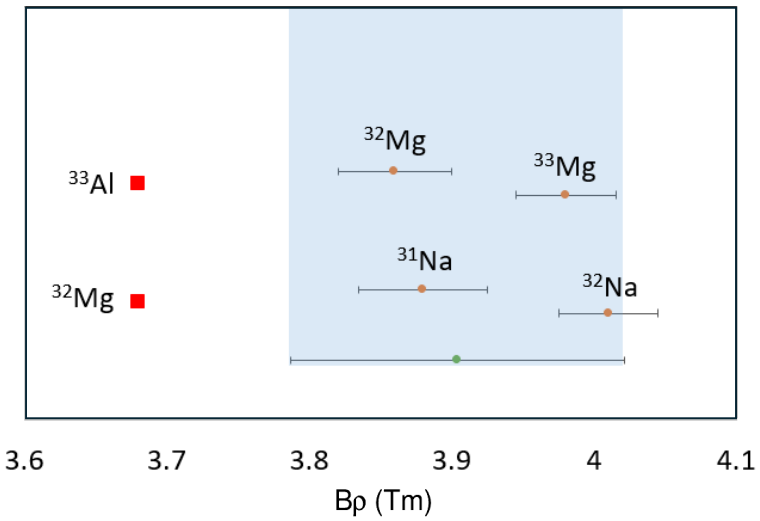

Figure 3.9 The $B\rho$ ranges for CE reaction products and decay products from the (d,^{2}He) reaction on ^{33}Al and ^{32}Mg isotopes are shown. Horizontal bars represent the full width of $B\rho$ distributions. The blue band shows the $B\rho$ acceptance (±2.9%) centered at $B\rho$ = 3.904 Tm.

CHAPTER 4

DATA ANALYSIS

4.1 S800 CRDC Calibration

The CRDC detectors at the focal plane of the S800 had to be calibrated in order to accurately determine the particle's position and angle. This task was accomplished by remotely inserting a "mask", which is a metal plate, in front of each CRDC. The mask is made of tungsten and has holes and slits at known locations as shown in Fig. 4.1(a). Once the mask was placed, only the particles making it through the holes are detected in the CRDCs and are used in the calibration process.

The mask calibration is done by relating channel numbers to actual physical distances (in mm) for the CRDCs. Fig. 4.1(a) represents the mask with holes and slits used for calibration and Fig. 4.1(b) shows the particles detected at the CRDCs making it through the hole. The x-position is determined from the charge induced on the pads and the slope is fixed to 2.54 mm/pad, according to the width of the pads. The y-position depends on the drift velocity of the particles, which varies with gas composition, pressure, and time. The slope in the y-direction was determined by fitting a Gaussian to the y-axis projection of the particles that passed through the mask shown in Fig. 4.1(b). The following equations were used to obtain the offsets in x-direction and y-direction, respectively:

$$x_{1,2}(mm) = m_{1,2}(mm/pad) \times x_{1,2}(pad) + b_{1,2}(mm) \tag{4.1}$$

$$y_{1,2}(mm) = n_{1,2}(mm/ns) \times y_{1,2}(ns) + c_{1,2}(mm) \tag{4.2}$$

m_1	b_1	n_1	c_1	m_2	b_2	n_2	c_2
2.54	-278.9	-0.12048	140.24068	2.54	-278.6	0.10638	-133.93590

Table 4.1 Parameter values obtained from the masked calibration of two CRDCs.

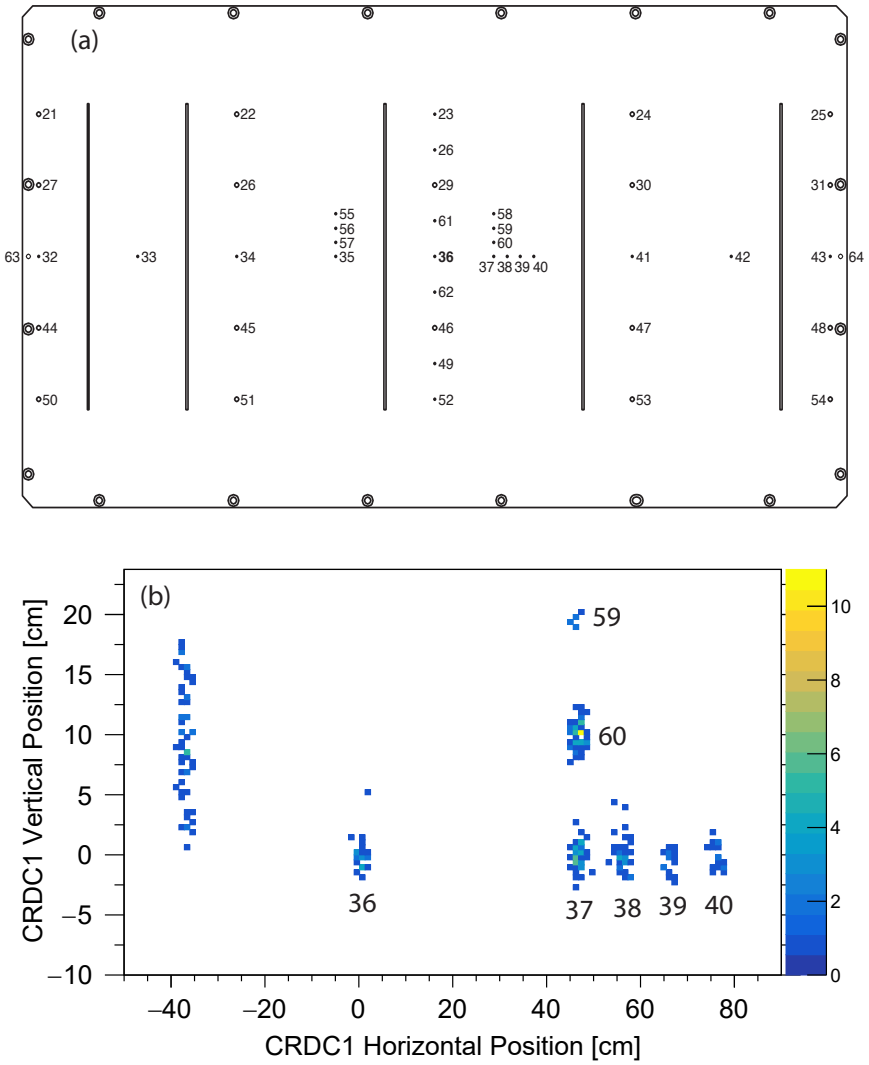

Figure 4.1 (a) Mask used for calibration of the CRDCs. (b) Position measurements for CRDC1 mask calibration. The measurements associated with the known hole positions in the mask are used to measure the offset and slope of the y-position as explained in text.

The values obtained from the calibration of both the CRDCs are listed in Table 4.1. The angles and positions in the focal plane can be calculated from these calibrated values using the following equations:

$$afp = atan\left(\frac{x_2 - x_1}{1073}\right) \tag{4.3}$$

$$bfp = atan\left(\frac{y_2 - y_1}{1073}\right) \tag{4.4}$$

$$xfp = x_1 \tag{4.5}$$

$$yfp = y_1 \tag{4.6}$$

where afp and bfp are the dispersive and non-dispersive angles, respectively, and xfp and yfp are the x and y positions, respectively. The distance between the two CRDCs is 1073 mm. These parameters are used to reconstruct the trajectory and properties of particles at the reaction vertex by applying an inverse transfer map matrix generated through a COSY INFINITY [110] calculation. A ray-tracing calculation is employed to determine four parameters at the location of the scattering event: position in the non-dispersive direction (yta), scattering angle in the dispersive plane (ata), scattering angle in the non-dispersive plane (bta), and measure of the energy of the scattered particle (dta), where $E = E_0(1 + dta)$ with E_0 being the central energy of the focal plane.

The ata and bta distributions were obtained from the unreacted beam setting. As shown in Fig. 4.2, these distributions are used in the simulation (see Sec. 4.6) to randomly draw the beam angles in the x and y directions. Since the ray-tracing depends on the distance along the z-position of the beam and the reaction can take place anywhere in the AT-TPC, we performed the ray-tracing using a set of ray-trace maps, which are interpolated to cover all positions along the length of the AT-TPC.

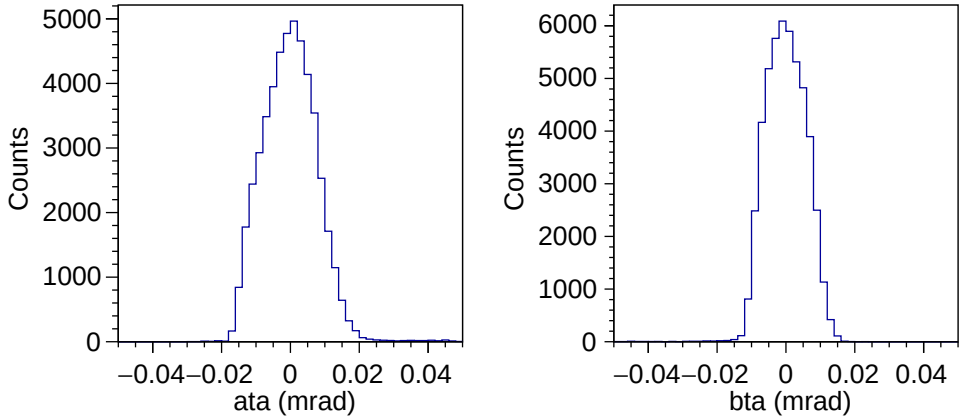

Figure 4.2 (a) Dispersive scattering angle (ata) and (b) non-dispersive scattering angle (bta) distributions obtained from ray-tracing calculation from beam runs sent directly to the S800 focal plane without any reaction with the target.

The magnetic rigidity spread for the reaction products ^{33}Mg and ^{32}Na were obtained from the dta distribution and are illustrated in Fig. 4.3.

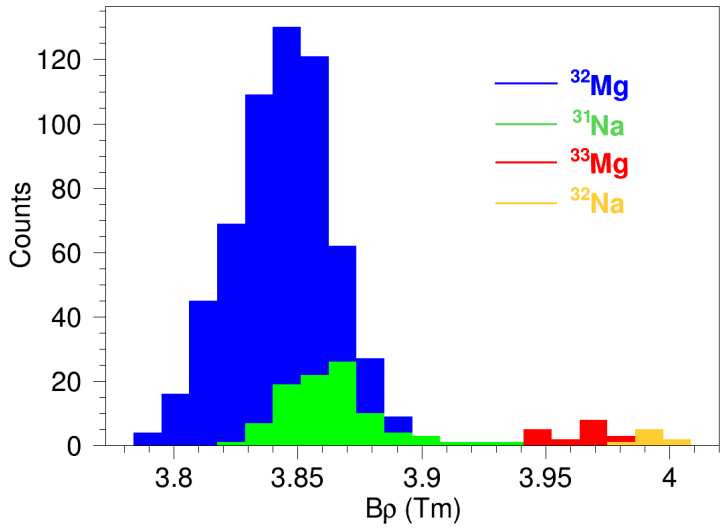

Figure 4.3 Measured $B\rho$ distributions for ^{33}Mg and ^{32}Mg from the ^{33}Al(d,^{2}He) and for ^{32}Na and ^{31}Na from the ^{32}Mg(d,^{2}He) reaction at the central $B\rho$ setting of 3.904 Tm.

4.2 Beam Gate

The cocktail beam mainly consisted of ^{33}Al and ^{32}Mg with small quantities of contaminants. A gate was used in the analysis to isolate events associated with each incoming beam. ToF measurements between a plastic scintillator positioned at the exit of ARIS and the object scintillator were used to accurately gate the desired beam within the cocktail beam. The absolute ToF scale for the S800 was calibrated using the beam velocities and the measured distance between two plastic scintillators. The beam velocities, calculated using LISE^{++}, were 12.7 cm/ns for the ^{33}Al beam and 12.2 cm/ns for the ^{32}Mg beam [111]. The distance between the two scintillators is 34.28 m. Fig. 4.4 illustrates the separation of the beam components, which was achieved using Time-of-Flight (ToF) measurement between the two scintillators. We applied an 1D gate on the ToF measurement for the beam of interest.

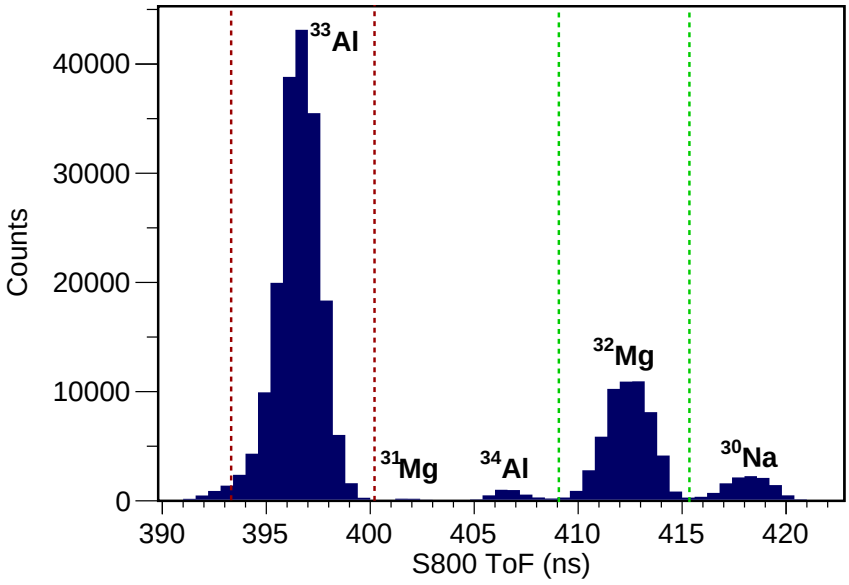

Figure 4.4 ToF (in ns), shown on logarithmic scale, between the two plastic scintillators placed at the exit of ARIS fragment separator and the beam entrance line of the S800 showing event-by-event incoming beam particles identification. The red and green dashed lines represent the boundaries of the gates drawn for ^{33}Al and ^{32}Mg beams, respectively.

4.3 Particle Identification

The particles of interest in this experiment were the recoil product ^{33}Mg and its decay product ^{32}Mg from the ^{33}Al beam, as well as ^{32}Na and its decay product ^{31}Na from the ^{32}Mg beam. Fig. 4.5

illustrates the reaction processes and decay products of the various beam components, recorded at the focal plane of the S800. The particle identification (PID) was performed using the ΔE-ToF method.

The energy loss, ΔE, was measured by the ionization chamber at the focal plane, and its dependence on the particle's charge Z^2 is described by the Bethe-Bloch formula (see Eq. 3.1). The measurement of ΔE allowed identification of the charge of the particle, thereby determining the element. However, this method alone could not distinguish isotopes of the same element. The time-of-flight (ToF) was determined by measuring the time difference between the object scintillator and the focal plane scintillator. The ToF measurement provided crucial information about the particle's velocity, v, for the known flight path, L. For a constant magnetic rigidity, B_ρ, and known flight path L, the ToF measurement relates the particle's mass-to-charge ratio, $\frac{m}{q}$, to its velocity as shown below:

$$B_\rho = \gamma \frac{mv}{q} \rightarrow \frac{1}{v} = const. \times \frac{m}{q} = \frac{ToF}{L} \tag{4.7}$$

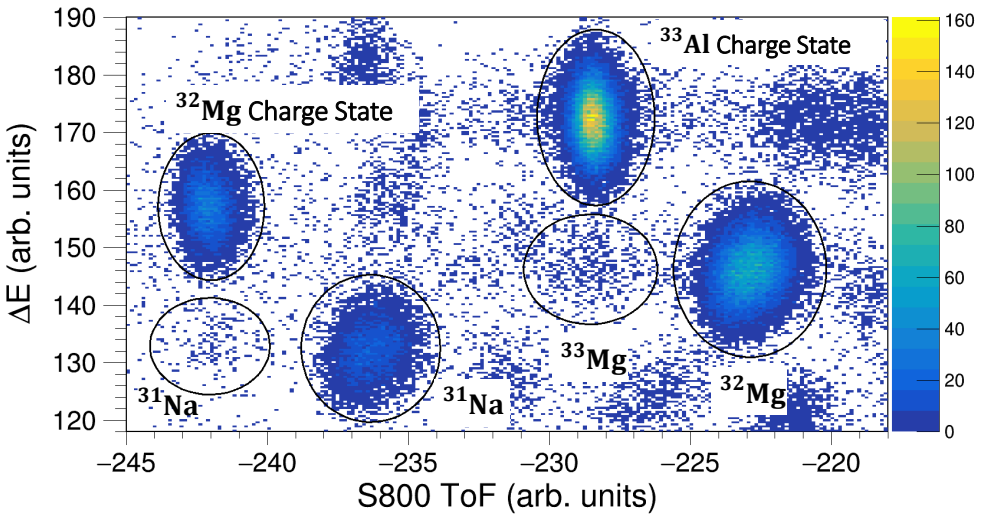

Figure 4.5 Particle identification at the focal plane of the S800. ^{33}Mg and ^{32}Na are the reaction products from the ^{33}Al(d,^{2}He) and ^{32}Mg(d,^{2}He) reactions, respectively. Following neutron decay, ^{33}Mg and ^{32}Na produce ^{32}Mg and ^{31}Na, respectively, as their decay products. The ^{33}Al and ^{32}Mg charge states represent the beam particles that picked up an electron from the AT-TPC gas or windows, but did not undergo a nuclear reaction.

The gates around the blobs in the PID plot were defined using 3σ cuts from Gaussian fits to the projections on both the x and y axes. As an example, Fig. 4.6 shows the projection of the ^{32}Mg fragment, identified in Fig. 4.5, along the x-axis (S800 time of flight).

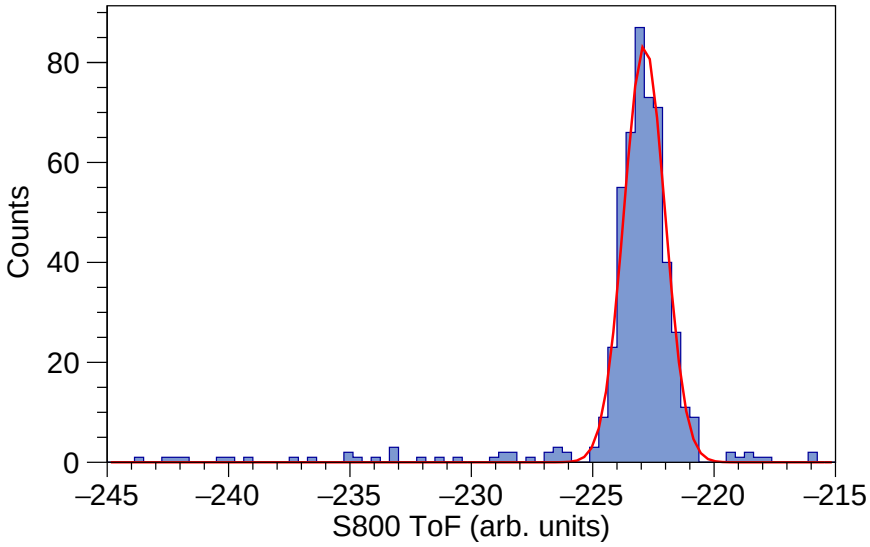

Figure 4.6 Projection of the ^{32}Mg fragment on the S800 time of flight (ToF) axis. The red curve represents a Gaussian fit used to define the gate for fragment identification, with the gate set around 3σ from the fit to ensure accurate selection of events.

A similar approach was used for the y-axis projection to ensure accurate fragment identification, as shown in Fig. 4.7, also for the case of ^{32}Mg.

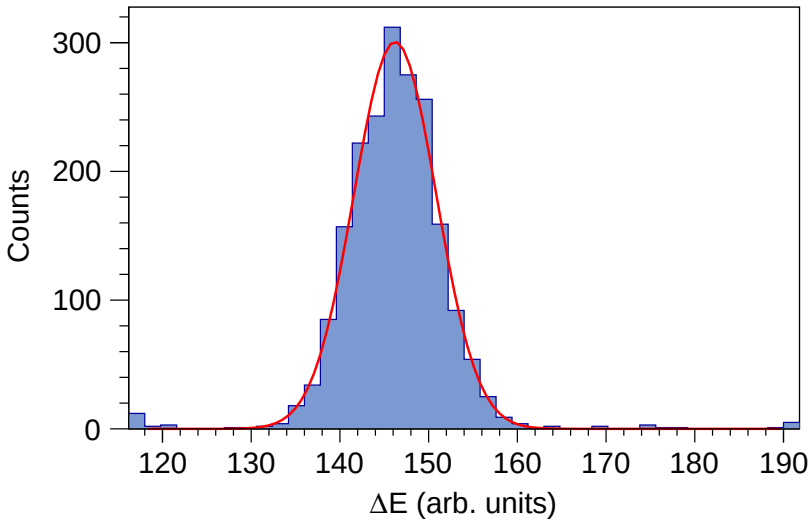

Figure 4.7 Projection of the ^{32}Mg fragment on the ΔE axis. The red curve represents a Gaussian fit used to define the gate for fragment identification, with the gate set around 3σ from the fit to ensure accurate selection of events.

In cases where a 3σ gate would overlap with another fragment's gate, we reduced the gate width and adjusted the corresponding cross-sections accordingly. It is noted that there is some background on the PID plot of Fig. 4.5. However, the requirement of a (d,^{2}He) event, associated with 2 proton tracks from a single vertex in the AT-TPC (see Sec. 4.4), removes the background not associated with CE events.

4.4 Event Reconstruction in the AT-TPC

A point cloud, consisting of a set of hit points defined by distinct spatial coordinates, was generated for each event occurring within the AT-TPC gas volume (see Fig. 4.8). The x and y coordinates of these points were obtained from the hit pattern on the pad plane of the AT-TPC and the z coordinate was determined from the drift length of the electrons. The drift length was calculated from the drift time and drift velocity. The drift velocity depends on certain factors and requires correction, detailed in Sec. 4.5. After obtaining accurate coordinates for the hit points, the RANSAC (Random SAmple Consensus) algorithm was utilized to analyze the point clouds for all events. The routine identifies the hits that belong to a track and reject the noise points. Then

the tracks are fitted by a 3D line using χ^2 minimization. Ref. [112] describes the details of the algorithm as applied to the analysis of AT-TPC data.

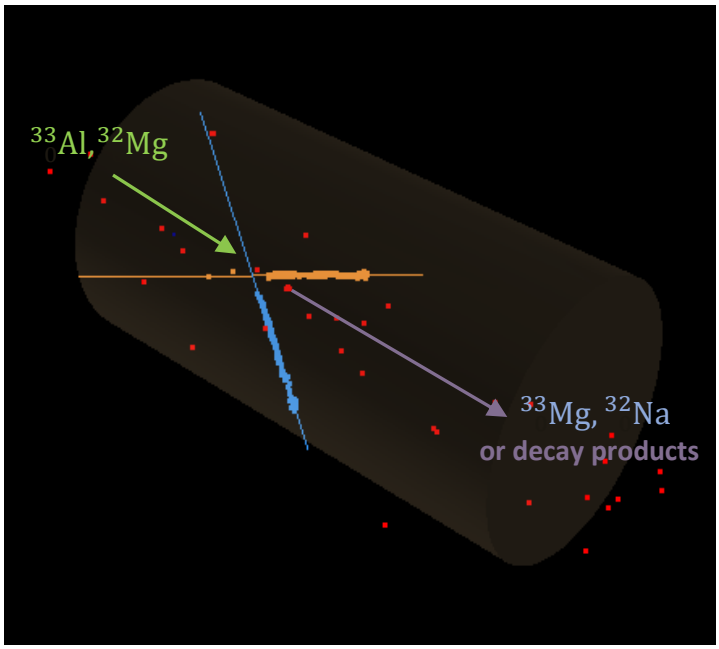

Figure 4.8 Visualization of the beam entering the AT-TPC through the entrance hole, with the residual and decay products exiting through the opposite side after interacting with the deuterium gas. The visualization also includes a representation of fitting the particle tracks onto a point cloud, based on data from a real event in the ^{33}Al(d,^{2}He) reaction.

.

Inside the AT-TPC, the δ electrons are the primary source of background. However, the signals from δ electrons can be significantly reduced by applying a threshold, as the charge induced on the pad plane by the interaction of δ electrons is much lower compared to that of protons or other ion tracks. The threshold value is optimized empirically by testing a range of values and selecting the ones that effectively suppress δ electron signals without affecting the detection of proton signals. Fig. 4.9 illustrates a real (d,^{2}He) event with fitted tracks using the RANSAC algorithm. There are some signals in the plot not attached to any particular track which are most likely the result of electronic noise or remaining signal from δ electrons produced in the AT-TPC.

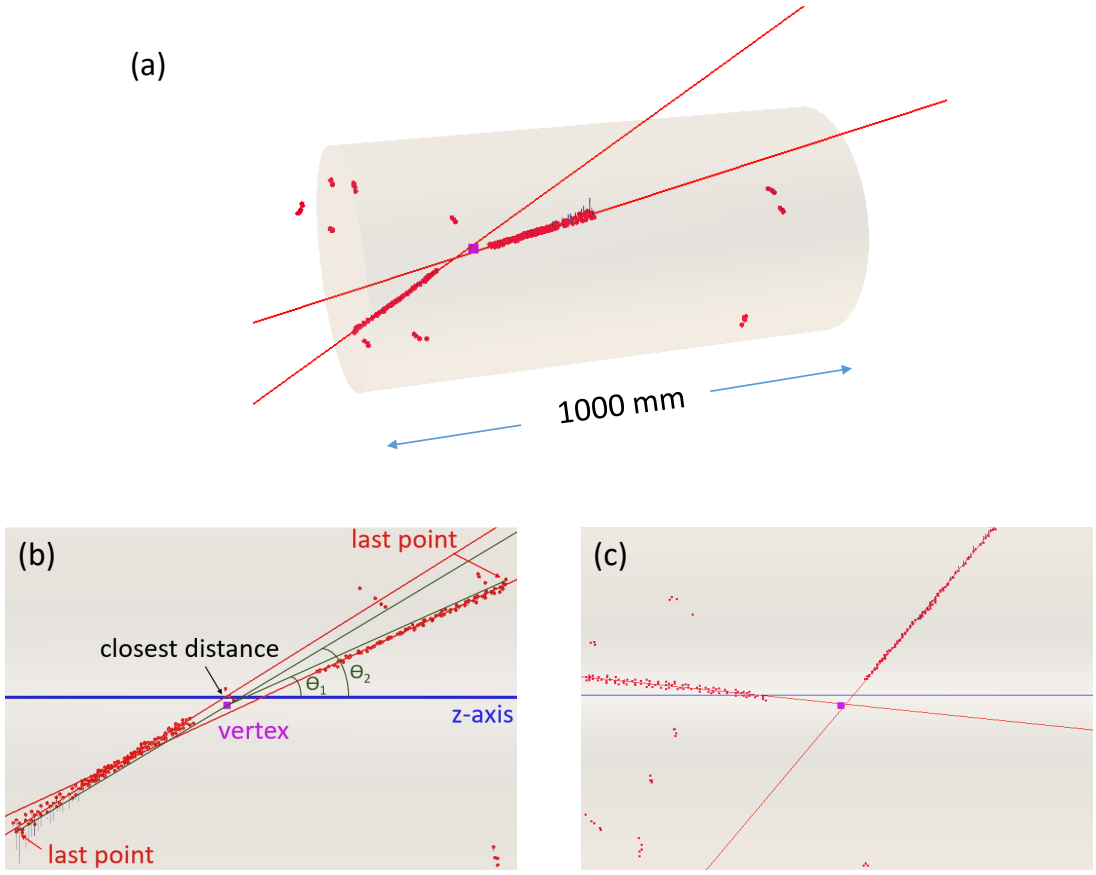

Figure 4.9 Real event from a (d,^{2}He) reaction visualized inside the active volume of the AT-TPC. (a) The two tracks in 3D are formed from the hits using RANSAC algorithm. (b) Closest distance between the two tracks, vertex reconstruction, projection of the last points on the vertex, and angles of the tracks are shown for the same run and event as (a). (c) The same event as (a) and (b) where the two tracks are seen to be intersecting at the vertex from a different perspective to show the vertex is reconstructed at the closest distance in 3D.

.

For events where at least two tracks are identified, a vertex is determined by the center of the closest distance between the two fitted tracks. Due to the insensitivity of the central region of the AT-TPC, the vertex location was determined based on extrapolated tracks from the fitting process. The vertex position was weighted by the number of hits on each track for tracks with less than 50 hit points. Without applying this weighting, the distribution of the closest distance between the two tracks broadened because shorter tracks will have a larger uncertainty in the reconstructed angle. This distance followed a roughly half-normal distribution, as shown by the fit of the distance

between the two reconstructed tracks at the vertex in Fig. 4.10. The scale parameter σ of the half-normal distribution ranged from 7 to 7.5 mm during the experiment. Events where the closest distance exceeded 3σ were excluded from the analysis.

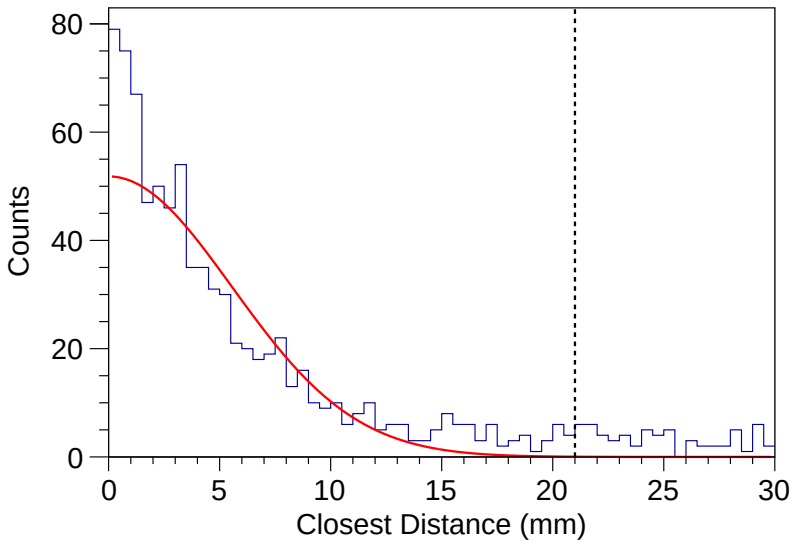

Figure 4.10 Distribution of the closest distance between two reconstructed tracks at the vertex, fitted with a half-normal Gaussian (red curve) for ^{33}Al beam. The events on the right of dotted line were excluded from the analysis.

.

In Fig. 4.9(b), the two straight lines in red were the two fitted tracks and the square in pink was the reconstructed vertex for this event. The length of the tracks were defined as the distance between the vertex and the last point on the fitted tracks, as labeled in Fig. 4.9(b). The last point is the hit with the largest radius from the vertex. The angle of the tracks, labeled as θ_1 and θ_2, were determined between the beam axis and the direction of the tracks. Events in which either or both tracks escaped the active volume of the AT-TPC were excluded from the analysis since accurate reconstruction of these events is not feasible.

As discussed in Sec. 3.3, space-charge effects can distort the tracks close to the beam line in central region of the AT-TPC (see Fig. 4.11). This can impact the quality of the reconstructed tracks. To address this issue, a correction factor was incorporated into the analysis code. Here, we describe the process for correcting the hit points.

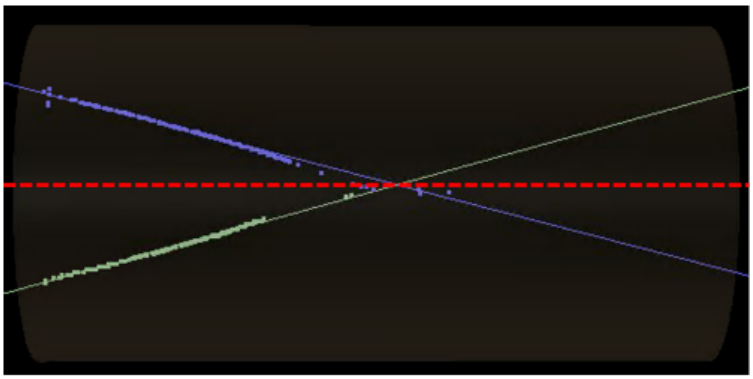

Figure 4.11 The two reconstructed tracks based on hit points. The 3D hit cloud illustrates the deviation from a straight line near the beam region, where hits are drawn inward due to space charge effects. Figure has been taken from Ref. [113].

.

If we treat the space charge as a long thin wire centered at (0,0), the electric field can be given by:

$$\vec{E} = \frac{\lambda z}{2\pi\epsilon_0 \rho L}\hat{\rho} \tag{4.8}$$

where λ is the magnitude of the line charge at the window, z is the distance from the pad plane, and L is the length of the drift volume. There is a closed form solution to the Langavin equation in the z direction for this model given by [113]:

$$\rho_f^2 - \rho_i^2 = \frac{\lambda z^2}{2\pi\epsilon_0 E_z L} \tag{4.9}$$

where ρ_f^2 is the distance from space charge line after correction and ρ_i^2 is the distance from the space charge line before correction. We can rewrite Eq. 4.9 as:

$$(\rho_f + \rho_i)(\rho_f - \rho_i) = \frac{\lambda z^2}{2\pi\epsilon_0 E_z L} \tag{4.10}$$

Here, we can define $(\rho_f - \rho_i) = \Delta\rho$ and $(\rho_f + \rho_i) = r$. If we assume ρ_f is really small, then $r \approx \rho_i$. Therefore, the correction factor we need to apply to our hit points simply becomes:

$$\Delta\rho = \frac{cz^2}{\rho_i} \tag{4.11}$$

where $c = \lambda/(2\pi\epsilon_0 E_z L)$. In cylindrical coordinates, the hit points in our point cloud will have the coordinates:

$$\rho = \sqrt{x^2 + y^2} \tag{4.12}$$

$$\theta = \arctan\left(\frac{y}{x}\right) \tag{4.13}$$

$$z = z \tag{4.14}$$

The cylindrical coordinates of the hit points after correction becomes:

$$\rho' = \rho + \Delta\rho = \sqrt{x^2 + y^2} + \Delta\rho = \frac{cz^2}{\rho_i} \tag{4.15}$$

$$\theta' = arctan\frac{y}{x} \tag{4.16}$$

Now transforming the cylindrical units back into cartesian ones we get:

$$x' = \rho' cos\theta = (\sqrt{x^2 + y^2} + \frac{cz^2}{\sqrt{x^2 + y^2}})cos(arctan\frac{y}{x}) \tag{4.17}$$

$$y' = \rho' cos\theta = (\sqrt{x^2 + y^2} + \frac{cz^2}{\sqrt{x^2 + y^2}})sin(arctan\frac{y}{x}) \tag{4.18}$$

$$z' = z \tag{4.19}$$

In this analysis, we treat c as a correction factor, with the primary variable being λ, while all other parameters remain constant. Thus, varying c effectively corresponds to varying λ. In our code, we run the analysis for several values of c to determine the optimal correction for the best track fit quality. To identify the best fit, we compute the average χ^2 of the fits for two tracks and find which value of c yields the lowest χ^2. Once the optimal c is identified, the subsequent calculations

proceed using that value. This method enables us to correct for track curvature on an event-by-event basis.

In this $(d,^2\mathrm{He})$ experiment, the track curvature was minimal. Fig. 4.12 shows the count distribution for the optimal c values used in the analysis (with the y-axis on a logarithmic scale). It is evident that for most events, the lowest χ^2 was achieved when $c = 0$. We tested c values from 0 to 1×10^{-4} in steps of 1×10^{-5}, which causes the highest value of c to be biased. If we had extended the range, the final bin would likely have a similar count to the preceding bins. The events with non-zero c values likely arise from random coincidences. Since space-charge corrections did not significantly improve the fits, they were not applied in the analysis.

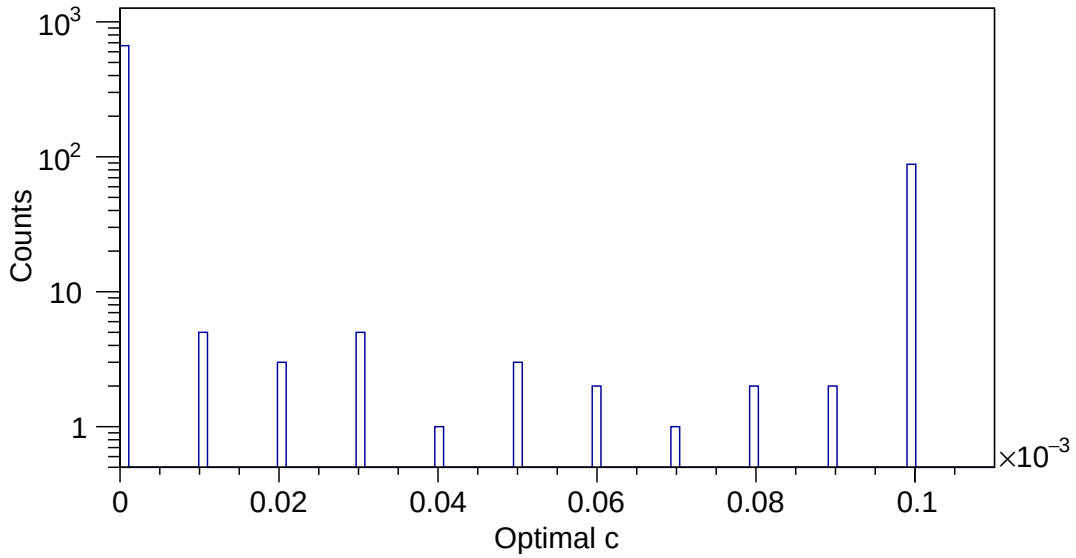

Figure 4.12 Distribution of the optimal curvature parameter c used in the track fitting analysis for the $^{33}\mathrm{Al}(d,^2\mathrm{He})^{33}\mathrm{Mg}$ reaction, plotted on a logarithmic scale. The majority of events exhibit minimal track curvature, as indicated by the peak at $c = 0$. The corresponding low χ^2 values show that space-charge corrections did not significantly improve the fits, leading to the decision not to apply them in the final analysis.

.

Another approach to improve the track fitting was to eliminate sections of the tracks close to the beam axis, where most of the bending occurs due to space charge accumulation. We ran the analysis multiple times, cutting off different initial track lengths. Fig. 4.13 presents the average χ^2

of the fits, scaled by the total charge, for two tracks in three different cases: the black line represents the average χ^2 with no portion of the tracks removed, the green line represents the average χ^2 after removing the first 10 mm to eliminate bending, and the red line shows the average χ^2 after removing the first 40 mm.

While cutting off the first 40 mm resulted in fewer statistics due to excluding short tracks or having too few remaining hits to reconstruct both tracks, no significant difference in statistics was observed between the cases with no cut and with the 10 mm cut. In all trials, the charge-scaled χ^2 distributions were comparable, as observed in Fig. 4.13, indicating that removing portions of the tracks did not impact the fit quality. Therefore, we decided to continue the analysis without eliminating any parts of the tracks.

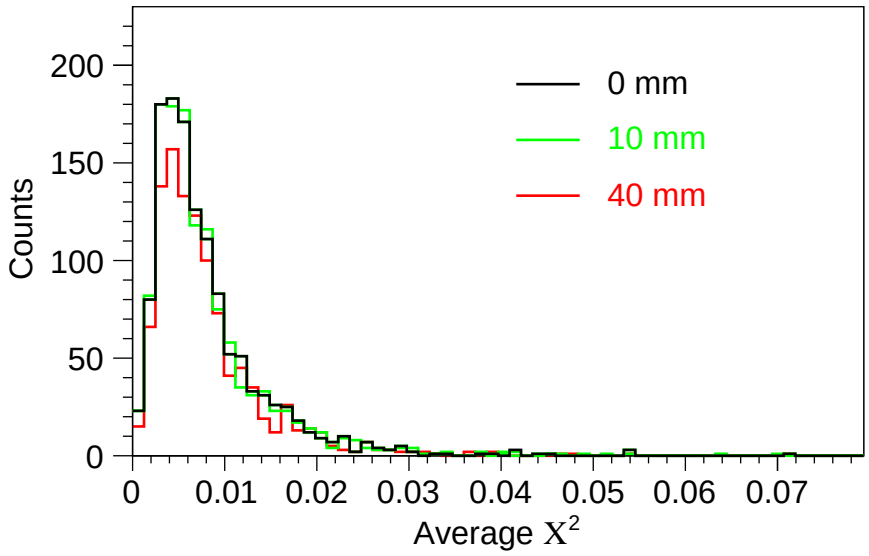

Figure 4.13 Distribution of the average χ^2 values scaled by total charge for two tracks under three different conditions: no track section removed (black line), first 10 mm of the tracks removed (green line), and first 40 mm of the tracks removed (red line). While removing the first 40 mm reduced the overall statistics, the χ^2 distributions remain comparable across all cases, indicating that eliminating portions of the tracks near the beamline does not significantly impact the quality of the fits.

.

In the experiment, the alignment of the AT-TPC's axis with the beam axis was not perfect.

Since this impacts the kinematic reconstruction, this angle was determined and used in the further analysis. The angles were calculated based the reconstructed vertices from 2 track events, including ones in which one or both tracks escaped the chamber.

Fig. 4.14(a) illustrates a scatter plot of the vertex positions in the x-axis (vertexX) versus the longitudinal axis (vertexZ) inside the AT-TPC. The trendline fitted to these points gives the beam's angle relative to the x-axis, along with the corresponding offset at the entrance window. Similarly, Fig. 4.14(b) shows a plot of the vertex positions in the y-axis (vertexY) against vertexZ, with the fitted line providing the beam's angle and offset relative to the y-axis.

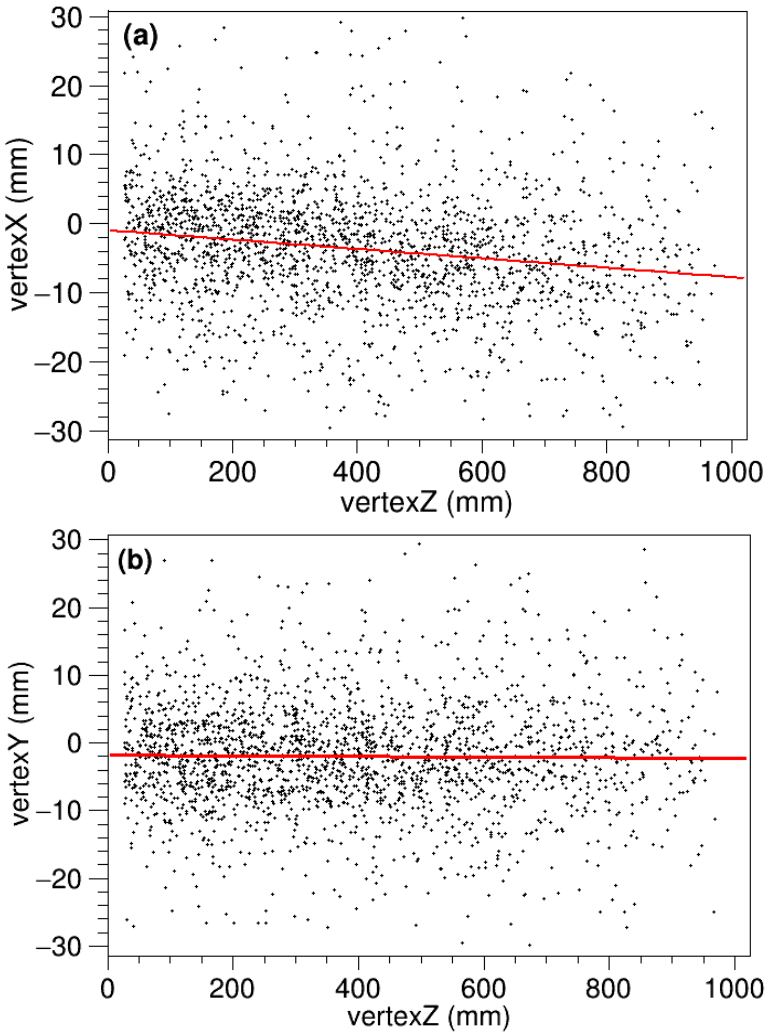

Figure 4.14 Reconstructed vertex locations from two-track events in the (a) xz-plane and (b) yz-plane. The red lines are the fits and indicate the beam axis.

$\theta_{beam,x}(deg)$	$\Delta_{beam,x}(mm)$	$\theta_{beam,y}(deg)$	$\Delta_{beam,y}$ (mm)
-0.393	-0.89	-0.026	-1.807

Table 4.2 Angles and offsets of the beam in x and y direction at the entrance window of AT-TPC. The offset Δ is the offset at z = 0.

These angles and offsets are essential for aligning the experimental setup with the beam axis and are summarized in Table 4.2, which reports the exact values for the beam's angular deviation and the corresponding offsets in both the x and y directions. This correction ensures the precision of the particle tracking data and helps improve the overall accuracy of the analysis.

4.5 Drift Velocity Correction

The drift velocity of particles inside the AT-TPC gradually decreased over time, possibly due to the accumulation of contaminants, necessitating a correction. Since the drift length of particles within the AT-TPC volume is 1000 mm, we expect the reconstructed vertex Z positions to be constrained within the physical limits of the AT-TPC. Specifically, the vertex distribution along the Z-axis should span from 0 to 1000 mm. If the vertex distribution stretches beyond this range or ends before reaching 1000 mm, it indicates that a drift velocity correction is required. To address this, we apply a straightforward correction procedure on run-by-run basis. The drift velocity correction was performed with one-track events to improve the accuracy of the correction.

The drift velocity corrections applied during the first and second (d,^{2} He) experiments in inverse kinematics were not identical. In the first experiment, for the analysis of the ^{14}O(d,^{2} He) and ^{13}N(d,^{2} He) reactions, the one-track events were analyzed under the assumption of a fixed drift velocity, which was calculated using the computational program Magboltz [114]. The vertex Z distribution for each run was then fit with a Fermi function to determine the edge of the distribution, which provided an approximation of the drift length based on the assumed fixed drift velocity. The updated drift velocity was subsequently calculated using the following relationship:

$$\text{New Drift Velocity} = \frac{\text{Fixed Drift Velocity} \times \text{Drift Length in the AT-TPC}}{\text{Edge of vertex Z distribution from fit}}$$

The corrected drift velocity was then applied to more accurately reconstruct the vertex Z

positions. After applying this correction, the edge of the vertex Z distribution should align closely with 1000 mm as shown in Fig. 4.15, which corresponds to the maximum drift length inside the AT-TPC volume.

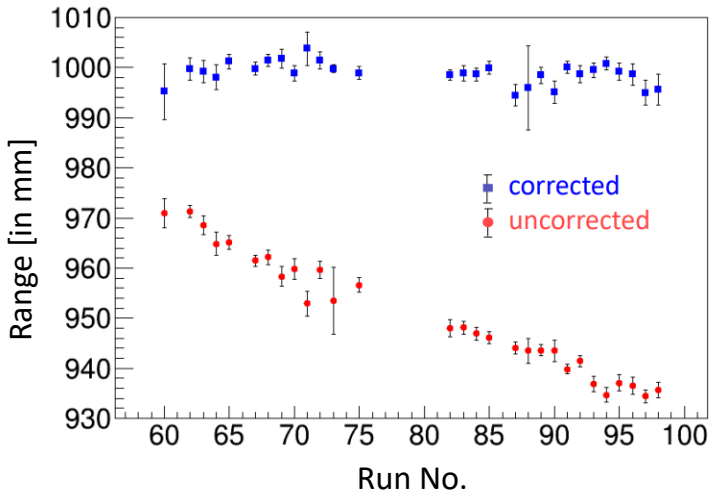

Figure 4.15 Maximum drift length as a function of the run number for the ^{14}O,^{13}N(d,^{2}He) experiment, before (red) and after (blue) the drift velocity correction. The uncertainties shown represent the uncertainties in fitting the maximum drift distance.

For the second (d,^{2} He) experiment using ^{33}Al and ^{32}Mg beams, the limited statistics made drift velocity correction more challenging. In several runs, the data were insufficient to accurately determine the edge of the vertex Z distribution, making it difficult to apply run-by-run corrections. As in the first (d,^{2} He) experiment, one-track events were processed using a pre-determined fixed drift velocity. However, with this fixed velocity, the vertex Z distribution extended beyond the physical boundaries of the AT-TPC, and the distribution's edge showed a linear decline with increasing run numbers, indicating the need for a correction (see Fig. 4.16(a)). Due to the lack of sufficient statistics, run-by-run corrections could not be performed.

To address this issue, we first determined the vertex Z distribution edge for the runs where sufficient statistics were available. These data points were then used to fit a linear relationship between the edge of the distribution and the run number. This linear fit was applied to estimate the drift velocity correction across all runs, allowing for a more consistent correction despite the lower statistics in some runs. After applying the corrections, the edge of the vertex Z distribution

aligns at 1000 mm. Fig. 4.16 shows the vertex Z distribution (a) before, and (b) after correcting for drift velocity across all runs in the experiment. A 2% change in the drift velocity shifts the excitation energy spectrum by approximately 100 keV. For runs 80–112, we applied a lower charge threshold to prevent missing good events, resulting in a higher number of recorded events. However, these additional events were found not to contain additional (d,^{2}He) events and were primarily background from δ electrons. As a result, we reverted to our initial charge threshold setting from run 113.

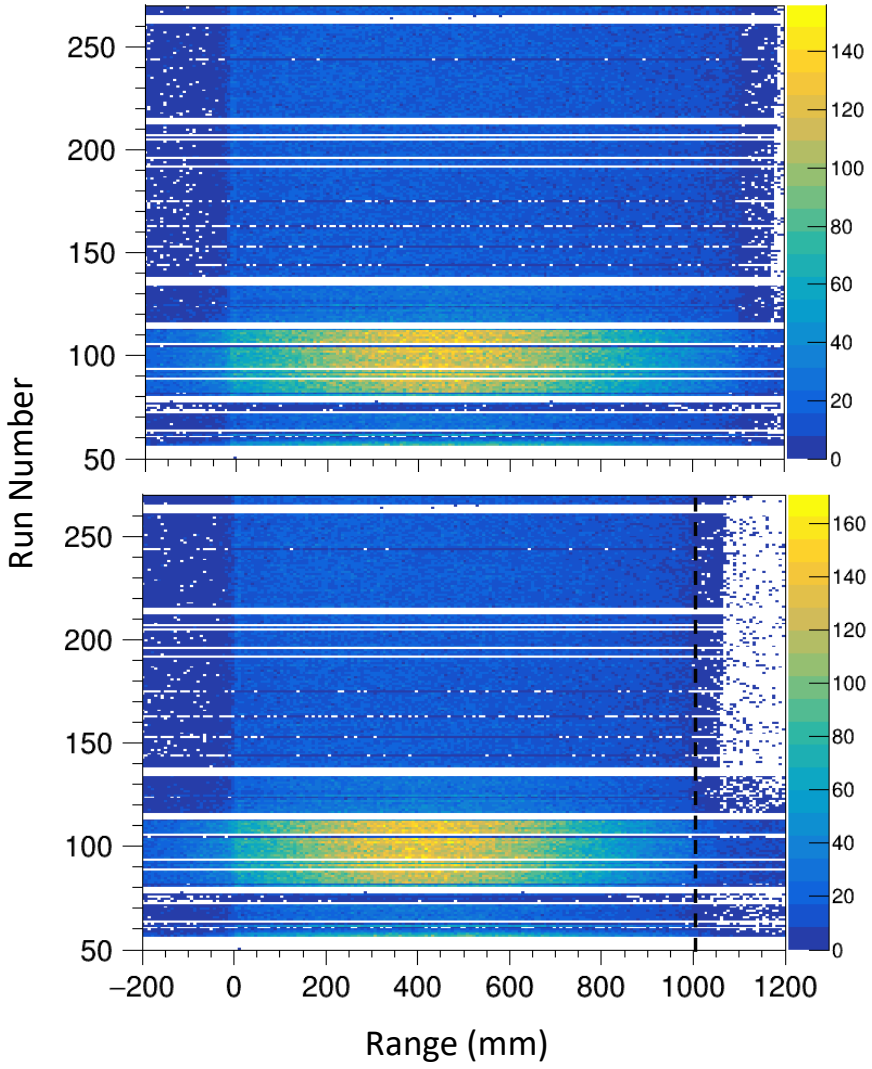

Figure 4.16 The vertex Z distribution across all run numbers: (a) The distribution before any corrections are applied. (b) The distribution after correcting for drift velocity. The dashed black line represents where the edge of the vertex Z distribution was determined to be.

4.6 Simulation

Simulations play a crucial role in understanding the detector response and correcting for the limited acceptance. It also enables benchmarking and a deeper interpretation of experimental data. The ATTPCROOT package [115, 116], written in C++ programming language and developed within the FAIRROOT framework [117], was employed. This package provides comprehensive

tools for both simulation and data analysis. The simulation process is divided into three main stages: event generation, digitization, and reconstruction. Notably, the same analysis code used for reconstructing simulated data is applied to experimental data. This reduces systematic uncertainties with application of acceptance corrections determined in the simulation to the analysis of the data. A brief description of each simulation stage is provided below, with more detailed information available in Ref. [109].

4.6.1 Event Generator

The first stage of the simulation focuses on generating realistic (d,^{2}He) events, comparable to the process of obtaining raw data during the actual experiment. This simulation stage is executed using the Virtual Monte-Carlo (VMC) package [5], which serves as an interface to the GEANT4 toolkit [6]. Within this simulation framework, the geometry of the detection system, beam optics, and all other essential components are thoroughly defined. The event generator class produces the particles, which are then transported through the system by GEANT4, and the corresponding hit information is stored in a class that handles simulated data points.

In the simulation, we define the AT-TPC as having a cylindrical geometry filled with D_2 gas, consistent with the actual experiment setup. The beam parameters-such as mass, charge, and energy-are specified, alongside a detailed implementation of beam optics. This includes the beam angular spread (see Sec. 4.1), the beam momentum spread, and the beam size. These aspects of the beam optics are important for accurately simulating the transport of the beam and its interaction with the target gas inside the AT-TPC.

Additionally, the simulation incorporates the in-flight decay of two protons from ^{2}He. The consistency of the (d,^{2}He) reaction mechanism is maintained by integrating relativistic three-body kinematics for generating particles in the final state. The acceptance of ϵ_{pp}, the relative energy between the two protons, depends on the scattering angle of ^{2}He. The simulation uses theoretical differential cross-sections from ACCBA as inputs (see Sec. 2.3). These cross-sections correspond to different angular momentum components ($\Delta L = 0, 1, 2$). To analyze the data, the simulation is run separately for each ΔL value. This step is important for isolating the $\Delta L = 0$ component

from the experimental cross-section using the multipole decomposition analysis. The (d,^{2}He) event generator creates events based on the reaction cross-section, ensuring a realistic representation of the process. The number of counts in each bin of θ_{cm} and ϵ_{pp} depends on the cross-section for that bin and the total number of events generated in the simulation.

4.6.2 Event Digitizer

This stage follows the event generator and is comparable to the unpacking of raw data during the experimental phase. Its primary objective is to simulate the detector's response to the tracks generated in the previous stage. The stage consists of two key subroutines.

The first subroutine simulates electron diffusion, where the number of ionization electrons produced for each hit and the drift time of the electrons are calculated. Electron diffusion inside the AT-TPC volume introduces uncertainty in the reconstructed excitation energy. A larger diffusion parameter causes broader proton tracks, which subsequently degrade the precision of the track fitting. For the digitization stage of simulated events in our analysis, we utilized parameters that reflect the realistic conditions achieved with the AT-TPC filled with deuterium gas (D_2). Several experimental parameters such as the electric field, gas pressure, the average gain of the micromegas detector, the gain of the GET electronics, and the electron drift velocity are directly obtained from the experimental setup to ensure consistency. In addition to these, we employed realistic values for key gas properties such as the ionization energy of D_2, gas density, and the Fano factor of the gas, which is crucial for modeling ionization fluctuations. These values are crucial for simulating the electron transport properties and signal formation within the AT-TPC. Table 4.3 shows the values used for these parameters in the digitization process. Fig. 4.17 shows a projection of a simulated event with two tracks on the pad plane, providing a visual representation of how the diffusion and digitization stages influence the track shapes.

The second subroutine models the electronic response. The high gain required in the electronics for detecting proton tracks in the AT-TPC significantly increases the likelihood of detecting δ-rays, as previously discussed. To mitigate this, the output of this subroutine is coupled to an electronics response module, which simulates the signal for each pad. This is essential for realistic signal

Parameter	Value
Electric Field	5000 V/m
Gas Pressure	530 Torr
Average Gain of Micromegas Detector	1000
Gain of GET Electronics	1000
Electron Drift Velocity	0.89 cm/μs
Ionization Energy of D_2	13.6 eV
Gas Density	0.1143 kg/m^3
Fano Factor of D_2	0.24
Longitudal Coefficient of Electron Diffusion	0.0038 1/m
Transverse Coefficient of Electron Diffusion	0.0014 1/m

Table 4.3 Parameters and their corresponding values used in the digitization of events in the AT-TPC.

processing in the analysis pipeline.

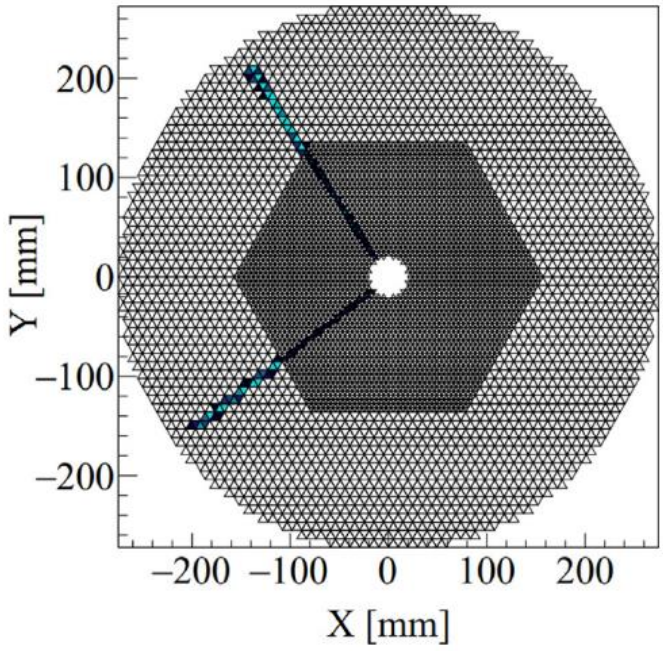

Figure 4.17 Projection of simulated (d,^{2}He) event on the Micromegas plane. Beam-like particles pass through the 3 cm aperture in the central region. Figure obtained from Ref. [109].

4.6.3 Reconstruction

Once the events are generated and the detector response is accounted for, the reconstruction stage of the simulation mirrors the process used for experimental data. Similar to experimental data, the RANSAC algorithm is employed to fit the particle tracks for all events, and to identify the $(d,^2\mathrm{He})$ reactions. The momenta of the two recoiling protons are extracted, allowing for the reconstruction of ϵ_{pp} through an invariant-mass calculation. A missing-mass calculation is performed to reconstruct the excitation energy spectrum of the ejectile. Mathematical details of the invariant-mass and missing-mass calculations are provided in Sec. 4.7. Fig. 4.18 illustrates the reconstructed excitation energy for the ground state in ^{33}Mg. The simulated ground state has an energy resolution of approximately 0.5 MeV.

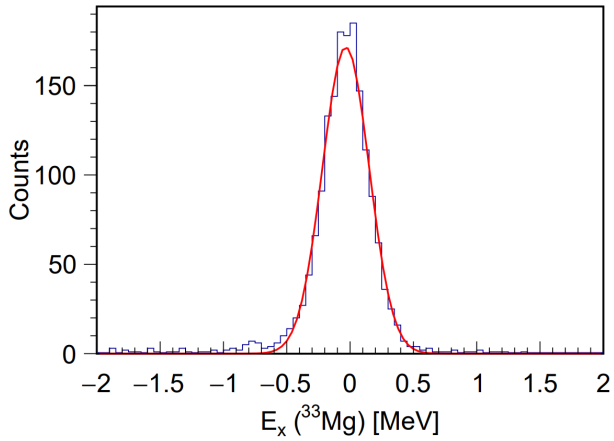

Figure 4.18 Simulated reconstructed excitation energy of ^{33}Mg ground state with a full width at half maximum of about 0.5 MeV.

4.6.4 Acceptance Corrections

The simulation is used for the acceptance corrections for the detection of two protons from the ^{2}He particle and the residual nucleus in the focal plane of the S800 are crucial for extracting accurate differential cross-sections.

It is insightful to look at the correlation between ϵ_{pp} and $\theta_{c.m.}$ in the first $(d,^2\mathrm{He})$ experiment for the ^{14}O beam channel to understand how the acceptance varies with the reaction kinematics. Fig. 4.19 illustrates the correlation between ϵ_{pp} and $\theta_{c.m.}$ for the transition from ^{14}O(0^+; ground

state) to ^{14}N(1$^+$; 3.95 MeV), which was the strongest transition observed in the first (d,^{2}He) experiment. The ground state Q value of this reaction is 3.702 MeV, which is relatively small. As a result, the momentum transfer during the reaction remains small at low center-of-mass scattering angles ($\theta_{c.m.} < 2°$). At low values of ϵ_{pp}(< 1 MeV), the protons produced in the reaction do not have sufficient energy to escape the central, insensitive region of the AT-TPC. Therefore, higher ϵ_{pp} values are required for both protons to be detected. On the other hand, at higher $\theta_{c.m.}$, the momentum transfer increases, leading to higher-energy protons. When this occurs, one or both of the protons may escape the active volume of the AT-TPC, making their reconstruction difficult or impossible. Consequently, for larger angles ($\theta_{c.m.} > 4°$), the analysis is restricted to lower ϵ_{pp} values (< 1.5 MeV), as can be observed in Fig. 4.19.

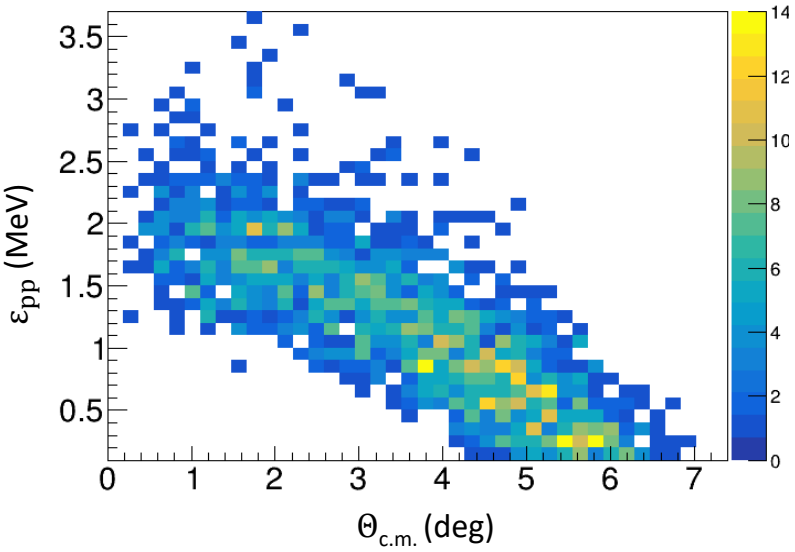

Figure 4.19 Correlation between the relative proton energy ϵ_{pp} and the center-of-mass scattering angle $\theta_{\text{c.m.}}$ for the experimental data from the ^{14}O(d,^{2}He)^{14}N reaction inside the sensitive region of AT-TPC. The figure has been taken from Ref. [70].

The Q-value for the ^{33}Al(d,^{2}He) reaction is -14.902 MeV for the ground state resulting in a higher momentum transfer for the reconstructed ^{2}He in the ^{33}Al reaction. As a result, for $\theta_{c.m.} \approx 0°$, protons from the ^{2}He decay with $\epsilon_{pp} > 0.5$ MeV are able to escape the central, insensitive region of the AT-TPC, unlike in the ^{14}O(d,^{2}He) reaction where higher ϵ_{pp} is required for this to occur. However, at moderately high values of $\epsilon_{pp} > 2$ MeV and $\theta_{c.m.} > 6°$, the protons are more likely to

escape the active volume of the AT-TPC due to the larger momentum transfer, as seen in Fig. 4.20. This explains why for the ^{14}O(d,^{2}He) reaction, events can be detected up to $\epsilon_{pp} \approx 3.5$ MeV, whereas in the case of the ^{33}Al(d,^{2}He) reaction, detection is constrained to $\epsilon_{pp} \approx 2$ MeV. Similarly, the center-of-mass angle $\theta_{c.m.}$ can reach up to 7° for the ^{14}O(d,^{2}He) reaction, but is mostly limited to 6° for the ^{33}Al(d,^{2}He) reaction.

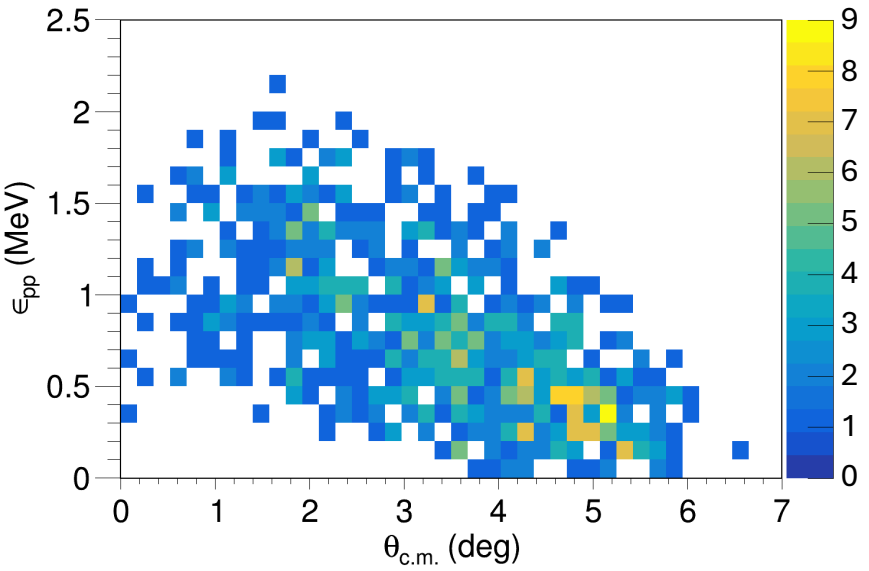

Figure 4.20 Correlation between the relative proton energy ϵ_{pp} and the center-of-mass scattering angle $\theta_{\mathrm{c.m.}}$ for the experimental data from the ^{33}Al(d,^{2}He)^{33}Mg reaction inside the sensitive region of AT-TPC.

Simulations are crucial for accounting the differences in detector acceptance arising from the specific kinematics of each reaction. Fig. 4.21(a) and 4.21(b) show the correlation between ϵ_{pp} and $\theta_{c.m.}$ from simulations run with an input energy of 8 MeV for the monopole ($\Delta L = 0$) and dipole ($\Delta L = 1$) cross-sections from ACCBA, respectively.

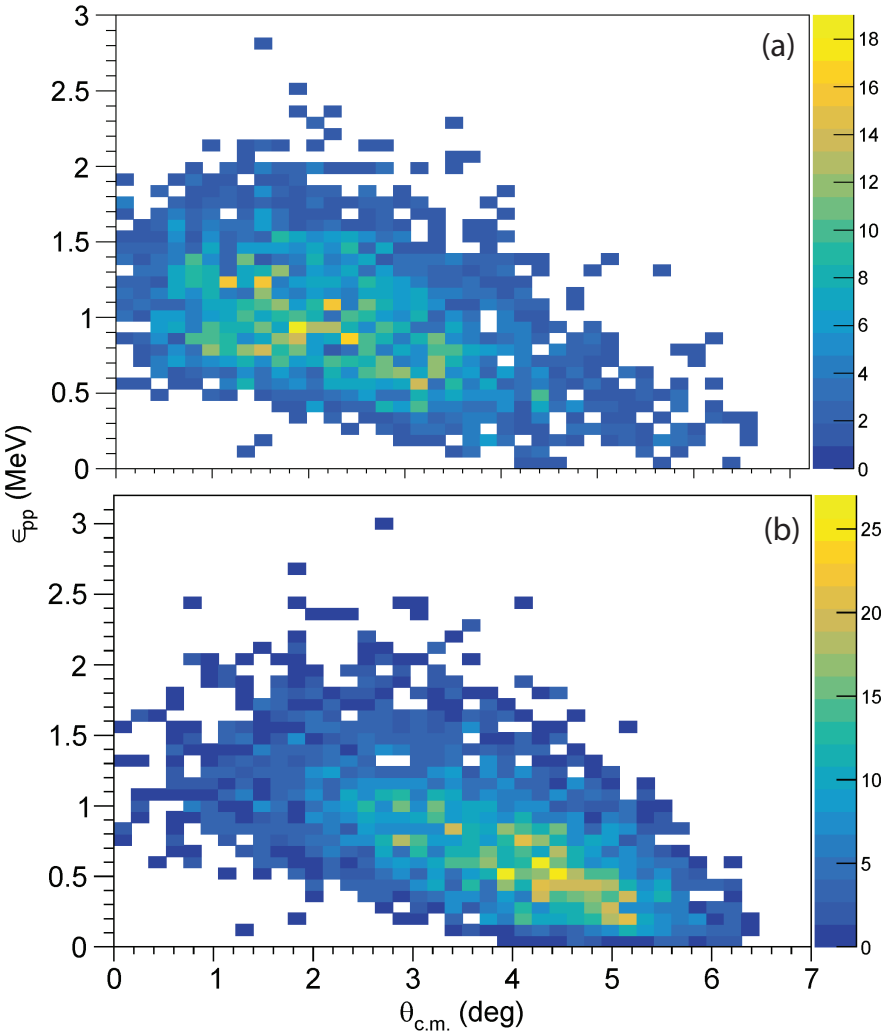

Figure 4.21 Simulated correlation between ϵ_{pp} and $\theta_{c.m.}$ for 8 MeV input energy. (a) Shows the correlation for monopole transitions ($\Delta L = 0$) and (b) for dipole transitions ($\Delta L = 1$), based on cross-sections from ACCBA.

Additionally, the correlation observed in Fig. 4.19 and 4.20 is impacted by the excitation energy of the residual nucleus. As the excitation energy increases, it results in greater momentum transfer to the ^{2}He system and an increase in the energy of the two protons. These effects are included in the simulation.

When the excitation energy surpasses the threshold for particle emission, the momentum-kick from the emitted particles affect the residual particle's momentum, causing a broadening in both momentum and angular distributions. This broadening can lead to a loss of events due to the limited

momentum and angular acceptances of the S800. The AT-TPC exit hole has a diameter of 4 cm, which also contributes to event loss due to the expanded angular distribution. When determining the cross section, the S800's acceptance must be taken into account. Two key factors contribute to losses: (1) a portion of the momentum distribution lies outside the S800's momentum acceptance, and (2) some beam residues are lost due to the limited size of the AT-TPC exit hole. This loss is more significant for lighter residues because they receive a larger momentum kick from neutron or proton decay. In the first (d,^{2}He) experiment conducted in inverse kinematics with ^{14}O and ^{13}N beams, more events were lost at higher excitation energies, as many did not reach the S800 focal plane. Specifically, 31% of ^{32}Na fragments were lost due to the S800 acceptance limits, while all other fragments were fully transmitted to the focal plane.

4.7 Kinematic Event Reconstruction

The energies of the protons in the (d,^{2}He) events were determined from their path lengths using an energy-loss look-up table calculated using SRIM[118], as illustrated in Fig. 4.22.

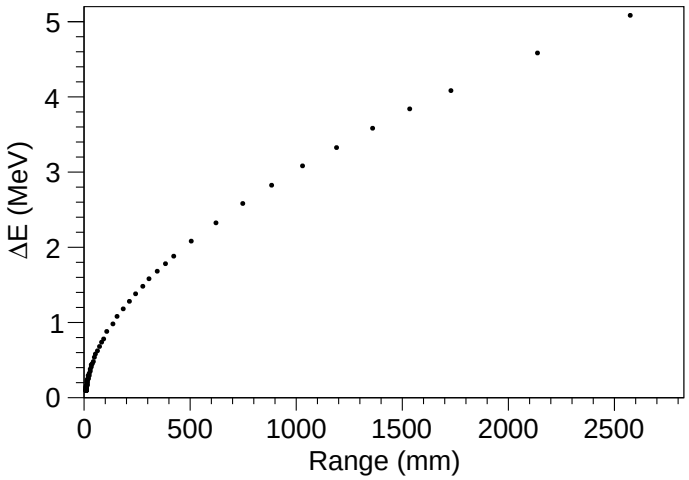

Figure 4.22 Energy loss as a function of proton path lengths calculated using SRIM.

The path lengths and track angles were used to reconstruct the momentum vectors of the two protons, $\vec{P}_{p_1}$ and $\vec{P}_{p_2}$. The momentum of the ^{2}He were then calculated from the proton tracks using the momentum conservation:

$$\vec{P}_{^2He} = \vec{P}_{p_1} + \vec{P}_{p_2}, \tag{4.20}$$

The total mass of the ^{2}He system, $M_{^2He}$, was obtained using an invariant-mass calculation:

$$M_{^2He} = \sqrt{(E_{p_1} + E_{p_2})^2 - P^2_{^2\mathrm{He}}}, \tag{4.21}$$

where E_{p_1} and E_{p_2} are the energies of the two protons. The relative energies between the two protons, ϵ_{pp}, can then be calculated using the following equation:

$$\epsilon_{pp} = M_{^2He} - 2m_p, \tag{4.22}$$

where m_p is the mass of a proton. The ϵ_{pp} is used in the missing-mass calculation, which is then used for the excitation-energy reconstruction. In order to find the missing mass, it is important to first find the missing energy and the missing momentum. The missing energy, M.E., is calculated by:

$$M.E. = E_{\mathrm{beam}} + m_{\mathrm{beam}} + m_d - (E_{^2\mathrm{He}} + \epsilon_{pp} + m_{^2\mathrm{He}} + 0.511), \tag{4.23}$$

where E_{beam} and m_{beam} are the kinetic energy and mass of the projectile beam, m_d is the mass of target deuteron, $E_{^2\mathrm{He}}$ is the kinetic energy of the reconstructed ^{2}He, $m_{^2\mathrm{He}}$ is the mass of ^{2}He, and 0.511 is the rest energy of an electron in MeV. The kinetic energy of the ^{2}He particle is calculated using:

$$E_{^2\mathrm{He}} = \sqrt{\vec{P}^2_{^2\mathrm{He}} + M^2_{^2He}} - M_{^2He} \tag{4.24}$$

The missing momentum, $M.P.$, can be simply calculated using:

$$M.P. = \sqrt{\vec{P}^2_{\mathrm{beam}} - \vec{P}^2_{_{2\mathrm{He}}}} \tag{4.25}$$

where $\vec{P}_{\mathrm{beam}}$ is the momentum of the projectile beam. We calculate the missing mass, $M.M.$:

$$M.M. = \sqrt{M.E.^2 - M.P.^2} \tag{4.26}$$

Finally, we can calculate the reconstructed excitation energy:

$$E_x = M.M. - m_{\text{prod}} \tag{4.27}$$

where m_{prod} is the rest mass of the reaction product.

The theoretical and experimental kinematics of the ^{33}Al(d,^{2}He) reaction are shown in Fig. 4.23. The theoretical calculations (represented by circles) are calculated with $\epsilon_{pp} = 0$ MeV, while the experimental data (represented by diamonds) span a range of ϵ_{pp} values. This variation in ϵ_{pp} leads to an upward shift in the experimental data compared to the theoretical predictions.

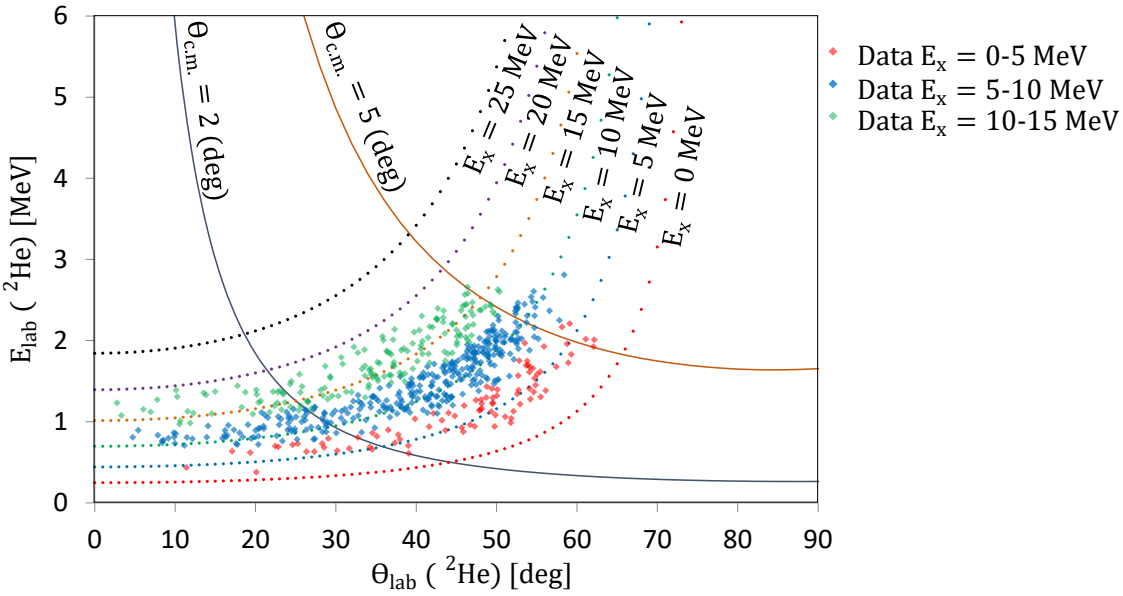

Figure 4.23 Theoretical (circles) and experimental (diamonds) kinematics of the ^{33}Al(d,^{2}He) reaction. The theoretical kinematics are calculated for $\epsilon_{pp} = 0$ MeV, while the experimental data correspond to a range of ϵ_{pp} values, leading to the observed upward shift relative to theory.

4.8 Event Selection

Fig. 4.24 illustrates the excitation energy spectrum derived from the calculation after applying a gate on the ^{33}Al beam. In this plot, noticeable background contributions appear at both negative-

and high-energy regions. These background contributions are attributed to various sources. It is important to apply additional gates to filter out these background events.

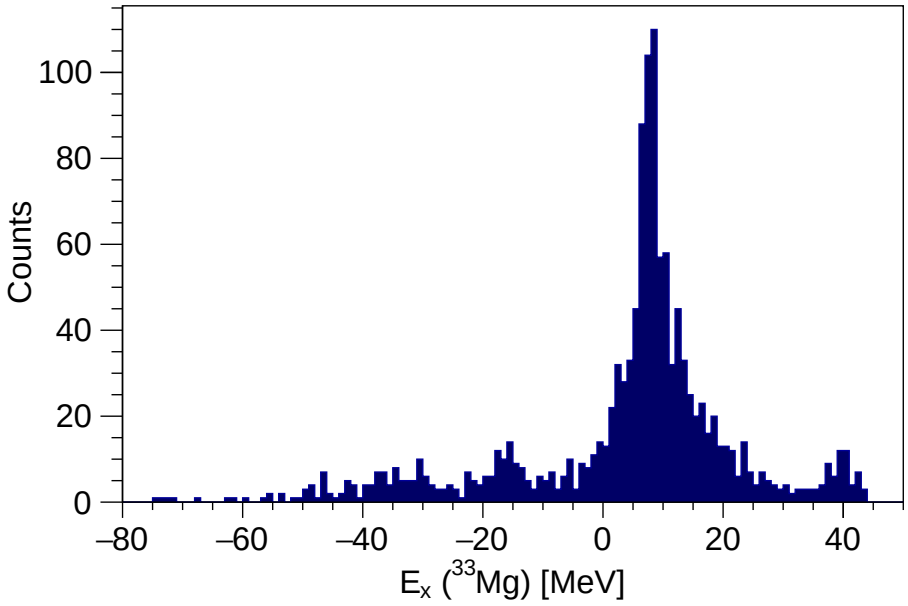

Figure 4.24 Excitation energy spectrum of the ^{33}Al(d,^{2}He)^{33}Mg reaction. The background contributions arise from various sources, with elastic scattering events being the predominant factor.

Fig. 4.25 shows a plot of the scattering angles of two proton tracks (θ_1 and θ_2) relative to the beam axis. The red squares represent events with excitation energies above 0 MeV in Fig. 4.24, while the blue squares represent those below 0 MeV. A band near 1.57 radians appears in both θ_1 and θ_2. This pattern is consistent with elastic scattering of deuterium off the beam, which peaks at 0° in the c.m. frame and near 90° in the laboratory frame. As the cross section for elastic scattering is very high, there is a chance that two of such events happen within a short time and sufficiently close in distance to create a random 2-track coincidence event creating background for the (d,^{2}He) channel. A second cluster of events is visible near 0 radians for θ_2. These events are due to a high event rate in a few pads of the pad plane, associated with the beam hitting these pads, or noisy/sparking pads, introducing background. However, by setting a gate on the angular correlation spectrum of Fig. 4.25, this background can be removed.

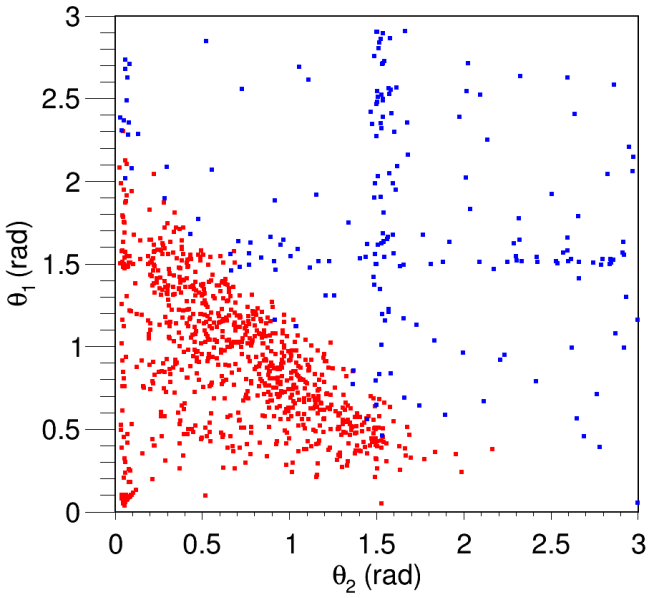

Figure 4.25 Correlation between the proton track angles, θ_1 and θ_2. The red triangles represent events with excitation energies greater than 0 MeV, while the blue squares correspond to events with excitation energies below 0 MeV. A distinct pattern is evident, particularly with bands at $\theta_1 \approx 1.57$ rad and $\theta_2 \approx 1.57$ rad indicating the presence of elastic scattering events.

To determine the appropriate size of the gate in the correlation between θ_1 and θ_2, we used the simulation framework. Fig. 4.26 illustrates the simulated proton angles, along with the gate drawn around the valid (d,^{2}He) events. This gate was be applied to the experimental data to largely filter out the background events.

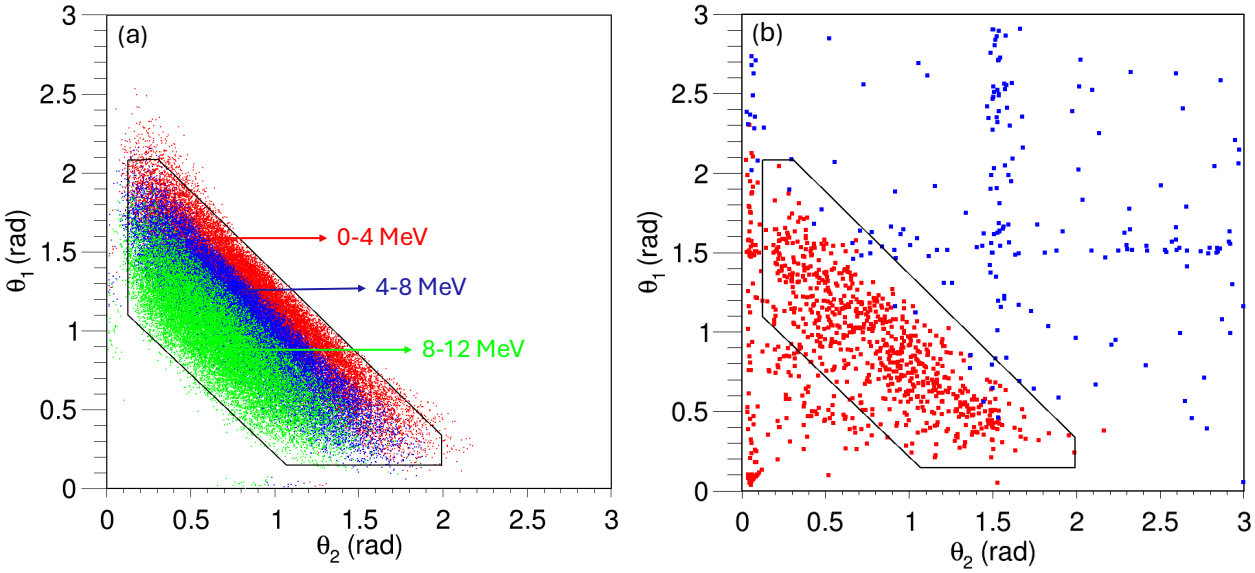

Figure 4.26 (a) Correlation between proton track angles, θ_1 and θ_2, from simulated events across different excitation energy ranges. Red corresponds to the 0-4 MeV range, blue to the 4-8 MeV range, and green to the 8-12 MeV range. The black gate highlights the region used in the analysis to select only good (d,^{2} He) events. (b) The gate obtained from simulated data has been applied to the data.

4.9 Excitation Energy Spectra and Differential Cross-Sections

Fig. 4.27 shows the excitation energy spectra for: (a) ^{33}Mg, obtained by selecting events with both ^{33}Mg recoil and its decay product, ^{32}Mg; and (b) ^{32}Na, created by selecting events with ^{32}Na recoil and its decay product, ^{31}Na. The excitation energy was calculated using Eq. 4.27.

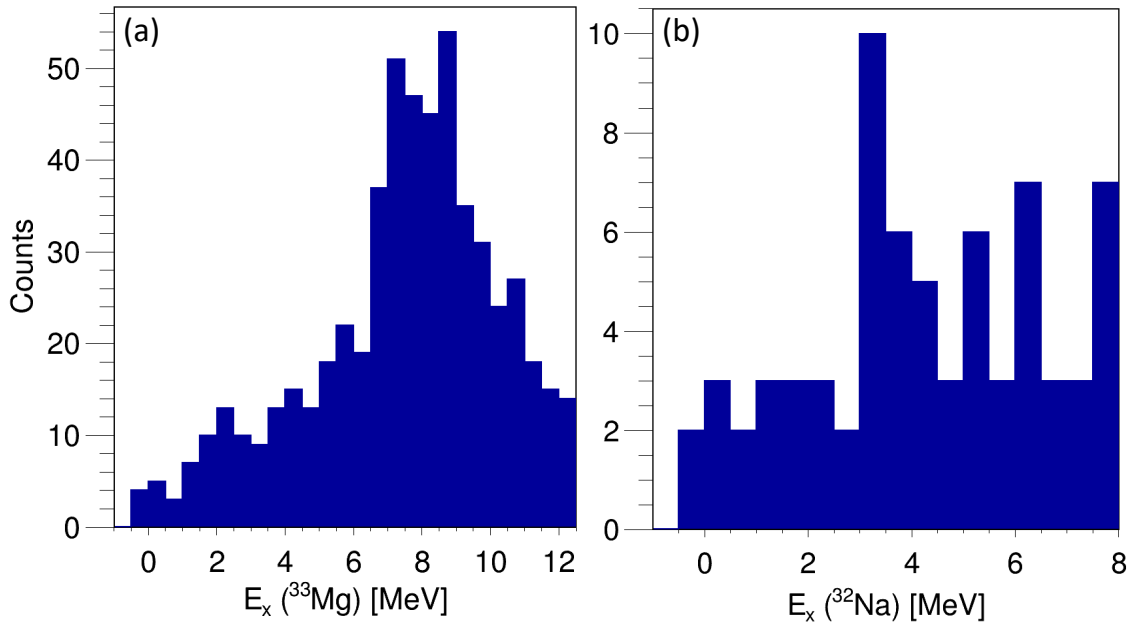

Figure 4.27 Excitation energy spectra of (a) ^{33}Al(d,^{2})He) and (b) ^{32}Mg(d,^{2})He) reactions.

The differential cross-sections are calculated for energy bins using the following formula:

$$\frac{d\sigma}{d\Omega} = \frac{N_{bin}}{N_{beam} \cdot \Delta\Omega \cdot N_{target} \cdot \varepsilon} \tag{4.28}$$

where N_{bin} is the number of counts in each energy bin, N_{beam} is the number of beam particles, $\Delta\Omega$ is the solid angle, N_{target} is the number of target particles. ε accounts for the S800 acceptance of residuals and the acceptance of the two protons inside the AT-TPC, combined with corrections applied due to all the gates used in the analysis. The beam particle count, N_{beam}, is weighted by the transmission efficiency of 31.2% from the object scintillator to the focal plane. N_{target} is calculated as:

$$N_{target} = \frac{\rho_A \cdot N_A}{M_{D_2}} \tag{4.29}$$

where $\rho_A = 11.69$ mg/cm^2 is the surface density, $N_A = 6.02 \times 10^{23}$ is the Avogadro's number, and $M_{D_2} = 4028$ mg/mol is the molar mass for D_2 gas.

Fig. 4.28 shows the integrated cross-sections as a function of E_x for $\theta_{c.m.}$ less than 6°: (a) for the ^{33}Al(d,^{2}He)^{33}Mg reaction and (b) for the ^{32}Mg(d,^{2}He)^{32}Na reaction.

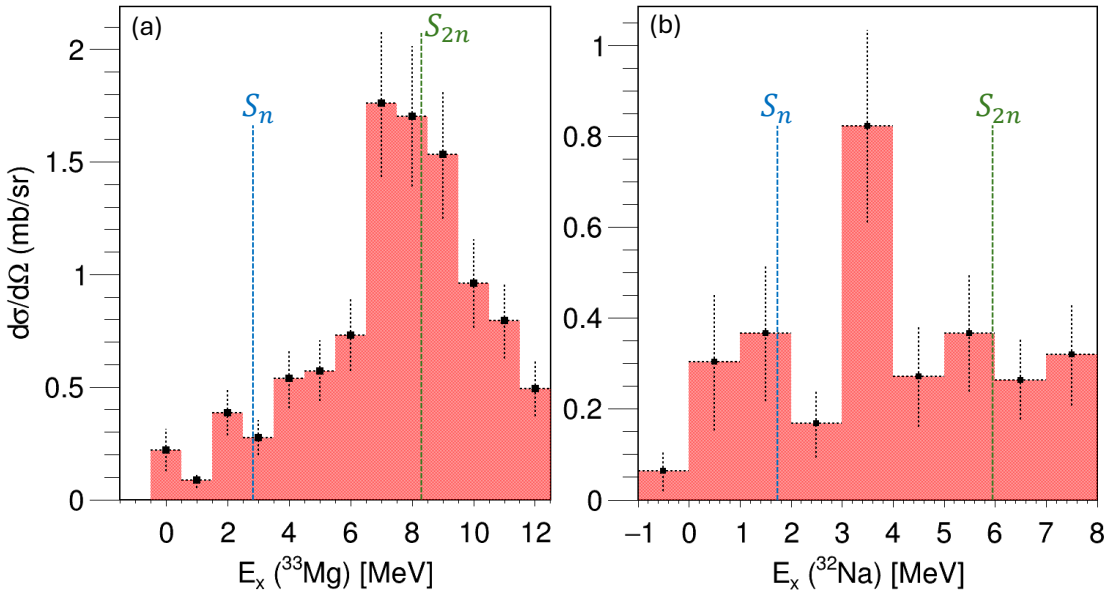

Figure 4.28 Differential cross-sections for: (a) ^{33}Al(d,^{2}He)^{33}Mg and (b) ^{32}Mg(d,^{2}He)^{32}Na reactions. The dashed lines represent the separation energies. (a) and (b) show differential cross-section up to 12 MeV and 8 MeV, respectively, but may have missing cross-section above S_{2n} as ^{31}Mg and ^{30}Na fragments were not detected in the S800 focal plane for the chosen B_ρ setting.

Differential cross-sections were also calculated as a function of $\theta_{c.m.}$. Fig. 4.29 shows angular distributions for the ^{33}Al(d,^{2}He)^{33}Mg reaction. Subfigures correspond to the following energy ranges: (a) -1 to 1 MeV, (b) 1-4 MeV, (c) 4-6 MeV, (d) 6-8 MeV, (e) 8-10 MeV, and (f) 10-12 MeV.

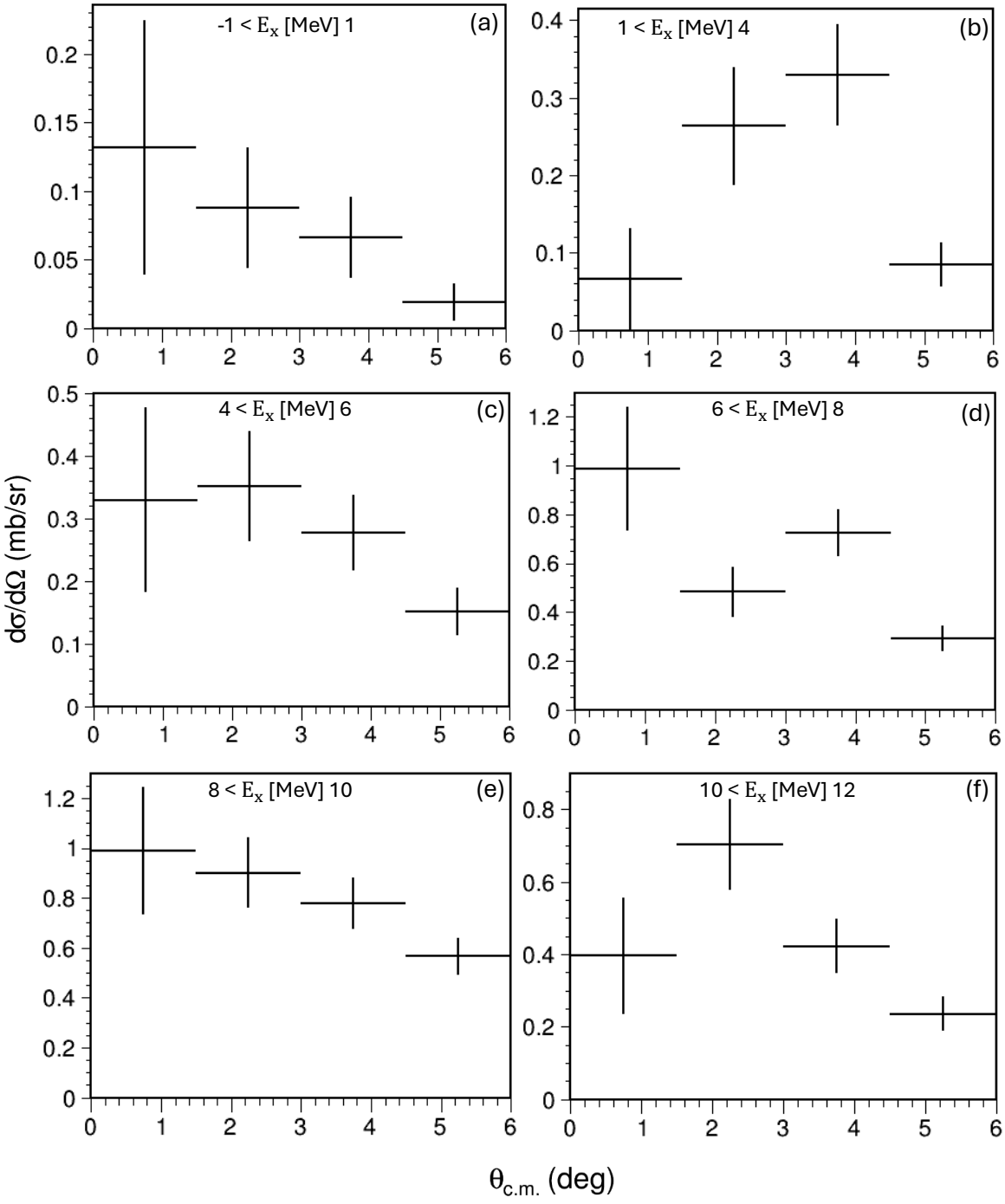

Figure 4.29 Angular distributions of differential cross-sections for the ^{33}Al(d,^{2}He)^{33}Mg reaction for different energy ranges.

Similarly, Fig. 4.30 shows angular distributions for the ^{32}Mg(d,^{2}He)^{32}Na reaction. Subfigures correspond to the following energy ranges: (a) -1 to 1 MeV and (b)-(f) 1-MeV-wide intervals up to

6 MeV.

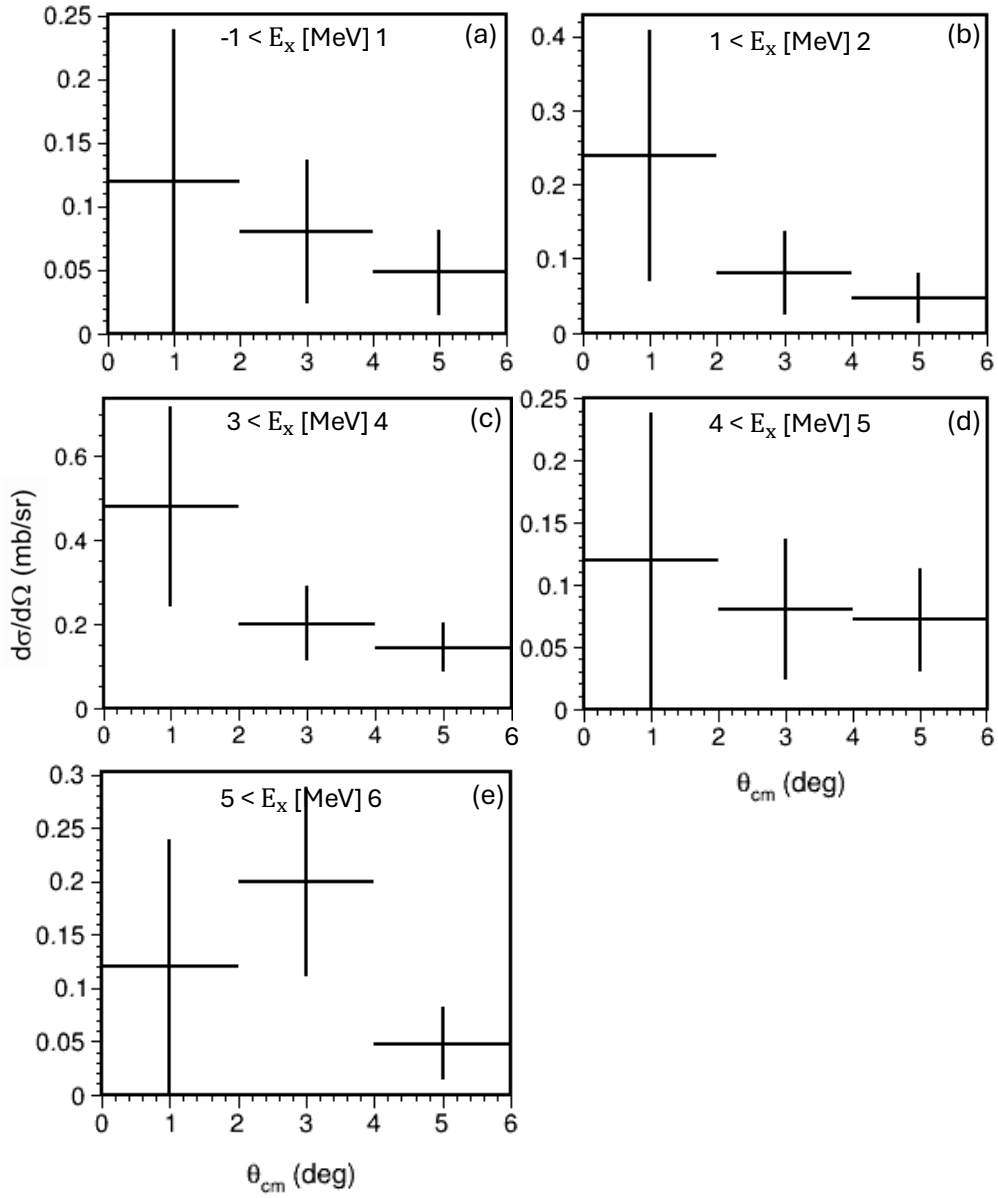

Figure 4.30 Angular distributions of differential cross-sections for the ^{32}Mg(d,^{2}He)^{32}Na reaction for different energy ranges.

The vertical error bars in all differential cross-section plots represent statistical uncertainties. The horizontal bars in the angular distribution plots indicate the bin widths of the angular intervals. The systematic uncertainty from all gating conditions was negligible compared to the statistical uncertainty and was therefore excluded from the analysis.

4.10 Multipole Decomposition Analysis

As described in Chap. 2, the differential cross-section from the experimental data can have contributions from various ΔL components. We use the MDA to extract GT component ($\Delta L = 0$) of the differential cross-section using Eq. 2.1.

4.10.1 ^{33}Al(d,^{2}He)^{33}Mg Reaction

A state is observed at $E_x(^{33}\mathrm{Mg}) \sim 0$ MeV (see Fig. 4.29). The angular distribution of this state peaks at 0°, as illustrated by Fig. 4.29(a). This is indicative of a $\Delta L = 0$ transition, and thus a GT transition. As discussed in Sec. 1.2, a GT transition from the $(5/2)^+$ ground state to the ground state in ^{33}Mg is highly unlikely, as current evidence points to the ground state of ^{33}Mg having a spin-parity of $3/2^-$ [41, 42, 43]. States at 484 keV and 546 keV are tentatively identified as having spin-parities of $(5/2^-)$ and $(3/2^-)$ [119], respectively, although Ref. [43] suggested a positive parity for the 484 keV state. A state at 705 keV has tentatively been assigned a spin-parity of $(3/2, 5/2^+)$. Since the uncertainty in the reconstructed excitation energy due to uncertainty in drift velocity is ~100 keV (see Sec 4.5), it is unlikely that the observed state is associated with any of the excited states at 484 keV or above. We concluded that the observed state is likely a low-lying excited state previously unobserved. However, since the statistical uncertainties are large, it was also investigated whether a misidentification is possible, and if it is a dipole transition to the ground state.

Due to the properties of the nucleon-nucleon interaction, transitions to final states that can be associated with $\Delta L = 0$, also have $\Delta L = 2$ contributions. Fig. 4.31(a) shows a fit of the angular distribution with $\Delta L = 0$ and $\Delta L = 2$ contributions, resulting in reduced χ^2 of 0.29. Fig. 4.31(b) shows a fit with a $\Delta L = 1$ angular distribution, resulting in a reduced χ^2 of 0.95. While we cannot rule out that the transition proceeds with $\Delta L = 1$, it is more likely that there is a strong $\Delta L = 0$ component.

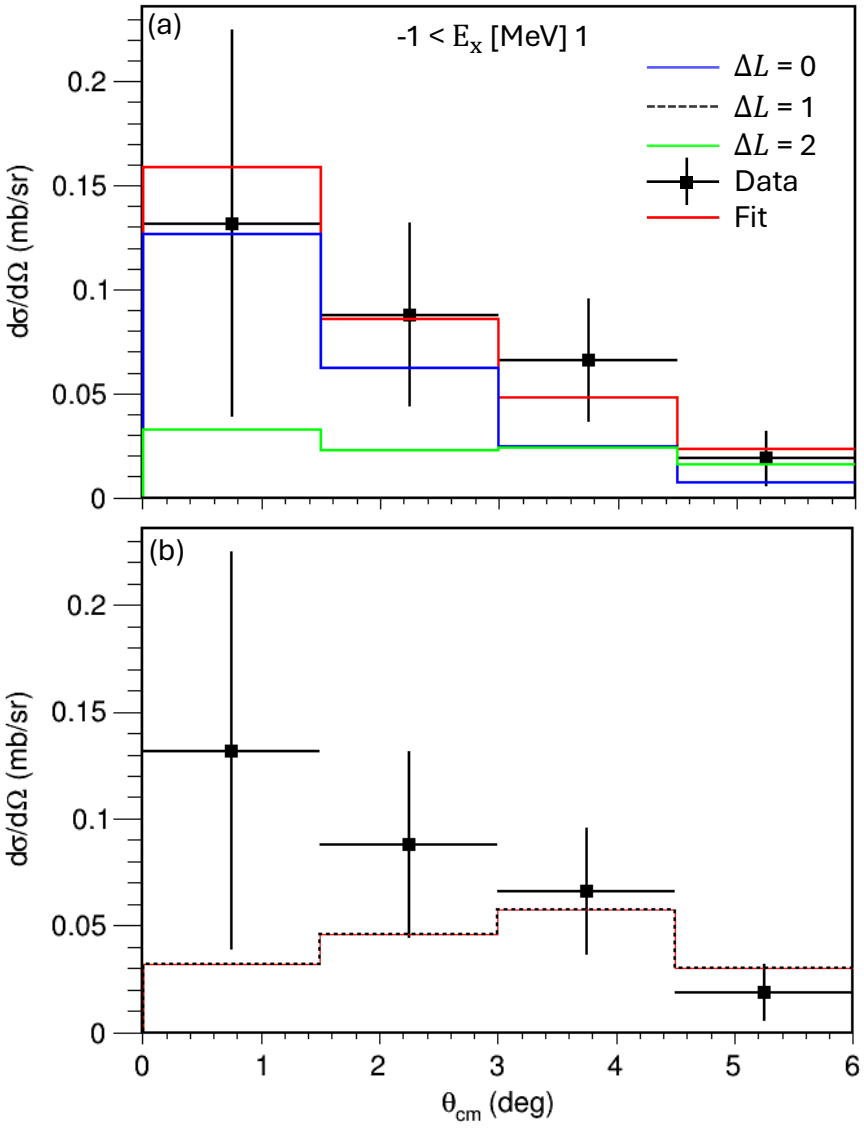

Figure 4.31 MDA fit of the experimental angular distribution for the ^{33}Mg between -1 and 1 MeV in the ^{33}Al(d,^{2}He) reaction and the simulated angular distribution at 0 MeV.

The experimental angular distributions for other energy ranges in Fig 4.29(b)-(f) were also fit with simulated angular distributions. Ref. [43] proposed spin-parities of $1/2^-$ and $3/2^-$ for the states at 1.24 MeV and 1.85 MeV. In our analysis, the angular distribution in the 1 to 4 MeV range is dominated by dipole ($\Delta L = 1$) contributions, as illustrated in Fig. 4.32, although minor other contributions are not excluded.

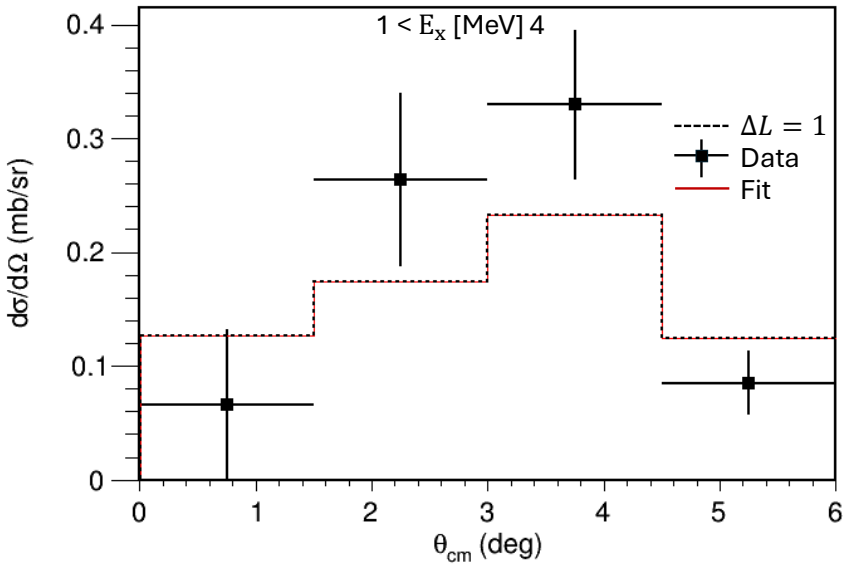

Figure 4.32 Fit of the experimental angular distribution for the ^{33}Al(d,^{2}He) reaction between 1 and 4 MeV and the simulated $\Delta L = 1$ angular distribution at 2.5 MeV.

For all angular distributions with $E_x > 4$ MeV, the angular distributions can be reproduced by assuming dominant quadrupole transitions ($\Delta L = 2$). Fig. 4.33 shows the fit for the following energy ranges: (a) 4-6 MeV, (b) 6-8 MeV, (c) 8-10 MeV, and (d) 10-12 MeV. There is no prior experimental information available for states at these energies, and based on the fit results, it is not possible to assign any B(GT) to states at these excitation energies.

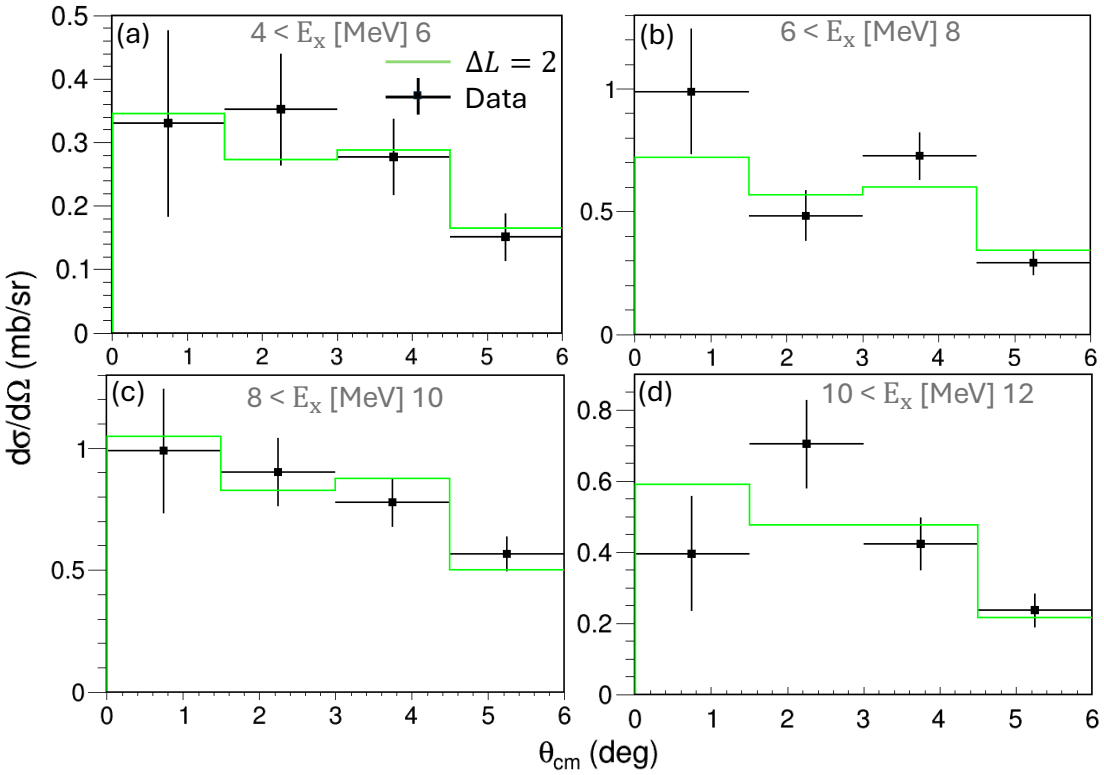

Figure 4.33 MDA fit of the experimental angular distribution for the ^{33}Al(d,^{2}He) reaction for the energy ranges: (a) 4-6 MeV, (b) 6-8 MeV, (c) 8-10 MeV, and (d) 10-12 MeV with the simulated angular distribution for: (a) 5 MeV, (b) 7 MeV, (c) 9 MeV, and (d) 11 MeV.

4.10.2 ^{32}Mg(d,^{2}He)^{32}Na Reaction

The strongest peak in the ^{32}Mg(d,^{2}He)^{32}Na reaction differential cross-section spectrum occurs between 3 and 4 MeV, with the peak occurring between 3 and 3.5 MeV (see Fig. 4.27). As the width of this peak is close to the experimental resolution of 0.5 MeV, it is likely that this peak belongs to a single excited state. The state peaks at forward angles indicating a $\Delta L = 0$ transition. We fit the experimental differential cross section in this energy range with simulated differential cross-sections for $\Delta L = 0$ and $\Delta L = 2$ components at $E_x = 3.5$ MeV, shown in Fig. 4.34.

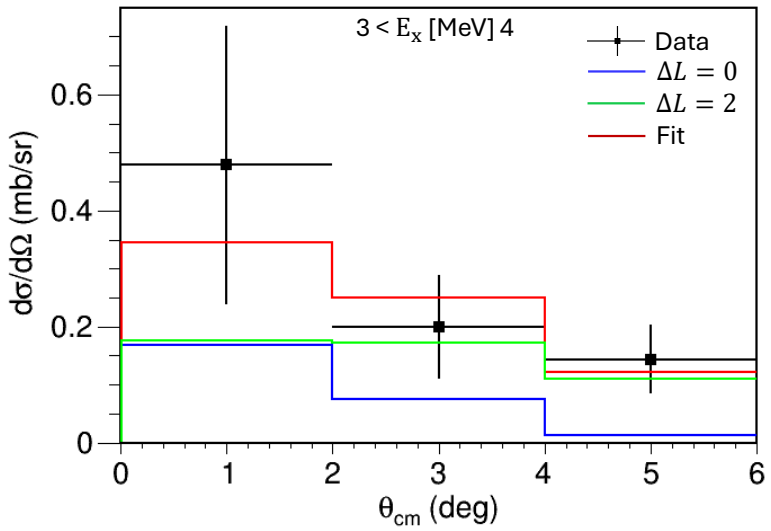

Figure 4.34 MDA performed for the ^{32}Mg(d,^{2}He) reaction in the 3 to 4 MeV excitation energy range, with simulated angular distributions for $\Delta L = 0$ and $\Delta L = 2$ at 3.5 MeV.

The forward peaking behavior in the angular distribution was also observed between 1 and 2 MeV in Fig. 4.30. To extract the GT transition in this region, we fit the experimental differential cross section in this energy range with simulated differential cross-sections for $\Delta L = 0$ and $\Delta L = 2$ components, shown in Figs. 4.35(a) and (b), respectively, at $E_x = 1.5$ MeV.

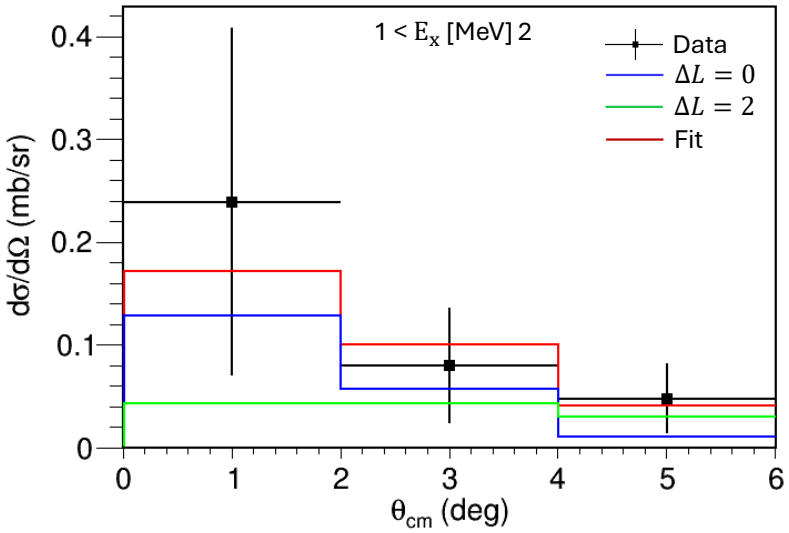

Figure 4.35 MDA performed for the ^{32}Mg(d,^{2}He) reaction in the 1 to 2 MeV excitation energy range, with simulated angular distributions for $\Delta L = 0$ and $\Delta L = 2$ at 1.5 MeV.

For the energy ranges -1 to 1 MeV and 4 to 5 MeV, the angular distributions are likely dominated

by the quadrupole ($\Delta L = 2$) contribution, as shown in Figs. 4.36(a) and (b). However, the statistical uncertainties are so large it is difficult to be sure about the nature of transitions in these excitation energy ranges.

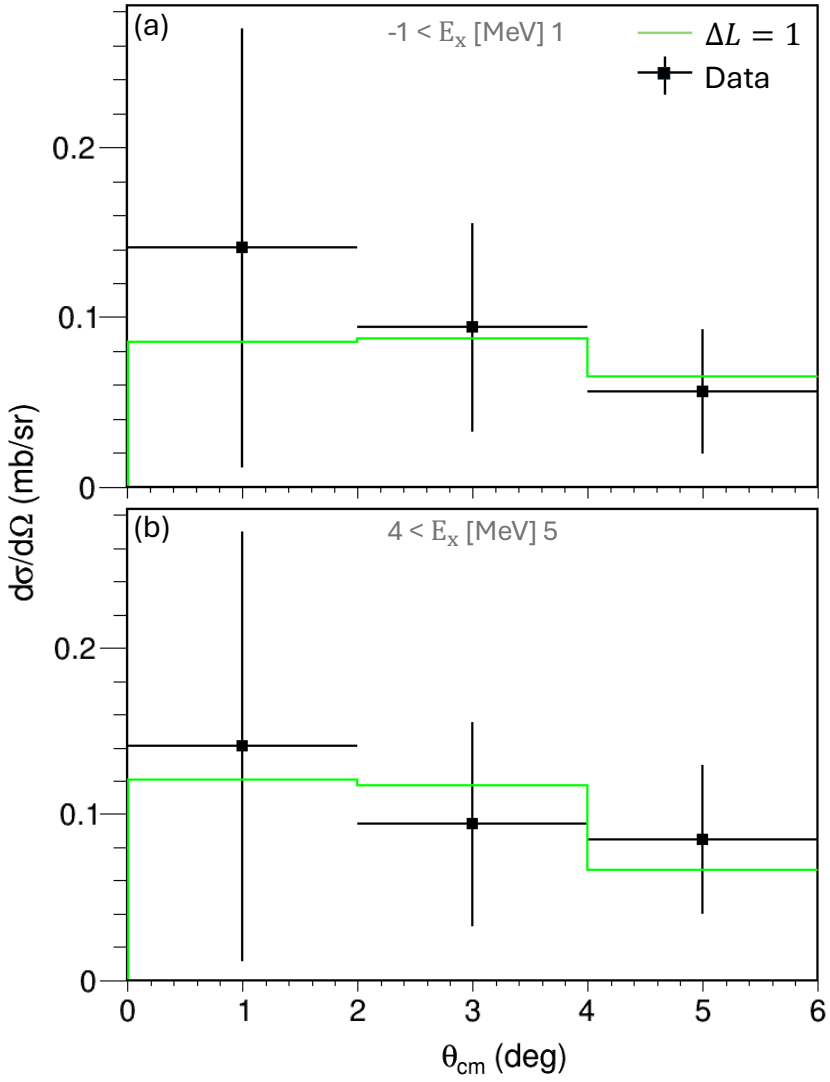

Figure 4.36 Fit of the experimental angular distribution for the ^{32}Mg(d,^{2}He) reaction with the $\Delta L = 2$ for the energy ranges: (a) -1 to 1 MeV and (b) 4 to 5 MeV with simulated angular distribution for: (a) 0 MeV and (b) 4.5 MeV.

Finally, the angular distribution for the 5-6 MeV range appears to be dominated by dipole ($\Delta L = 1$) transition, as shown by Fig. 4.37. The statistical uncertainties are too large to draw a definitive conclusion.

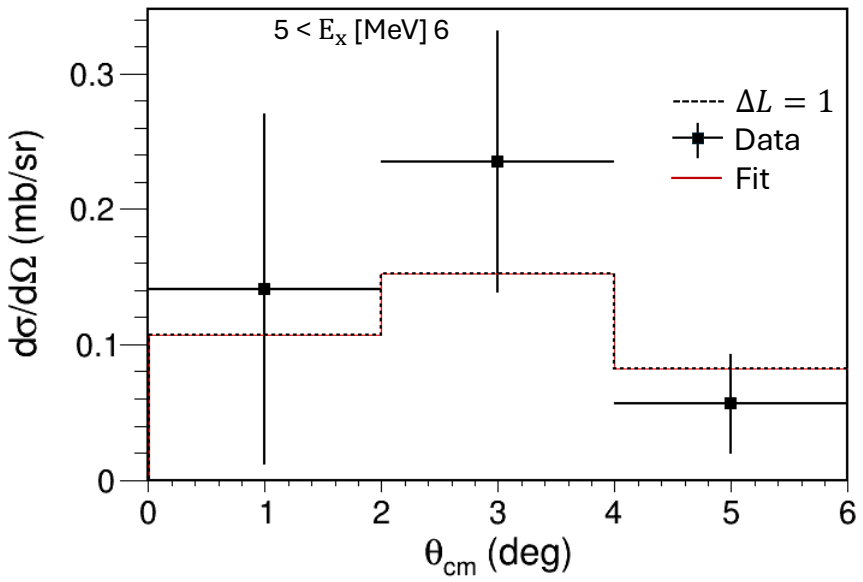

Figure 4.37 MDA fit of the experimental angular distribution for the ^{32}Mg(d,^{2}He) reaction with simulated angular distributions for: (a) -1 to 1 MeV and (b) 5 to 6 MeV.

4.11 B(GT) Extraction

The differential cross-sections were extrapolated to values at zero momentum transfer ($q = 0$) and $\epsilon_{pp} < 1$ MeV. This extrapolation was carried out using DWBA calculations with the ACCBA code and the simulation. The relationship used in the extrapolation is given by:

$$\begin{aligned}\frac{d\sigma}{d\Omega}(\theta \approx 0^\circ,\ q = 0,\ \epsilon_{pp} < 1\,\text{MeV}) = &\left(\frac{\frac{d\sigma}{d\Omega}(\theta \approx 0^\circ,\ q = 0,\ \epsilon_{pp} < 1\,\text{MeV})}{\frac{d\sigma}{d\Omega}(\theta \approx 0^\circ,\ q,\ \epsilon_{pp} < 1\,\text{MeV})}\right)_{\text{ACCBA}} \\ &\times \left(\frac{\frac{d\sigma}{d\Omega}(\theta \approx 0^\circ,\ q,\ \epsilon_{pp} < 1\,\text{MeV})}{\frac{d\sigma}{d\Omega}(\theta,\ q,\ \epsilon_{pp})}\right)_{\text{Simulation}} \\ &\times \left(\frac{d\sigma}{d\Omega}(\theta \approx 0^\circ,\ q,\ \epsilon_{pp})\right)_{\text{exp}}. \end{aligned} \tag{4.30}$$

In this equation, the third term of the product is the extracted experimental differential cross section at the lowest θ bin. The second term extrapolates the experimental differential cross section to $\epsilon_{pp} < 1$ MeV based on the simulated acceptance. And the first term extrapolated the differential cross section to $q = 0$.

The B(GT) was calculated from the extrapolated differential cross section at low scattering angles and $\epsilon_{pp} < 1$ MeV using the proportionality relationship in Eq. 1.12. The value of $\hat{\sigma}$ used for calculating B(GT) from the extrapolated cross-section was obtained from the ^{32}S(d,^{2}He) reaction study for $\epsilon_{pp} < 1$ MeV [120]. For different CE reactions, it has been shown that the unit cross section varies smoothly with mass number A [121], therefore, using a known unit cross section for $A = 32$ is reasonable for the systems studied here. Even though there is limited experience with nuclei far away from the valley of stability, which could introduce systematic uncertainties, these uncertainties are significantly smaller than the statistical uncertainties reported here. For the ^{32}S(d,^{2}He) reaction, the unit cross section could be determined from 4 transitions, at $E_x = 1.15$ MeV, 4.06 MeV, 5.41 MeV, and 6.65 MeV, with B(GT) = 0.344 ± 0.004, 1.005 ± 0.006, 0.087 ± 0.002, and 0.068 ± 0.023, respectively. To determine the unit cross section for the reactions studied here, we only included the transition with the high B(GT)s, since for states with low B(GT), a larger systematic uncertainty is expected [77]. The extracted unit cross section was 1.868 ± 0.100.

For the ^{33}Al(d,^{2}He)^{33}Mg reaction, the B(GT) could only be extracted for the transition to the lowest lying state. The extracted B(GT) was = 0.062 ± 0.041. Fig. 4.38 compares the extracted B(GT) value with shell-model predictions (see Sec. 2.2). The vertical error bar indicates the uncertainty in B(GT). The horizontal error bar reflects the uncertainty in excitation energy, arising from the peak resolution of 200 keV and 100 keV uncertainty due to the drift velocity correction (see Sec. 4.5). In other energy regions, the fit results showed that the angular distributions were dominated by dipole or quadrupole contributions and given the statistical uncertainties, no B(GT) could be extracted.

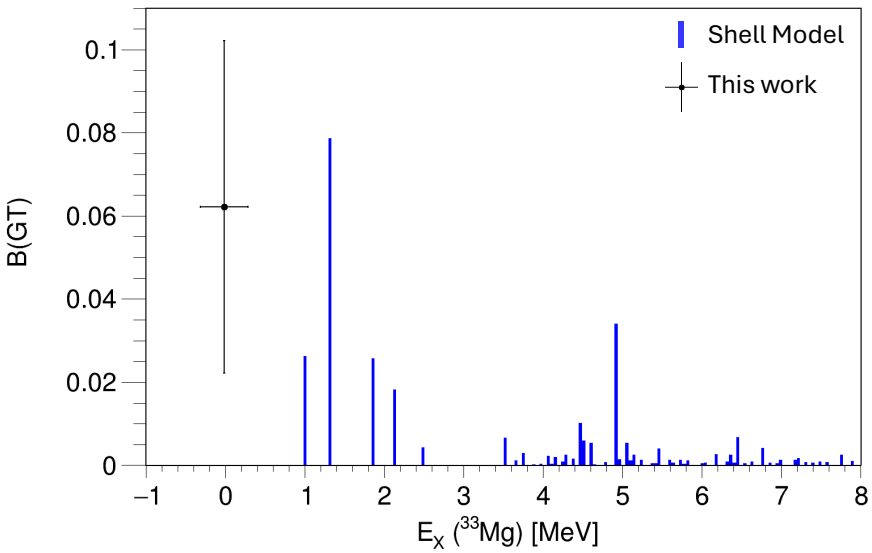

Figure 4.38 Comparison of extracted B(GT) values with shell-model predictions for the ^{33}Al(d,^{2}He)^{33}Mg reaction. A phenomenological quenching factor of 0.55 has been applied to the shell-model calculations.

For the ^{32}Mg(d,^{2}He)^{32}Na reaction, the B(GT) was extracted in the 1-2 MeV and 3-4 MeV excitation energy ranges. We obtained B(GT) = 0.06 ± 0.05 for the 1–2 MeV range and B(GT) = 0.07 ± 0.06 for the 3–4 MeV range. The B(GT) was not extracted for other excitation energies because dipole and quadrupole contributions dominated. Fig. 4.39(a) compares the extracted B(GT) values with shell-model predictions for this reaction. The vertical error bars in Fig. 4.39(a) represent the uncertainty from the angular distributions fits, consistent with the analysis of ^{33}Al(d,^{2}He)^{33}Mg. The horizontal error bars indicate the excitation energy ranges analyzed for the GT transition. Fig. 4.39(b) shows the summed B(GT) up to 6 MeV from this work and the shell-model calculations.

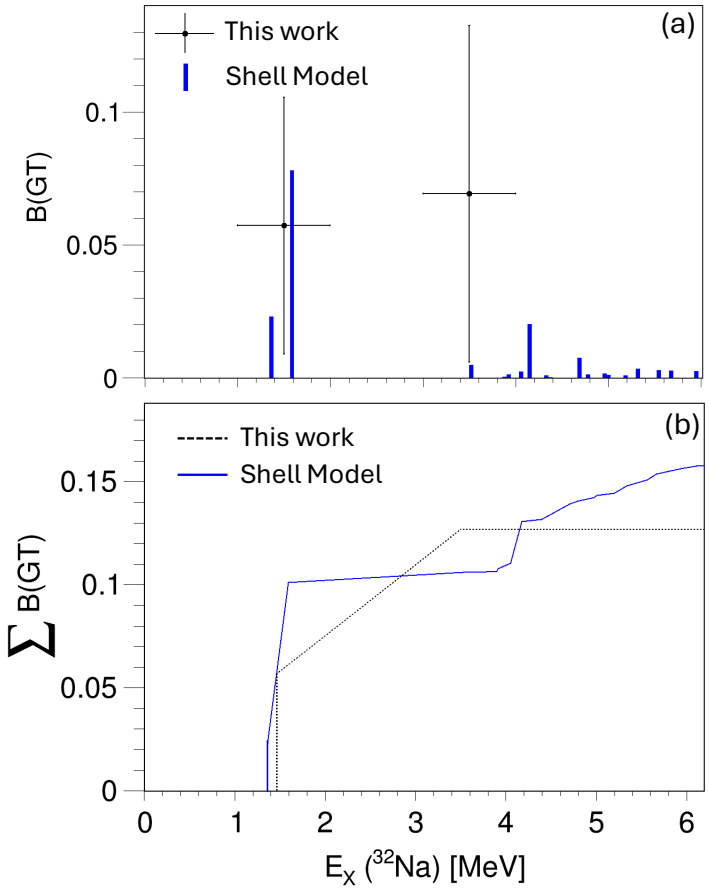

Figure 4.39 (a) Extracted B(GT) values from this work compared with shell-model predictions for the ^{32}Mg(d,^{2}He)^{32}Na reaction. (b) Summed B(GT) from this work compared with shell-model predictions. A phenomenological quenching factor of 0.55 has been applied to the shell-model calculations.

4.12 B(GT) Comparison with Theory

For the GT strength from ^{33}Al, the shell-model calculations shown in Fig. 4.38 do not predict a low-lying state near 0 MeV. However, the predicted B(GT) for a state at roughly 1.3 MeV is comparable to the experimental B(GT) extracted for state near 0 MeV. Furthermore, the shell model predicts additional states above 1.5 MeV with non-zero B(GT) values. These states could not be identified in the data, but given the small predicted strengths and the significant contribution from transitions with $\Delta L > 0$ in the experimental data, the presence of some GT strength at higher excitation energy cannot be ruled out.

For the ^{32}Mg(d,^{2}He)^{32}Na reaction, the experimentally extracted B(GT) between 1 MeV and

2 MeV agrees well with the shell-model prediction for a state near 1.6 MeV, despite the large uncertainties arising from low statistics (see Fig. 4.39(a)). The shell-model calculations have some strength at higher excitation energy, but it is rather fragmented. We observe a transition to a state at ~3.5 MeV that is likely associated with a GT transition (see Fig. 4.28(b)). As shown in Fig. 4.39(b), the summed B(GT) measured in this work is in reasonable agreement with the shell-model predictions, although the error bars are large.

The observation of a GT transition from ^{33}Al to ^{33}Mg highlights the importance of including pf-shell configurations in describing nuclei in this region, and confirms that ^{33}Al ground state has a significant $pf-$shell component in its wavefunction. Meanwhile, ^{32}Mg is already established to be part of the island of inversion, and the extracted B(GT)s for the ^{32}Mg(d,^{2}He)^{32}Na reaction provides further evidence for this. In addition, further refinements to the shell model, along with experiments offering improved statistics, would help confirm these findings and reduce the associated uncertainties.

CHAPTER 5

NEUTRON STAR CRUST SIMULATION

We ran simulations for neutron star crust using **xnet**, a nuclear reaction network that accounts for all possible reactions in the crust and has been used to simulate the heating and cooling in neutron star crusts in Ref. [12]. **xnet** calculates the EC and the β^- decay rates from a set of input files provided by the user. First, we ran **xnet** with inputs calculated with QRPA calculations from Ref. [15]. We then repeated the simulation by replacing these inputs with shell-model calculations for sd- and pf-shell nuclei, using USDB [122] and GXPF1 [123] interactions, respectively. In addition, we ran another version of the simulation where we incorporated β^- decay experimental data for the sd- and pf- shell nuclei where available from the Nudat database by National Nuclear Data Center (NNDC). For the calculation of EC rates, experimental data from charge-exchange reactions were also used in the input files if available. In cases where no experimental data were available to calculate EC rates, we used Eq. 1.5 to determine the ground-state EC rates. To ensure consistency, everything except the inputs for calculating EC and β^- decay rates remained unchanged across all three versions used in the simulation.

The neutron star simulation uses the dynamic model described in Ref. [7]. The neutron star structure is adopted from Ref. [124] and the thermal structure is based on the calculations from Ref. [125]. The model incorporates EC rates, neutron-capture rates, and pycnonuclear-fusion rates, which are coupled to a thermal model of the neutron star crust. It also includes important processes such as neutrino cooling and heat transport. In addition to the energy lost via neutrinos emitted during the Urca process, neutrino pair bremsstrahlung is generated when electrons scatter off the Coulomb field of nuclei in the crust, providing an additional cooling mechanism [126]. The reaction network used in the model includes approximately over 3000 isotopes and spans from the valley of stability to regions beyond the neutron-drip line.

In the model, the crust is a plane-parallel slab in a local Newtonian frame, where Newtonian mechanics are a valid approximation, with constant gravity g, set to the value of 1.85×10^{14} cm/s^2. The composition changes of an accreted fluid element is induced by the increasing pressure

$P = \dot{m}gt$, where $\dot{m}$ is the local accretion rate and t is the time. It determines the steady-state of the composition of the crust. The mass density is calculated using an equation of state $P = P(T, \rho, Y_i)$ where T is the temperature, ρ is density, and Y_i is the nuclear abundance [127]. Y_i includes the neutron abundance as well.

The astrophysical parameters used in the simulation are realistic for a neutron star and the same as those used in Ref. [12]. The mass and radius of the neutron star are fixed at 1.4 solar mass and 10 km, respectively. The mass accretion rate, $\dot{M}$, is fixed at 0.3 $\dot{m}_{\rm Edd}$, where $\dot{m}_{\rm Edd}$ is the Eddington mass accretion rate- defined as the rate at which the gravitational energy released by the in-falling matter produces the maximum luminosity for a star in hydrostatic equilibrium. The local accretion rate per unit area, $A\dot{M}$, is set to 2.637×10^4 g s^{-1} cm^{-2}. We started all of our calculations at a density of $\rho = 1.4 \times 10^9$ g cm^{-3}.

Nuclear masses are a critical input for the reaction network, influencing the calculation of phase space for EC and β^- decay rates, as well as photodisintegration and neutron-capture rates. Neutron-capture rates are computed assuming a Maxwell-Boltzmann distribution [7] and the photodisintegration rates are derived using a detailed balance [128]. Additionally, nuclear masses determine the Q value of reaction processes, significantly impacting the phase space of the electrons. In the neutron star crust simulation, theoretical masses are taken from the Finite Range Droplet Mass Model (FRDM) [129], which is a macroscopic model augmented by microscopic corrections for shell and pairing effects. To maintain consistency, the FRDM is used for calculating EC and β^- decay strength functions for nuclei with $Z > 7$. For nuclei with $Z \leq 7$ and very neutron-rich isotopes, the analytical Hilf mass formula [130], a semi-empirical atomic mass model, is applied. Where available, experimental nuclear masses were also incorporated.

Building on this framework, we focus on heating and cooling in the neutron star crust. As discussed in Sec. 1.1, two-step ECs are among the strongest heating sources, while the Urca process is the main cooling mechanism. The strength of the transitions in these reactions is given by the ft value thant can be calculated from B(GT) using Eq. 1.4. The strength of an Urca pair can be estimated from its β^- decay flow, which measures how quickly β^- decay transforms one

nucleus into another during nucleosynthesis. In this work, we compare heating generated from ECs and different Urca cycles' contributions to cooling. The Urca cooling strength is calculated using time-integrated reaction flow, measured relative to the strongest Urca pair.

We ran three versions of the simulation, each using different input files for EC and β^- decay and will be referred to as Model 1, 2, and 3 from this point onward. The inputs used in these models are as follows:

- **Model 1**: All inputs from QRPA.
- **Model 2**: Shell-model inputs for sd and pf shells, with all other inputs from QRPA.
- **Model 3**: Data incorporated into shell-model inputs in Model 2 where available, otherwise kept unchanged from Model 2.

Fig. 5.1 shows the nuclear chart with the inputs used for each isotope in the reaction network. To ensure consistency, we used the same input model for both EC and β^- decay rates within each Urca pair. However, different inputs were allowed for the same isotope for EC and β^- decay. For example, ^{18}O and ^{18}F form a potential Urca pair where ^{18}O undergoes β^- decay to ^{18}F, and ^{18}F undergoes EC to regenerate ^{18}O. For this pair, only shell-model inputs were used to ensure consistency. On the other hand, ^{18}F and ^{18}Ne form another potential Urca pair, but shell-model inputs were unavailable for ^{18}Ne EC rates. In this case, we used QRPA inputs for EC and β^- decay rates of ^{18}Ne and ^{18}F, respectively, maintaining input consistency within the pair even though different models were allowed for EC and β^- decay rates of the same isotope.

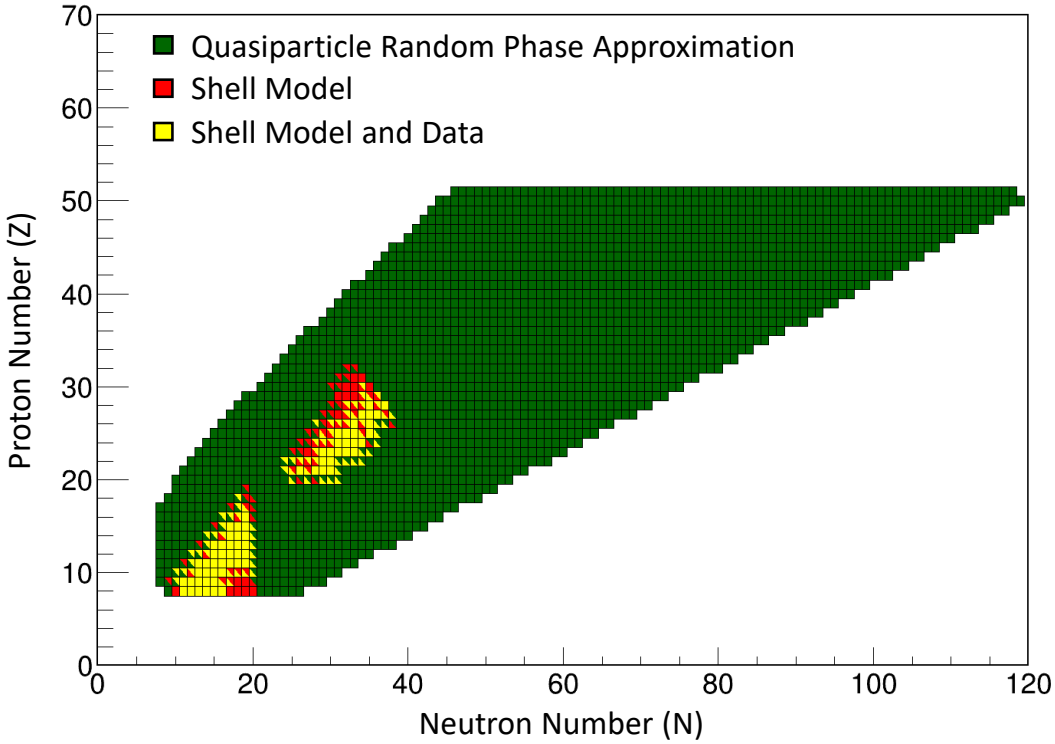

Figure 5.1 Nuclear chart illustrating the input models used for each isotope in the simulation. Green squares represent isotopes where only QRPA calculations were used for Models 1, 2, and 3; red squares indicate the use of shell-model inputs for Models 2 and 3; and yellow squares highlight isotopes where experimental data were incorporated in Model 3. Squares with mixed colors represent isotopes where different models were used for EC and β^- decay rates for the same isotope for Models 2 and 3.

5.1 Using the Neutron Star Crust Simulation Code

The EC and β^- decay rates were calculated in the simulation dynamically using input files that we provide to the simulation framework. For EC rates, the calculation relies on a table of B(GT)s as a function of excitation energy, with the assumption that the parent nucleus is always in its ground state. For relatively low temperatures (T <1 GK) in the neutron star crust, it is a reasonable assumption for neutron stars [131]. Four specific input files are required to compute the EC rates within the framework. The naming and formatting conventions for these files are detailed in Ref. [132]. The four input files primarily contain the following information:

1. Parent nucleus ground state spin
2. List of daughter states

3. Log(ft) values for transitions from the parent ground state to the daughter states

4. Nuclear properties of both the parent and daughter nuclei

In contrast, only a single input file is needed to calculate β^- decay rates. This file contains information about the atomic and mass numbers, the excitation energy of the parent, the excitation energy of the daughter nucleus, and the log(ft) value of the transition.

The initial composition for crust model depends on the system and depends on the composition of the accreted matter and the characteristics of surface burning processes such as X-ray bursts and superbursts. We can fix the abundance, Y, for each initial isotope, i, and the abundances are automatically normalized to:

$$\sum_i A_i Y_i = 1 \tag{5.1}$$

Table 5.1 lists the three key output files generated from the simulation along with their functions.

Input File	**Function**
abuntime	Records the abundances of isotopes over time.
totalenergy	Provides the energy at each timestep.
flux_movie	Details the reaction flows at each timestep.

Table 5.1 Description of key input files used in the simulation.

5.2 Calculation at $T = 0.5$ GK

In the simulation, we started the evolution at time $t = 1.4\times10^8$ s, with a temperature $T = 0.5$ GK, a mass density $\rho = 1.45\times10^9$ g/cm^3, and electron Fermi energy $E_F = 4.0$ MeV. Fig. 5.2 illustrates the initial isotopic abundances for superburst ashes as reported in Ref. [133]. This figure was generated from the "$flux\_movie$" output file produced by the simulation, and the initial composition was identical across all three models.

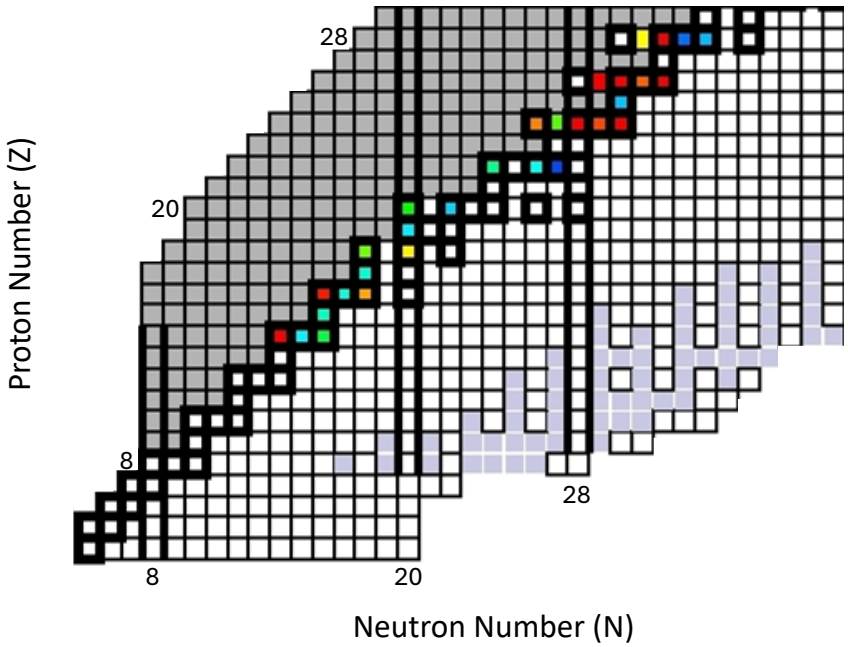

Figure 5.2 Initial composition at the start time of $t = 1.4 \times 10^8$ s for all three versions of data. The isotopic abundances are depicted on a logarithmic color scale ranging from blue (lowest) to green, yellow, orange, and red (highest). The lower cutoff is at 1.0×10^{-7}. Thick black squares indicate stable nuclei, while thin black squares represent unstable but particle-bound nuclei. Squares without outlines correspond to particle-unbound nuclei, and gray-shaded squares denote nuclei not included in the reaction network. The red diagonal lines represent EC reactions, while the blue diagonal lines indicate β^- decay reactions. Nuclei pairs connected by both red and blue lines simultaneously are identified as Urca pairs.

The deposition of integrated heat energy as a function of time for the different input sets are shown in Fig. 5.3, generated from the "*totalenergy*" file. The deposited heat energy per nucleon is calculated using the following equation:

$$dQ = dE_{nuc} + dE_e - dE_\nu \tag{5.2}$$

where $dE_{nuc} = \sum_i dY_i BE_i$ is the nuclear energy generation calculated from the abundance change dY_i and binding energy BE_i of each isotope i. $dE_e = E_F dY_e$ and dE_ν is the energy released as neutrinos from EC. In Fig. 5.3, the red line represents energy changes using Model 1, the green line corresponds to Model 2, and the blue line represents inputs for Model 3. Time = 0 s marks the start of accretion, but in Fig. 5.3 the time axis begins at 1.4E08 s, which corresponds to the occurrence of the superburst. In this figure, increases in energy are interpreted as heating and decreases as

cooling. Because the code calculates composition and energy generation as functions of depth under a steady state approximation, increasing time represents progression into deeper layers of the neutron star crust, where the pressure is higher. The upward trend observed in all three input models reflects increasing heating as the material moves into these deeper layers.

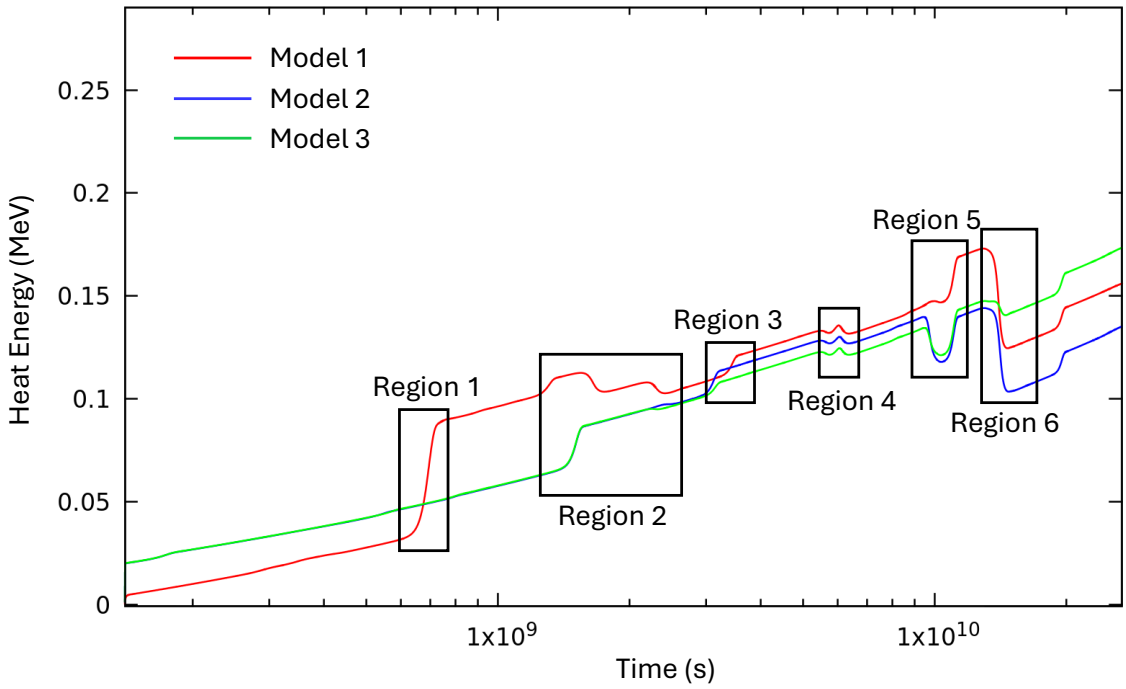

Figure 5.3 Energy evolution in the neutron star crust as a function of time for three different input sets. Time on x-axis is shown on a logarithmic scale. The red line corresponds to energy changes using Model 1 inputs, the green line represents inputs from Model 2, and the blue line illustrates the case for Model 3 inputs. Distinct regions of interest in the energy curve are labeled and highlighted.

Fig. 5.3 is divided into six regions where significant heating, cooling, or differences between the models are observed. To analyze these regions, the nuclei responsible for heating and cooling were identified by examining their abundances and reaction flows at specific timesteps. The input files for these isotopes were then reviewed to determine which parameters may be driving the observed variations in heating and cooling. Discussion on different regions identified in Fig. 5.3 is as follows.

5.2.1 Region 1

Region 1 spans the time interval from $t = 6.2 \times 10^8$ s to $t = 7.5 \times 10^8$. In this region, no difference in deposited heat energy is observed between Models 2 and 3. However, significant

heating is observed for Model 1. Fig. 5.4 illustrates the abundances of nuclei and the reactions occurring in Region 1 for Model 1.

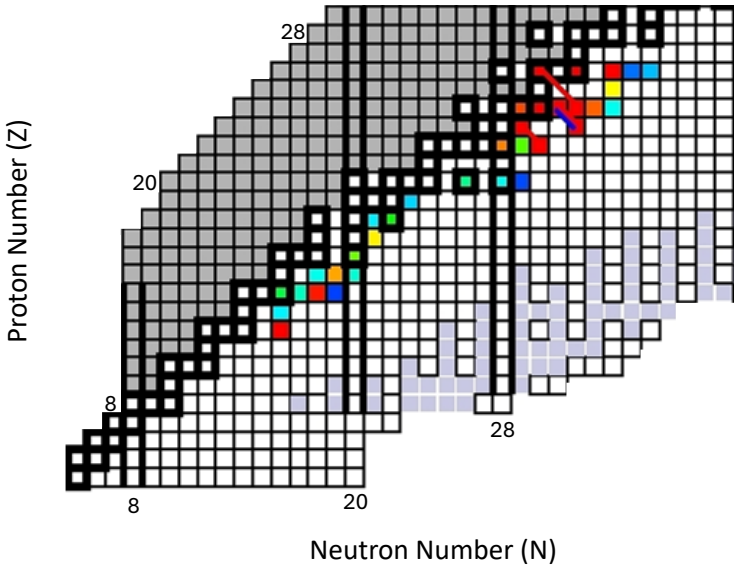

Figure 5.4 Isotopic abundances and reaction flows at $t = 7.2 \times 10^8$ s in Region 1, calculated using inputs from QRPA.

In Model 1, the primary contributor to heating is a two-step EC process: ^{56}Fe $\rightarrow$ ^{56}Mn $\rightarrow$ ^{56}Cr. Significant heat is deposited in the crust as both EC transitions occur for relatively highly excited states, leading to substantial energy release during the de-excitation of ^{56}Mn and ^{56}Cr, as illustrated in Fig. 5.5(a).

In contrast, Models 2 and 3 involve only a single EC transition from ^{56}Fe to ^{56}Mn. Moreover, in these models, the EC from ^{56}Fe proceeds to a low-lying state in ^{56}Mn, which deposits minimal energy into the crust upon de-excitation to the ground state. Notably, Model 3 incorporates experimental data for the ^{56}Fe $\rightarrow$ ^{56}Mn transition from Ref. [134], resulting in inputs that closely align with those of Model 2. It is concluded that the heating in Model 1 is artificial.

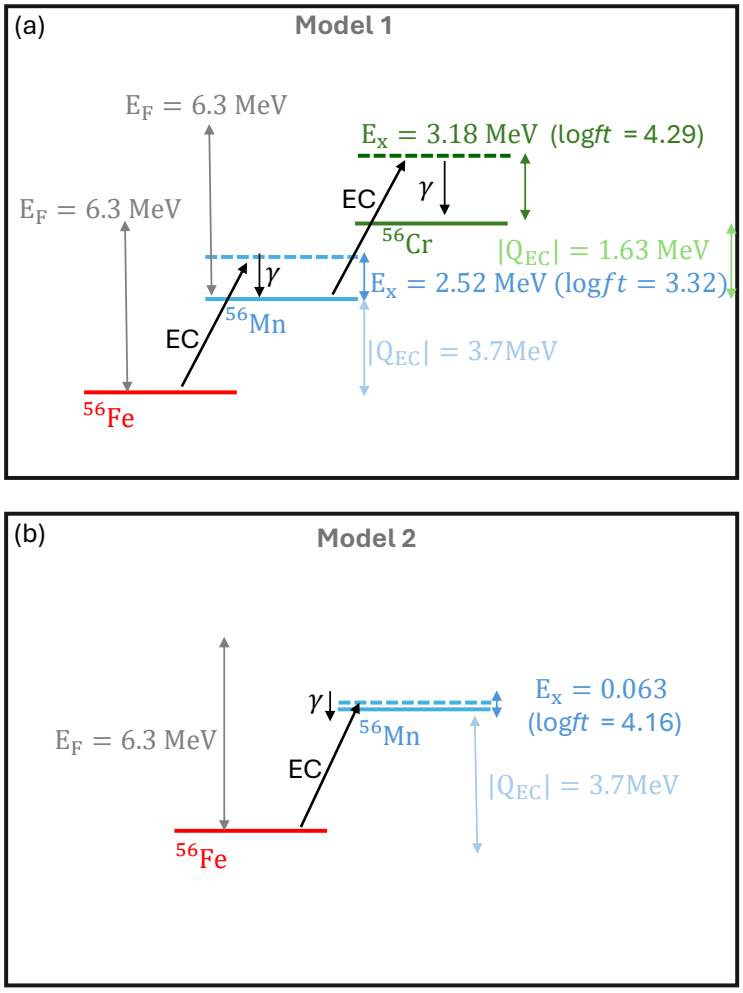

Figure 5.5 Energy level schemes in Region 1: (a) A two-step EC reaction from ^{56}Fe to ^{56}Cr in Model 1. (b) A single-step EC reaction from ^{56}Fe to ^{56}Mn in Model 2.

5.2.2 Region 2

Region 2 spans the time interval from $t = 1.2 \times 10^9$ s to $t = 2.5 \times 10^9$ s. Heating is observed across all three models. Model 1 exhibits lower heating that starts earlier in comparison to Models 2 and 3. Significant cooling is observed for Model 1 whereas the cooling in Models 2 and 3 are minimal. Fig. 5.6 shows the isotopic abundance and reaction flow for Model 2 at $t = 1.4 \times 10^9$ s.

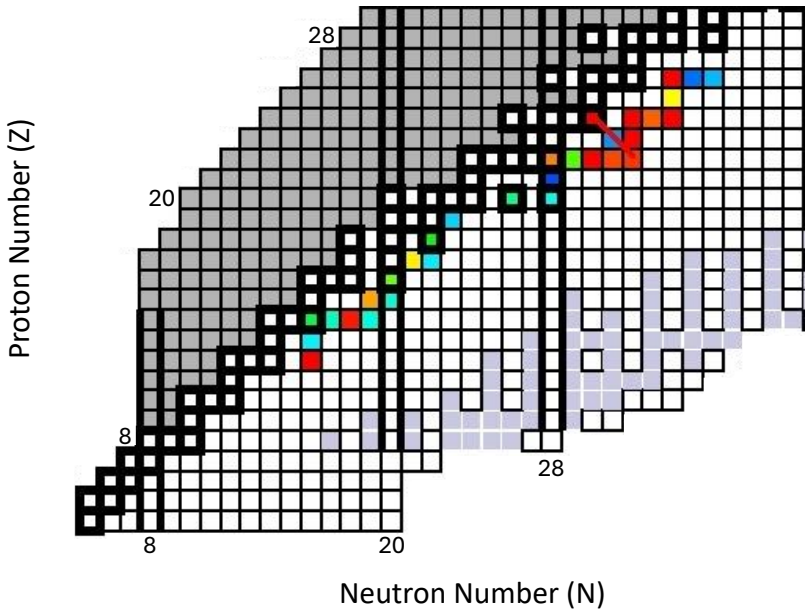

Figure 5.6 Isotopic abundances and reaction flows at $t = 1.4 \times 10^9$ s, calculated for Model 2 in Region 2.

In Fig. 5.6 at $t = 1.4 \times 10^9$ s, the significant source of heating is a two-step EC from ^{54}Cr to ^{54}Ti across all three models. Fig. 5.8 illustrates the energy level scheme for the ^{54}Cr→^{54}V→^{54}Ti transition for Models 1 and 2. No data was available for these nuclei, therefore, these inputs were kept unchanged from Model 2 for Model 3. In Model 1, EC from ^{54}Cr happens for a 0.07 MeV state in ^{54}Mn, and then in the next step it occurs in the ground state of ^{54}Ti. In Model 2, EC from ^{54}Cr takes place at a 0.309 MeV state in ^{54}Mn followed by a 2.46 MeV state in ^{54}Ti. As a result, Model 2 adds more heat to the crust.

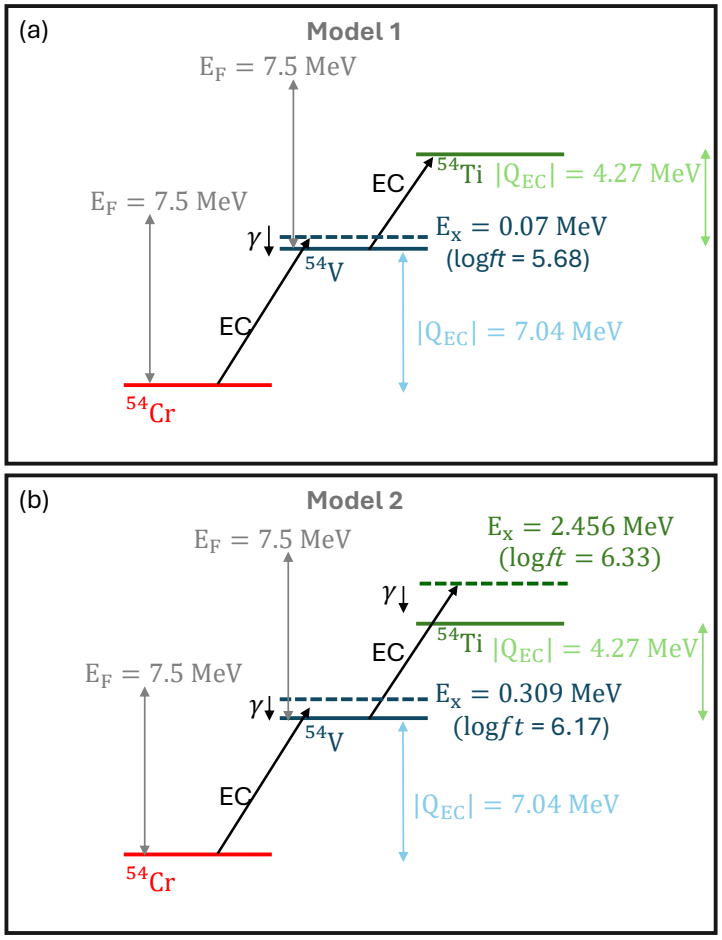

Figure 5.7 Energy level schemes shown for (a) Model 1 and (b) Model 2 showing the difference between heat deposited in the crust in Region 2.

In Region 2, we see cooling for Model 1 inputs indicating formation of Urca pairs. Fig. 5.6 shows the isotopic abundance and reaction flow for Model 2 at $t = 2 \times 10^9$ s.

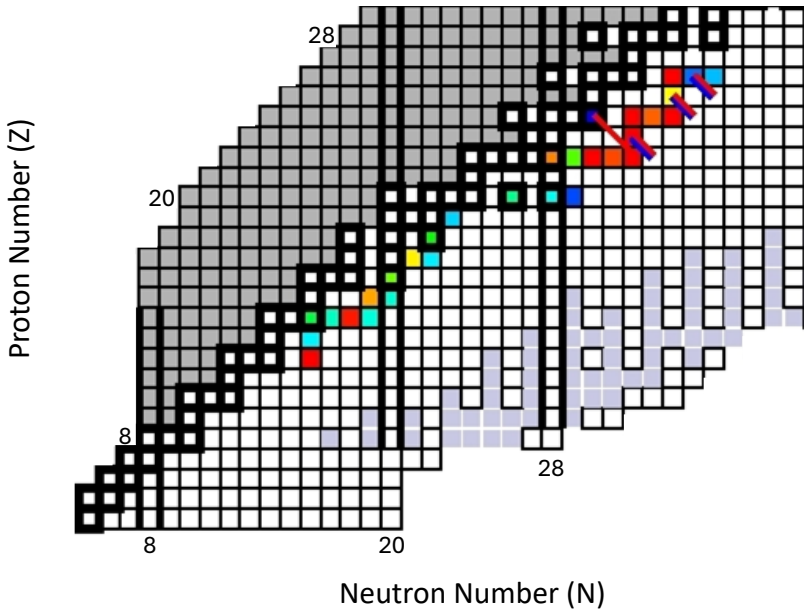

Figure 5.8 Isotopic abundances and reaction flows at $t = 2 \times 10^9$ s in Region 2, calculated using inputs from QRPA.

In Region 2, the strongest Urca pair is ^{55}V $\leftrightarrow$ ^{55}Ti for Model 1 (see Fig. 5.9). In this model, EC happens for the ground state of ^{55}Ti, and because the Fermi energy is nearly equal to the EC threshold, β^- decay can occur. In Models 2 and 3, the first allowed EC happens for an excited state at 1.017 MeV in ^{55}Ti, but the Fermi energy is too low for the transition to occur. Thus, an Urca pair forms in Model 1, but not in Models 2 and 3.

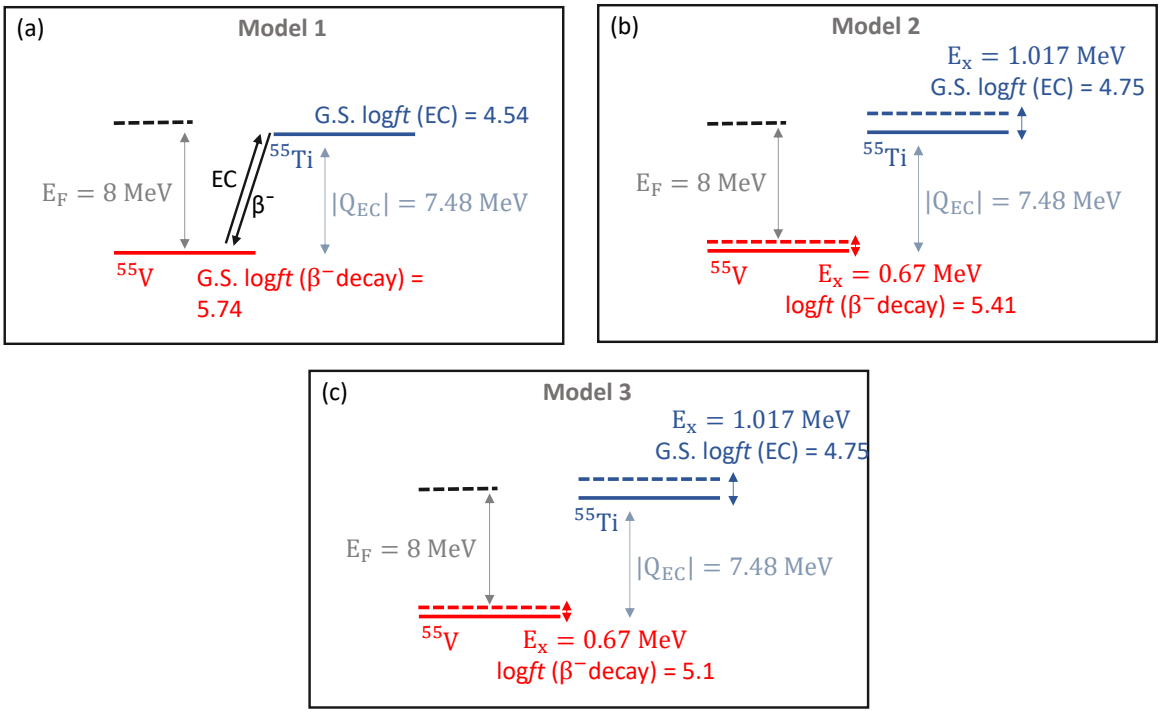

Figure 5.9 (a)Energy level scheme in Region 2 for Urca pair formed between ^{55}V and ^{55}Ti in Model 1. (b) and (c) No Urca pair is formed between ^{55}V and ^{55}Ti in Models 2 and 3, respectively.

Another important cooling contributor in this region is the Urca pair between ^{57}Cr and ^{57}V (see Fig. 5.10). In all models, EC happens from ground state to ground state. However, Model 1 has low $\log ft$ values for both EC and β^- decay, meaning its transition is the strongest. Model 2 has the highest $\log ft$ value for EC and the weakest cycle, while Model 3 provides slightly more cooling than Model 2. It is concluded that Model 1 provides less heating and more cooling than Models 2 and 3.

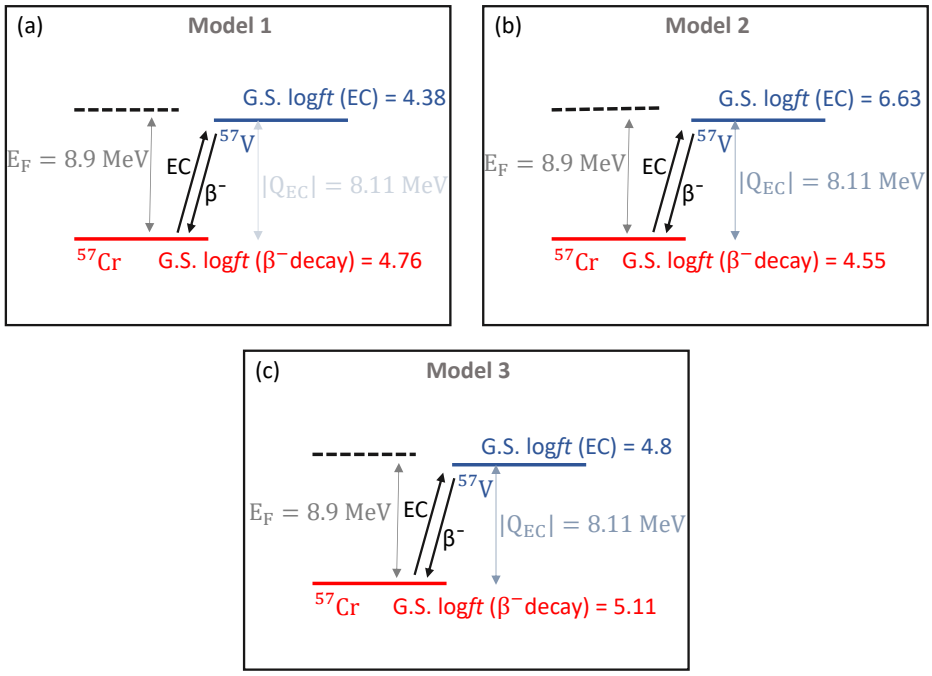

Figure 5.10 Energy level scheme shown for Urca pair formed between ^{57}Cr and ^{57}V in Region 2 in (a) Model 1, (b) Model 2, and (c) Model 3.

5.2.3 Region 3

Region 3 spans from $t = 2.9 \times 10^9$ s to $t = 3.8 \times 10^9$ s. No significant cooling occurs in this period, but heating differs among the models: Model 2 heats the most, Model 3 the least, and Model 1 is in between.

The main heating source here is the two-step EC reaction: ^{56}Cr $\rightarrow^{56}$ V $\rightarrow^{56}$ Ti. Fig. 5.11 displays the energy level schemes for these transitions. In Model 2, both steps involve excited states, with the ^{56}V $\rightarrow^{56}$ Ti step occurring at 1.21 MeV. This excited state releases a significant amount of heat when it de-excites to the ground state. In contrast, for Models 1 and 3, the second step happens from the ground state, so only the EC from ^{56}Cr to an excited state in ^{56}V contributes to heating. In Model 1, this transition is at 0.05 MeV, while in Model 3 it is at 0.01 MeV. Consequently, heating in Model 2 is higher than in Model 3.

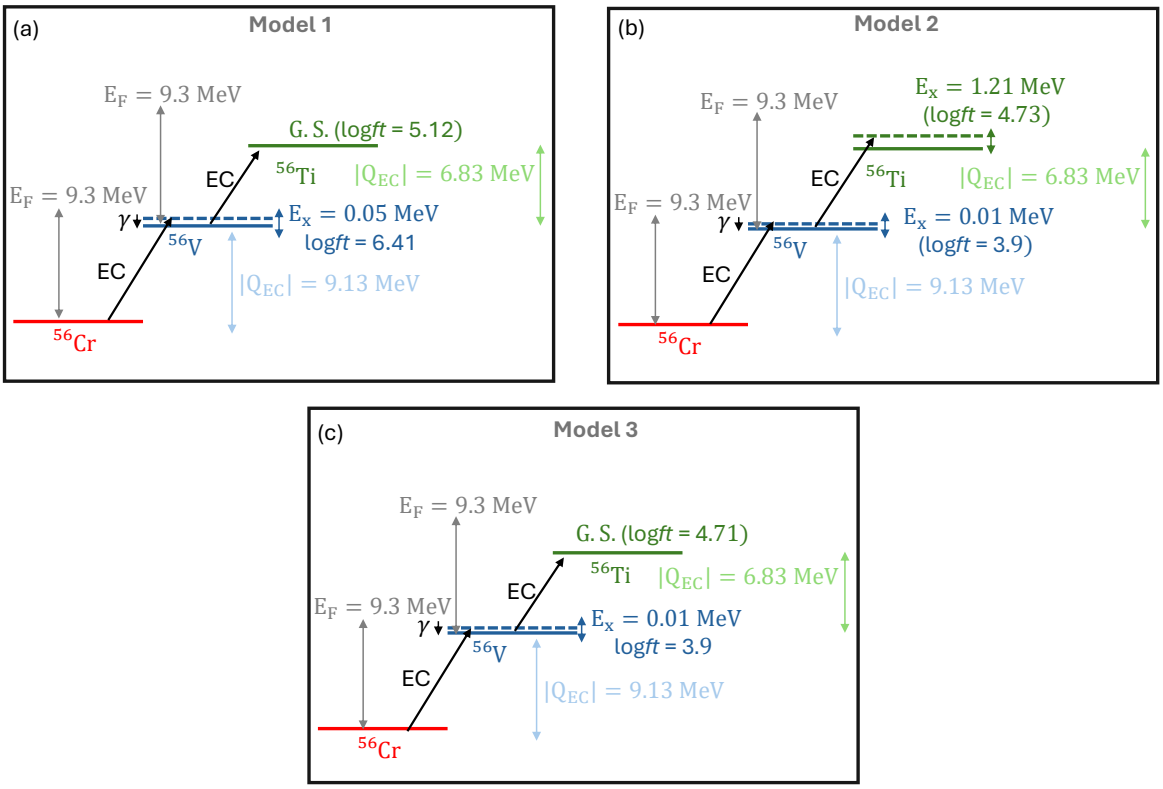

Figure 5.11 Level schemes shown for (a) Model 1, (b) Model 2, and (c) Model 3 for a two-step EC reaction from ^{54}Cr to ^{54}Ti in Region 3.

5.2.4 Region 4

Region 4 spans from $t = 5.3 \times 10^9$ s to $t = 6.6 \times 10^9$ s. In this period, all three models show the same patterns of heating and cooling as the inputs are identical. The heating mainly comes from a two-step EC reaction: ^{52}Ti $\rightarrow$ ^{52}Sc $\rightarrow$ ^{52}Ca. The cooling is provided by the two Urca pairs ^{59}Cr $\leftrightarrow$ ^{59}V and ^{57}V$\leftrightarrow$^{57}Ti. Fig. 5.12 displays the energy level scheme for the two-step EC reaction. In both steps, the transitions occur to excited states in the daughter nuclei, which then release heat as they de-excite to the ground state.

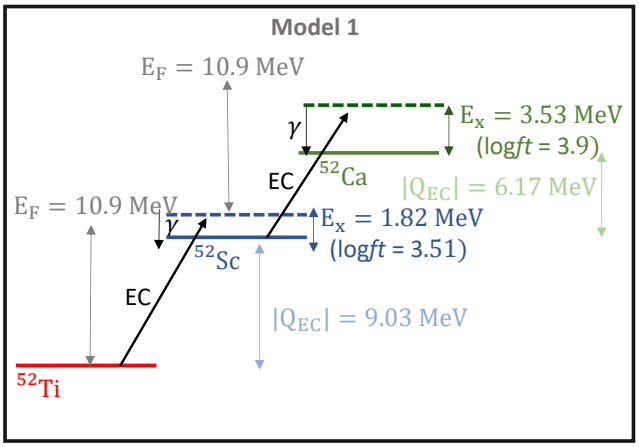

Figure 5.12 Energy level schemes shown for Model 1 for a two-step EC reaction from ^{52}Ti to ^{52}Ca in Region 4. The inputs were unchanged for Models 2 and 3, therefore, the level schemes for those Models are identical.

The energy level schemes for the two strong Urca pairs contributing to the cooling are shown in Fig. 5.13.

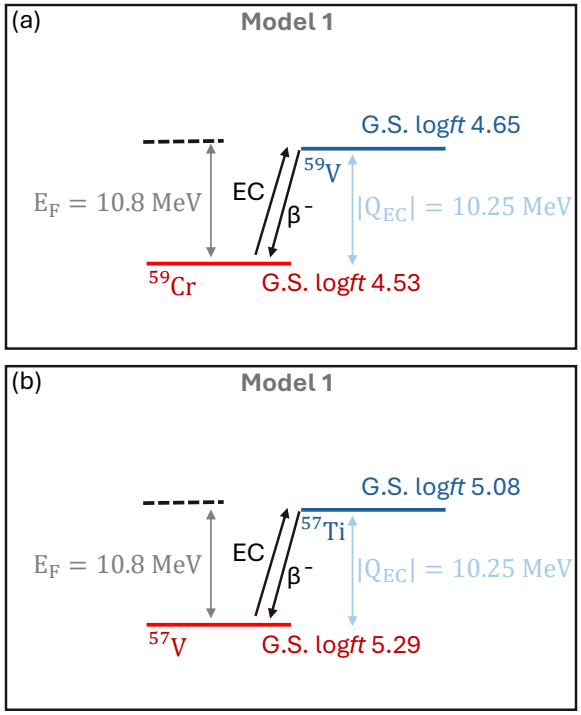

Figure 5.13 Energy level schemes shown for the Urca pairs in Region 4: (a) ^{59}Cr↔^{59}V and (b) ^{57}V↔^{57}Ti.

5.2.5 Region 5

Region 5 spans from $t = 9.34 \times 10^9$ s to $t = 1.17 \times 10^{10}$ s. Heating in this region is dominated by the two-step EC reaction: ^{55}Ti → ^{55}Sc → ^{55}Ca, shown by Fig. 5.14. The inputs in Models 2 and 3 were kept unchanged from Model 1; therefore, identical heating is observed across models.

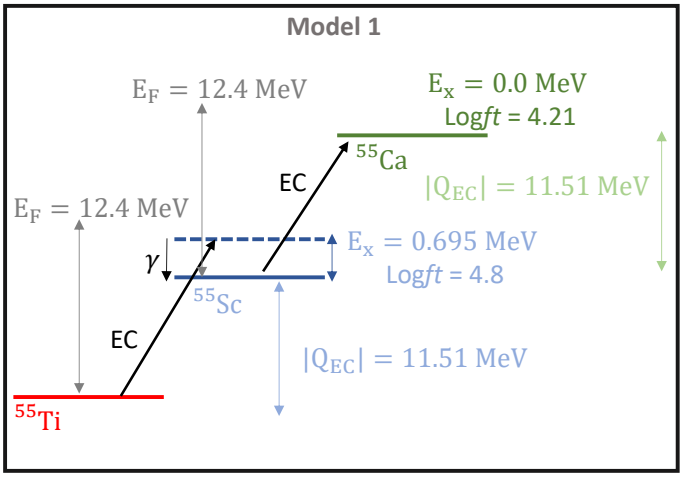

Figure 5.14 Energy level scheme for Model 1 for a two-step EC reaction from ^{55}Ti to ^{55}Ca in Region 5.

Cooling in Models 2 and 3 in this region is mainly driven by the strongest Urca pair: ^{33}Al ↔ ^{33}Si. Fig. 5.15 show the energy level schemes of these transitions to illustrate the difference between the formation of Urca pairs between the models. In Model 1, the first allowed EC transition occurs at an excited state of 0.37 MeV, while in Models 2 and 3 it takes place at the ground state. Because the Fermi energy is not high enough for EC to occur at the excited state in Model 1, no Urca pair forms. In contrast, in Models 2 and 3, EC is allowed, and the low logft values of the transitions lead to a strong Urca pair. It is concluded that this is an Urca pair that should be in the simulations, using the experimental data available.

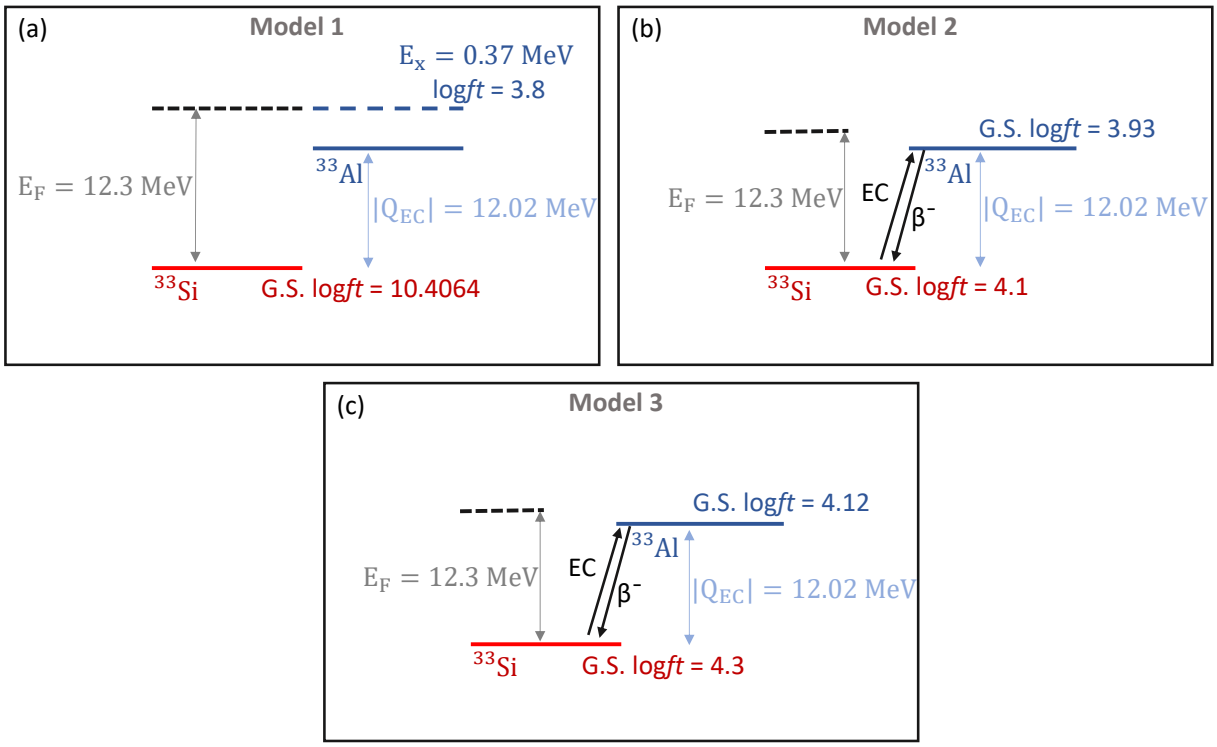

Figure 5.15 Energy level schemes for (a) Model 1, (b) Model 2, and (c) Model 3 for the Urca pair ^{33}Si↔^{33}Mg in Region 5.

5.2.6 Region 6

In Region 6, spanning from $t = 1.2 \times 10^{10}$ s to $t = 1.5 \times 10^{10}$ s, cooling is observed for all three models. The ^{29}Na ↔ ^{29}Mg pair is identified as the strongest transition for all input versions, though with different predicted strengths. Model 1 predicts the highest strength, resulting in the largest dip in Region 6. In contrast, Model 2 predicts approximately half the strength compared to Model 1, while Model 3 reduces the predicted strength by an order of magnitude. Energy level schemes of the Urca pair ^{29}Mg↔^{29}Na are shown in Fig. 5.16. It is concluded that the ^{29}Mg↔^{29}Na Urca pair exists, but is weaker than originally assumed.

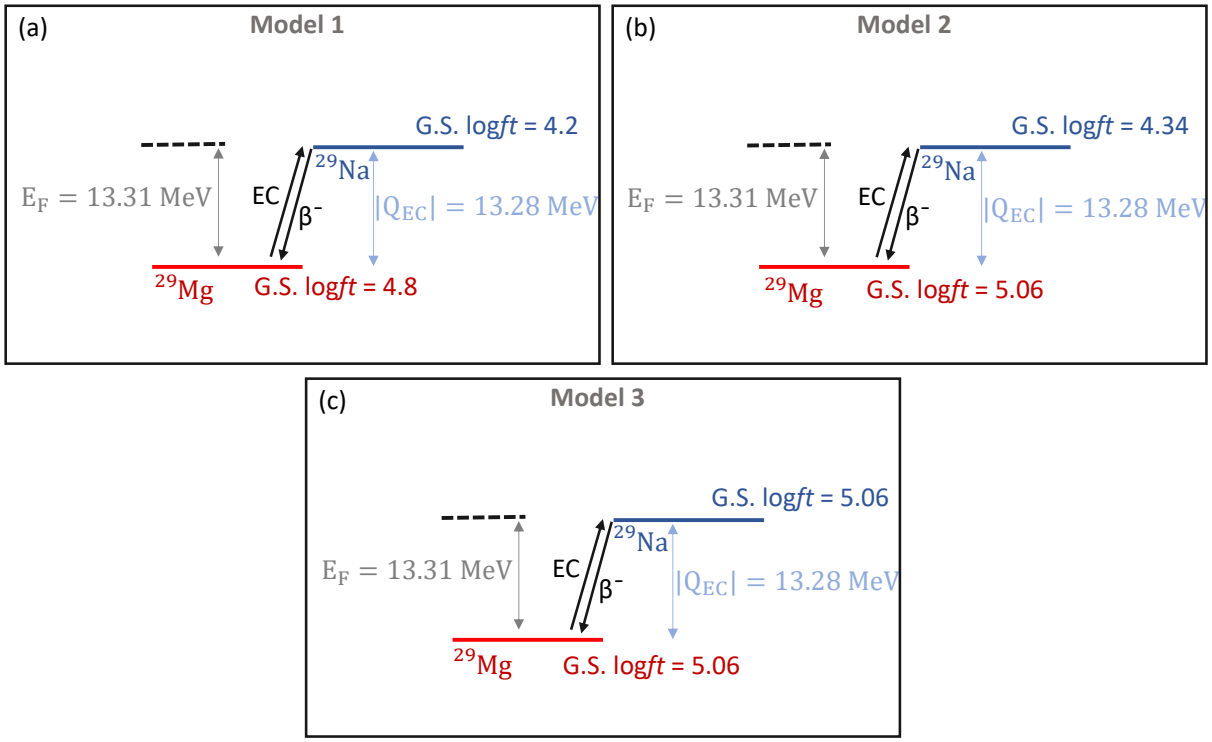

Figure 5.16 Energy level schemes for (a) Model 1, (b) Model 2, and (c) Model 3 for the Urca pair ^{29}Mg↔^{29}Na in Region 6.

5.3 Urca Pairs

The Urca pairs are crucial for cooling in the neutron star crust, and accurate inputs are necessary in the simulation to identify the strongest pairs responsible for cooling. Table 5.2 lists the strongest Urca pairs integrated over the entire time range for all three models. The strengths of these Urca pairs, calculated using time-integrated reaction flow, are scaled by the strength of the strongest Urca pair across all models, ^{29}Na ↔ ^{29}Mg, from Model 1. Urca pairs with scaled strengths lower than 10^{-4} are not included in the table, as they contribute minimally to the overall cooling. By focusing on the pairs with stronger contributions, we can better understand which reactions are most important for cooling the neutron star crust.

The ^{29}Na ↔ ^{29}Mg pair is identified as the strongest Urca pair in Models 1 and 2, while ^{33}Al ↔ ^{33}Si is the strongest Urca pair for Model 3 results. The strength for the ^{29}Na ↔ ^{29}Mg pair is highest for Model 1. In Models 2 and 3, the strength is reduced. The ^{33}Al ↔ ^{33}Si pair is the

Table 5.2 Comparison of Urca pair strengths for Models 1, 2, and 3 (scaled by the strength of ^{29}Na $\leftrightarrow$ ^{29}Mg pair from Model 1).

Urca Pairs	**Model 1**	**Model 2**	**Model 3**
^{29}Na $\leftrightarrow$ ^{29}Mg	1.0	0.433	0.112
^{33}Al $\leftrightarrow$ ^{33}Si	-	0.227	0.145
^{55}Ti $\leftrightarrow$ ^{55}V	0.129	-	-
^{57}Ti $\leftrightarrow$ ^{57}V	0.09	0.09	0.09
^{59}V $\leftrightarrow$ ^{59}Cr	0.044	0.045	0.045
^{61}V $\leftrightarrow$ ^{61}Cr	0.041	0.011	0.011
^{55}V $\leftrightarrow$ ^{55}Cr	0.032	-	-
^{57}V $\leftrightarrow$ ^{57}Cr	0.092	0.017	0.026
^{57}Sc $\leftrightarrow$ ^{57}Ti	0.026	0.022	0.022
^{59}Ti $\leftrightarrow$ ^{59}V	0.013	0.013	0.013
^{59}Cr $\leftrightarrow$ ^{59}Mn	0.013	-	-
^{57}Cr $\leftrightarrow$ ^{57}Mn	-	0.001	0.001
^{59}Mn $\leftrightarrow$ ^{59}Fe	-	0.001	0.0003

second strongest for Model. However, Model 1 does not identify this as a strong pair. Both of the above mentioned pairs involve isotopes near the $N = 20$ "island of inversion", and the experimental results described in this thesis will be helpful for constraining the weak interaction rates.

In contrast, the ^{55}Ti $\leftrightarrow$ ^{55}V pair is identified as one of the strongest by Model 1, but neither Model 2 or 3 support this finding. For the ^{57}Ti $\leftrightarrow$ ^{57}V pair, Model 1 inputs were kept unchanged across the three versions, so all predict identical strengths. The ^{59}V $\leftrightarrow$ ^{59}Cr pair is consistently identified as the fourth strongest across all versions, with minimal variation in strength.

For pairs like ^{61}V $\leftrightarrow$ ^{61}Cr, ^{57}Sc $\leftrightarrow$ ^{57}Ti, and ^{57}Cr $\leftrightarrow$ ^{57}Mn, no experimental data was available. As a result, Model 2 inputs were kept unchanged for Model 3, leading to identical strength predictions across the versions. Models 2 and 3 do not identify the ^{55}V $\leftrightarrow$ ^{55}Cr pair as strong, while Model 1 inputs fail to recognize ^{57}Cr $\leftrightarrow$ ^{57}Mn and ^{59}Mn $\leftrightarrow$ ^{59}Fe as strong pairs.

Finally, for the ^{57}V $\leftrightarrow$ ^{57}Cr pair, the three input versions predict varying strengths. Overall, the strengths based on experimental data align more closely with the shell-model than with QRPA predictions. Referring back to Fig. 5.3, it is observed that when the best estimates available for heating and cooling are used, the magnitudes of heating and cooling tend to become smaller. Whether this trend is true in other relevant regions in the chart of nuclei, requires further investigation.

CHAPTER 6

CONCLUSION AND OUTLOOK

Weak reactions such as electron capture and β^- decay contribute to heating and cooling in neutron stars. Accurate weak interaction rates are important for realistic neutron star simulations. However, the reaction networks used in simulations involve over 3,000 isotopes, making it impractical to obtain experimental weak interaction rates for all nuclei. As a result, theoretical calculations must be used, and experimental data are necessary to validate and benchmark these models.

Currently, several studies of neutron stars rely on mean-approximation calculations for weak reaction rates, which have been shown to be not as reliable for predicting transitions to specific low-lying states, which are most important for accurate simulations on neutron star crust. In contrast, the shell model is known to perform better for light and medium mass (A$<$ 65) nuclei. Gamow-Teller (GT) strengths are crucial for determining electron-capture rates, but direct weak-interaction studies are, if available, limited to ground state to ground state transitions for neutron-rich nuclei due to Q-value constraints. Charge-exchange reactions, governed by the strong interaction, overcome this limitation as they connect the same initial and final states as electron capture and β^- decay and allow for the extraction of GT strengths. These features make them an effective tool for studying weak-interaction rates indirectly.

Many astrophysically relevant nuclei are unstable, preventing their study in forward kinematics since a target for experimental studies cannot be created. Instead, the charge-exchange reactions must be performed in inverse kinematics, using unstable nuclei as beams to ensure they do not decay in-flight. The (d,^{2}He) reaction in inverse kinematics is particularly well-suited for this purpose due to its spin-selective nature. This approach was applied in two experiments at the National Superconducting Cyclotron Laboratory (NSCL) and the Facility for Rare Isotope Beams (FRIB) using the Active-Target Time Projection Chamber (AT-TPC) and the S800 magnetic spectrometer. The use of the active target and the ability to cleanly select (d,^{2}He) events because of the vertex reconstruction following the emission of two protons from ^{2}He are critical advantages of the method. It is, at present, the only way to obtain GT strength in the EC/β^+ direction for neutron-rich unstable

nuclei.

In this work, two reaction channels were studied: ^{33}Al(d,^{2}He) and ^{32}Mg(d,^{2}He). ^{32}Mg and ^{33}Al are near the $N = 20$ island of inversion, an area important for understanding neutron star heating, cooling, and nuclear structure. GT strengths were extracted for a state near 0 MeV in the ^{33}Al$\rightarrow$^{33}Mg transition and for states between 1–2 MeV and 3–4 MeV in the ^{32}Mg$\rightarrow$^{32}Na transition.

The presence of a GT transition shows that the ground state of ^{33}Al has significant pf shell contribution in its wavefunction. Although statistical uncertainties are large, we find reasonable correspondence between shell-model calculations using the $sdpf - m$ interaction, which included contributions from $sd-$ and $pf-$ shell configuration. For the ^{33}Al(d,^{2}He) reaction, we observed a GT transition at low excitation energies that the shell model predicts, for a state near 1.3 MeV. For the ^{32}Mg(d,^{2}He) reaction, the GT strength between 1–2 MeV agrees well with the shell model, and strength at higher exctiation energy is found, albeit in what appears to be a transition to single final state, where as in the shell-model calculations, the strength is distributed. Due to low statistics in the experiment, the uncertainties are high and it was difficult to draw strong conclusion about the strengths at high-excitation energies.

In addition to the experimental work, weak interaction rates and their role in the neutron star crusts were studied for nuclei in the sd and pf shells, for which accurate shell-model calculations are already available. Neutron star crust simulations were performed using three sets of weak interaction rates: (1) exclusively from QRPA calculations, (2) shell-model calculations for sd and pf shell nuclei combined with QRPA calculations for all others, and (3) experimental data for sd and pf shells when available combined with shell-model calculations, otherwise, QRPA calculations were used. The evolution of heat energy in the crust was studied for each set and reactions that contributed to heating and cooling at different depths were identified. The rates based on QRPA calculations tend to overestimate both heating and cooling compared to the models that use the shell-model calculations and experimental data. Moreover, the deviations between rates based on experimental data and the shell-model calculation are small. It is concluded that the approach of using shell-model calculations in combination with experimental data, where available, is a good

approach.

To improve neutron star crust simulation results, it will be important to extend shell-model calculations to include weak interaction rates for nuclei beyond the sd and pf shells, including those in the $N = 20$ island of inversion. The experimental work described in this thesis provides valuable benchmarks for these improvements. In addition, further experiments using the $(d,^2\mathrm{He})$ probe in inverse kinematics should be considered for important transitions such as ^{29}Mg $\leftrightarrow^{29}$ Na, ^{61}V $\leftrightarrow^{61}$ Cr, ^{57}Sc $\leftrightarrow^{57}$ Ti, and ^{57}Cr $\leftrightarrow^{57}$ Mn. The further increases in beam intensities at FRIB will be critical for such measurements. In addition, for the AT-TPC to handle higher beam intensities, it should be considered to operate in a solenoidal field, which would strongly reduce the background due to δ electrons. Additionally, it would improve the angular and energy resolution of the measured proton tracks and allow for the stopping of higher-energy protons, reducing event loss from tracks exiting the AT-TPC chamber.

BIBLIOGRAPHY

[1] J. M. Lattimer and M. Prakash. The Physics of Neutron Stars. *Science*, 304(5670):536–542, 2004.

[2] S. L. Shapiro and S. A. Teukolsky. *Black Holes, White Dwarfs and Neutron Stars: The Physics of Compact Objects*. Wiley, New York, 1983.

[3] W. Baade and F. Zwicky. Cosmic Rays from Super-Novae. *Proceedings of the National Academy of Sciences*, 20(5):259–263, 1934.

[4] A. Burrows and D. Vartanyan. Core-collapse supernova explosion theory. *Nature*, 589(7840):29–39, 2021.

[5] T. M. Tauris and H. Janka. J0453+1559: A Neutron Star–White Dwarf Binary from a Thermonuclear Electron-capture Supernova? *Astrophys. J. Lett.*, 886(1):L20, 2019.

[6] R. W. Romani, D. Kandel, A. V. Filippenko, T. G. Brink, and W. Zheng. PSR J09520607: The Fastest and Heaviest Known Galactic Neutron Star. *Astrophys. J. Lett.*, 934(2):L17, 2022.

[7] K. Y. Lau. *Nuclear Reactions in the Crust of Accreting Neutron Stars*. PhD thesis, Michigan State University, 2012.

[8] Z. Meisel, A. Deibel, L. Keek, P. Shternin, and J. Elfritz. Nuclear physics of the outer layers of accreting neutron stars. *J. Phys. G: Nucl. Part. Phys.*, 45(9):093001, 2018.

[9] T. J.-L. Courvoisier. *Neutron Stars*. Springer Berlin Heidelberg, Berlin, Heidelberg, 2013.

[10] S. Mereghetti, L. Stella, and M. Tavani. The neutron stars of Soft X-ray Transients. *Astron. Astrophys. Rev.*, 8(4):279–316, 1998.

[11] E. F. Brown. Superburst ignition and implications for neutron star interiors. *Astrophys. J.*, 614(1):L57, 2004.

[12] H. Schatz, S. Gupta, P. Möller, M. Beard, E. F. Brown, A. T. Deibel, L. R. Gasques, W. R. Hix, L. Keek, R. Lau, A. W. Steiner, and M. Wiescher. Strong neutrino cooling by cycles of electron capture and β^- decay in neutron star crusts. *Nature*, 505(7481):62–65, 2014.

[13] Z. Meisel, S. George, S. Ahn, D. Bazin, B. A. Brown, J. Browne, J. F. Carpino, H. Chung, A. L. Cole, R. H. Cyburt, A. Estradé, M. Famiano, A. Gade, C. Langer, M. Matoš, W. Mittig, F. Montes, D. J. Morrissey, J. Pereira, H. Schatz, J. Schatz, M. Scott, D. Shapira, K. Smith, J. Stevens, W. Tan, O. Tarasov, S. Towers, K. Wimmer, J. R. Winkelbauer, J. Yurkon, and R. G. T. Zegers. Mass Measurement of ^{56}Sc Reveals a Small $A = 56$ Odd-Even Mass Staggering, Implying a Cooler Accreted Neutron Star Crust. *Phys. Rev. Lett.*, 115:162501, 2015.

[14] G. Gamow and M. Schoenberg. Neutrino Theory of Stellar Collapse. *Phys. Rev.*, 59:539–547, 1941.

[15] P. Möller and J. Randrup. New developments in the calculation of -strength functions. *Nucl. Phys. A*, 514(1):1–48, 1990.

[16] A. L. Cole, T. S. Anderson, R. G. T. Zegers, S. M. Austin, B. A. Brown, L. Valdez, S. Gupta, G. W. Hitt, and O. Fawwaz. Gamow-Teller strengths and electron-capture rates for pf-shell nuclei of relevance for late stellar evolution. *Phys. Rev. C*, 86:015809, 2012.

[17] M. G. Mayer. On Closed Shells in Nuclei. II. *Phys. Rev.*, 75:1969–1970, 1949.

[18] O. Haxel, J. H. D. Jensen, and H. E. Suess. On the "Magic Numbers" in Nuclear Structure. *Phys. Rev.*, 75:1766–1766, 1949.

[19] A. Ridha. *Chapter Two (Binding Energy Nuclear Models)*. 2016.

[20] C. Thibault, R. Klapisch, C. Rigaud, A. M. Poskanzer, R. Prieels, L. Lessard, and W. Reisdorf. Direct measurement of the masses of ^{11}Li and $^{26-32}$Na with an on-line mass spectrometer. *Phys. Rev. C*, 12:644–657, 1975.

[21] X. Campi, H. Flocard, A. K. Kerman, and S. Koonin. Shape transition in the neutron rich sodium isotopes. *Nucl. Phys. A*, 251(2):193–205, 1975.

[22] B. H. Wildenthal and W. Chung. Collapse of the conventional shell-model ordering in the very-neutron-rich isotopes of Na and Mg. *Phys. Rev. C*, 22:2260–2262, 1980.

[23] A. Watt, R. P. Singhal, M. H. Storm, and R. R. Whitehead. A shell-model investigation of the binding energies of some exotic isotopes of sodium and magnesium. *J. Phys. G: Nucl. Phys.*, 7(7):L145, 1981.

[24] E. K. Warburton, J. A. Becker, and B. A. Brown. Mass systematics for A=29–44 nuclei: The deformed A∼32 region. *Phys. Rev. C*, 41:1147–1166, 1990.

[25] F. Sarazin, H. Savajols, W. Mittig, F. Nowacki, N. A. Orr, Z. Ren, P. Roussel-Chomaz, G. Auger, D. Baiborodin, A. V. Belozyorov, C. Borcea, E. Caurier, Z. Dlouhý, A. Gillibert, A. S. Lalleman, M. Lewitowicz, S. M. Lukyanov, F. de Oliveira, Y. E. Penionzhkevich, D. Ridikas, H. Sakuraï, O. Tarasov, and A. de Vismes. Shape Coexistence and the $N = 28$ Shell Closure Far from Stability. *Phys. Rev. Lett.*, 84:5062–5065, 2000.

[26] T. Otsuka, R. Fujimoto, Y. Utsuno, B. A. Brown, M. Honma, and T. Mizusaki. Magic Numbers in Exotic Nuclei and Spin-Isospin Properties of the *NN* Interaction. *Phys. Rev. Lett.*, 87:082502, 2001.

[27] T. Otsuka, A. Gade, O. Sorlin, T. Suzuki, and Y. Utsuno. Evolution of shell structure in exotic nuclei. *Rev. Mod. Phys.*, 92:015002, 2020.

[28] T. Glasmacher. COULOMB EXCITATION AT INTERMEDIATE ENERGIES. *Annu. Rev. Nucl. Part. Sci.*, 48(1):1–31, 1998.

[29] Y. Yanagisawa, M. Notani, H. Sakurai, M. Kunibu, H. Akiyoshi, N. Aoi, H. Baba, K. Demichi, N. Fukuda, H. Hasegawa, Y. Higurashi, M. Ishihara, N. Iwasa, H. Iwasaki, T. Gomi, S. Kanno, M. Kurokawa, Y. U. Matsuyama, S. Michimasa, T. Minemura, T. Mizoi, T. Nakamura, A. Saito, M. Serata, S. Shimoura, T. Sugimoto, E. Takeshita, S. Takeuchi, K. Ue, K. Yamada, K. Yoneda, and T. Motobayashi. The first excited state of ^{30}Ne studied by proton inelastic scattering in reversed kinematics. *Nucl. Phys. A*, 734:374–377, 2004.

[30] T. Nakamura, N. Fukuda, N. Aoi, N. Imai, M. Ishihara, H. Iwasaki, T. Kobayashi, T. Kubo, A. Mengoni, T. Motobayashi, M. Notani, H. Otsu, H. Sakurai, S. Shimoura, T. Teranishi, Y. X. Watanabe, and K. Yoneda. Neutron capture cross section of ^{14}C of astrophysical interest studied by Coulomb breakup of ^{15}C. *Phys. Rev. C*, 79:035805, 2009.

[31] B. V. Pritychenko, T. Glasmacher, B. A. Brown, P. D. Cottle, R. W. Ibbotson, K. W. Kemper, and H. Scheit. Shape coexistence on the boundary of the "island of inversion": Exotic beam spectroscopy of ^{34}Al. *Phys. Rev. C*, 63:047308, 2001.

[32] B. V. Pritychenko, T. Glasmacher, P. D. Cottle, R. W. Ibbotson, K. W. Kemper, L. A. Riley, A. Sakharuk, H. Scheit, M. Steiner, and V. Zelevinsky. Structure of the "island of inversion" nucleus ^{33}Mg. *Phys. Rev. C*, 65:061304, 2002.

[33] B. V. Pritychenko, T. Glasmacher, B. A. Brown, P. D. Cottle, R. W. Ibbotson, K. W. Kemper, L. A. Riley, and H. Scheit. First observation of an excited state in the neutron-rich nucleus ^{31}Na. *Phys. Rev. C*, 63:011305, 2000.

[34] K. Yoneda, H. Sakurai, T. Gomi, T. Motobayashi, N. Aoi, N. Fukuda, U. Futakami, Z. Gácsi, Y. Higurashi, N. Imai, N. Iwasa, H. Iwasaki, T. Kubo, M. Kunibu, M. Kurokawa, Z. A. Liu, T. Minemura, A. Saito, M. Serata, S. Shimoura, S. Takeuchi, Y. X. Watanabe, K. N. Yamada, Y. Yanagisawa, K. Yogo, A. Yoshida, and M. Ishihara. Deformation of ^{3}4Mg studied via in-beam γ-ray spectroscopy using radioactive-ion projectile fragmentation. *Phys. Lett. B*, 499:233–237, 2001.

[35] J. A. Church, C. M. Campbell, D.-C. Dinca, J. Enders, A. Gade, T. Glasmacher, Z. Hu, R. V. F. Janssens, W. F. Mueller, H. Olliver, B. C. Perry, L. A. Riley, and K. L. Yurkewicz. Measurement of $E2$ transition strengths in ^{32,34}Mg. *Phys. Rev. C*, 72:054320, 2005.

[36] V. Tripathi, S. L. Tabor, P. F. Mantica, Y. Utsuno, P. Bender, J. Cook, C. R. Hoffman, S. Lee, T. Otsuka, J. Pereira, M. Perry, K. Pepper, J. S. Pinter, J. Stoker, A. Volya, and D. Weisshaar. Intruder Configurations in the $A = 33$ Isobars: ^{33}Mg and ^{33}Al. *Phys. Rev. Lett.*, 101:142504, 2008.

[37] E. K. Warburton, J. A. Becker, and B. A. Brown. Mass systematics for A=29–44 nuclei: The deformed A∼32 region. *Phys. Rev. C*, 41:1147–1166, 1990.

[38] J. Chen and B. Singh. Nuclear Data Sheets for A = 33. *Nucl. Data Sheets*, 199:1, 2025.

[39] D. Guillemaud-Mueller, C. Detraz, M. Langevin, F. Naulin, M. de Saint-Simon, C. Thibault, F. Touchard, and M. Epherre. β-Decay schemes of very neutron-rich sodium isotopes and their descendants. *Nucl. Phys. A*, 426(1):37–76, 1984.

[40] S. Nummela, F. Nowacki, P. Baumann, E. Caurier, J. Cederkäll, S. Courtin, P. Dessagne, A. Jokinen, A. Knipper, G. Le Scornet, L. G. Lyapin, Ch. Miehé, M. Oinonen, E. Poirier, Z. Radivojevic, M. Ramdhane, W. H. Trzaska, G. Walter, J. Äystö, and ISOLDE Collaboration. Intruder features in the island of inversion: The case of ^{33}Mg. *Phys. Rev. C*, 64:054313, 2001.

[41] D. T. Yordanov, M. Kowalska, K. Blaum, M. De Rydt, K. T. Flanagan, P. Lievens, R. Neugart, G. Neyens, and H. H. Stroke. Spin and Magnetic Moment of ^{33}Mg: Evidence for a Negative-Parity Intruder Ground State. *Phys. Rev. Lett.*, 99:212501, 2007.

[42] D. T. Yordanov for the COLLAPS Collaboration. Laser spectroscopy in the island of inversion. *Hyperfine Interactions*, 196(1):53–60, 2010.

[43] D. Bazin, N. Aoi, H. Baba, J. Chen, H. Crawford, P. Doornenbal, P. Fallon, K. Li, J. Lee, M. Matsushita, T. Motobayashi, H. Sakurai, H. Scheit, D. Steppenbeck, R. Stroberg, S. Takeuchi, H. Wang, K. Yoneda, and C. X. Yuan. Spectroscopy of ^{33}Mg with knock-out reactions. *Phys. Rev. C*, 103:064318, 2021.

[44] A. L. Richard, H. L. Crawford, P. Fallon, A. O. Macchiavelli, V. M. Bader, D. Bazin, M. Bowry, C. M. Campbell, M. P. Carpenter, R. M. Clark, M. Cromaz, A. Gade, E. Ideguchi, H. Iwasaki, M. D. Jones, C. Langer, I. Y. Lee, C. Loelius, E. Lunderberg, C. Morse, J. Rissanen, M. Salathe, D. Smalley, S. R. Stroberg, D. Weisshaar, K. Whitmore, A. Wiens, S. J. Williams, K. Wimmer, and T. Yamamato. Strongly coupled rotational band in ^{33}Mg. *Phys. Rev. C*, 96:011303, 2017.

[45] G. Neyens. Multiparticle-multihole states in ^{31}Mg and ^{33}Mg: A critical evaluation. *Phys. Rev. C*, 84:064310, 2011.

[46] C. Ouellet and B. Singh. Nuclear Data Sheets for A = 32. *Nucl. Data Sheets*, 112:2199, 2011.

[47] G. M. Fuller, W. A. Fowler, and M. J. Newman. Stellar weak-interaction rates for sd-shell nuclei. I - Nuclear matrix element systematics with application to Al-26 and selected nuclei of importance to the supernova problem. *Astrophys. J.*, 42:447–473, 1980.

[48] G. M. Fuller, W. A. Fowler, and M. J. Newman. Stellar weak interaction rates for intermediate mass nuclei. III - Rate tables for the free nucleons and nuclei with A = 21 to A = 60. *Astrophys. J.*, 48:279–319, 1982.

[49] H. Th. Janka, K. Langanke, A. Marek, G. Martínez-Pinedo, and B. Müller. Theory of core-collapse supernovae. *Phys. Rep.*, 442(1-6):38–74, 2007.

[50] C. L. Doherty, G.-P. Pilar, L. Siess, and J. C. Lattanzio. Super-AGB Stars and their role as electron capture supernova progenitors. *Publ. Astron. Soc. Aust*, 34, 2017.

[51] K. Nomoto and S. Leung. *Electron Capture Supernovae from Super Asymptotic Giant Branch Stars*. Springer International Publishing, Cham, 2017.

[52] K. Iwamoto, F. Brachwitz, K. Nomoto, N. Kishimoto, H. Umeda, W. R. Hix, and F.-K. Thielemann. Nucleosynthesis in Chandrasekhar Mass Models for Type Ia Supernovae and Constraints on Progenitor Systems and Burning-Front Propagation. 2000.

[53] L. Men-Quan, Z. Jie, and L. Zhi-Quan. Nuclear statistical equilibrium at core-collapse supernova. *Chin. Phys.*, 16(10):3146, 2007.

[54] J. Cooperstein and J. Wambach. Electron capture in stellar collapse. *Nucl. Phys. A*, 420(3):591–620, 1984.

[55] K. Langanke and G. Martínez-Pinedo. Shell-model calculations of stellar weak interaction rates: II. Weak rates for nuclei in the mass range A = 45 65 in supernovae environment. *Nucl. Phys. A*, 673:481–508, 2000.

[56] G. Perdikakis, R. G. T. Zegers, Sam M. Austin, D. Bazin, C. Caesar, J. M. Deaven, A. Gade, D. Galaviz, G. F. Grinyer, C. J. Guess, C. Herlitzius, G. W. Hitt, M. E. Howard, R. Meharchand, S. Noji, H. Sakai, Y. Shimbara, E. E. Smith, and C. Tur. Gamow-Teller unit cross sections for (t,^{3}He) and (^{3}He, t) reactions. *Phys. Rev. C*, 83:054614, 2011.

[57] F. Osterfeld. Nuclear spin and isospin excitations. *Rev. Mod. Phys.*, 64:491–557, 1992.

[58] T. N. Taddeucci, C. A. Goulding, T. A. Carey, Robert C. B., C. D. Goodman, C. C. Gaarde, J. S. Larsen, D. J. Horen, J. R. Rapaport, and E. Sugarbaker. The (p, n) reaction as a probe of beta decay strength. *Nucl. Phys*, 469:125–172, 1987.

[59] H. Lenske, H. H. Wolter, and H. G. Bohlen. Reaction mechanism of heavy-ion charge-exchange scattering at intermediate energies. *Phys. Rev. Lett.*, 62:1457–1460, 1989.

[60] W. G. Love and M. A. Franey. Effective nucleon-nucleon interaction for scattering at intermediate energies. *Phys. Rev. C*, 24:1073–1094, 1981.

[61] R. G. T. Zegers, T. Adachi, H. Akimune, S. M. Austin, A. M. van den Berg, B. A. Brown, Y. Fujita, M. F., S. Gales, C. Guess, M. Harakeh, H. Hashimoto, K. Hatanaka, R. Hayami, G. W. Hitt, M. E. Howard, M. Itoh, T. Kawabata, K. Kawase, M. Kinoshita, M. Matsubara, K. Nakanishi, S. Nakayama, S. Okumura, T. Ohta, Y. Sakemi, Y. Shimbara, Y. Shimizu, C. Scholl, C. Simenel, Y. Tameshige, A. Tamii, M. Uchida, T. Yamagata, and M. Yosoi. Extraction of weak transition strengths via the (^{3}He, t) reaction at 420 MeV. *Phys. Rev. Lett.*, 99 20:202501, 2007.

[62] K. Ikeda, S. Fujii, and J. I. Fujita. The (p,n) reactions and beta decays. *Physics Letters*, 3(6):271–272, 1963.

[63] G. F. Bertsch and H. Esbensen. The (p,n) reaction and the nucleon-nucleon force. *Rep. Prog. Phys.*, 50(6):607, 1987.

[64] A. Arima. History of giant resonances and quenching. *Nucl. Phys. A*, 649(1):260–270, 1999. Giant Resonances.

[65] B. H. Wildenthal, M. S. Curtin, and B. A. Brown. Predicted features of the beta decay of neutron-rich sd-shell nuclei. *Phys. Rev. C*, 28:1343–1366, 1983.

[66] B. A. Brown and B. H. Wildenthal. Experimental and theoretical Gamow-Teller beta-decay observables for the *sd*-shell nuclei. *At. Data Nucl. Data Tables*, 33(3):347–404, 1985.

[67] G. Martínez-Pinedo, A. Poves, E. Caurier, and A. P. Zuker. Effective g_A in the pf shell. *Phys. Rev. C*, 53:R2602–R2605, 1996.

[68] R. G. T. Zegers, R. Meharchand, Y. Shimbara, Sam M. Austin, D. Bazin, B. A. Brown, C. Aa. Diget, A. Gade, C. J. Guess, M. Hausmann, G. W. Hitt, M. E. Howard, M. King, D. Miller, S. Noji, A. Signoracci, K. Starosta, C. Tur, C. Vaman, P. Voss, D. Weisshaar, and J. Yurkon. ^{34}P(^{7}Li,^{7} Be$+\gamma$) Reaction at 100A MeV in Inverse Kinematics. *Phys. Rev. Lett.*, 104:212504, 2010.

[69] S. Giraud, J. C. Zamora, R. G. T. Zegers, D. Bazin, Y. Ayyad, S. Bacca, S. Beceiro-Novo, B. A. Brown, A. Carls, J. Chen, M. Cortesi, M. DeNudt, G. Hagen, C. Hultquist, C. Maher, W. Mittig, F. Ndayisabye, S. Noji, S. J. Novario, J. Pereira, Z. Rahman, J. Schmitt, M. Serikow, L. J. Sun, J. Surbrook, N. Watwood, and T. Wheeler. β^+ Gamow-Teller Strengths from Unstable ^{14}O via the (d,^{2} He) Reaction in Inverse Kinematics. *Phys. Rev. Lett.*, 130:232301, 2023.

[70] Z. Rahman, S. Giraud, J. C. Zamora, R. G. T. Zegers, Y. Ayyad, S. Beceiro-Novo, D. Bazin, B. A. Brown, A. Carls, J. Chen, M. Cortesi, M. DeNudt, C. Maher, W. Mittig, F. Ndayisabye, S. Noji, J. Pereira, J. Schmitt, M. Z. Serikow, L. J. Sun, J. Surbrook, N. Watwood, and T. Wheeler. Extraction of Gamow-Teller strengths in the β^+ direction with the (d,^{2} He) reaction in inverse kinematics. *Phys. Rev. C*, 110:024313, 2024.

[71] H. Ohnuma, K. Hatanaka, S. I. Hayakawa, M. Hosaka, T. Ichihara, S. Ishida, S. Kato, T. Niizeki, M. Ohura, H. Okamura, H. Orihara, H. Sakai, H. Shimizu, Y. Tajima, H. Toyokawa, H. Y. Yoshida, and M. Yosoi. (d,^{2}He) reactions at E_d=260 MeV as a possible probe to nuclear spin-isospin excitation. *Phys. Rev. C*, 47:648–651, 1993.

[72] H. M. Xu, G. K. Ajupova, A. C. Betker, C. A. Gagliardi, B. Kokenge, Y.-W. Lui, and A. F. Zaruba. (d,^{2}He) reactions at E_d=125.2 MeV. *Phys. Rev. C*, 52:R1161–R1165, 1995.

[73] D. Frekers and M. Alanssari. Charge-exchange reactions and the quest for resolution. *Eur. Phys. J.*, 54:177, 2018.

[74] S. Kox, J. Carbonell, C. Furget, T. Motobayashi, C. Perrin, C. Wilkin, J. Arvieux, J.P. Bocquet, A. Boudard, G. Gaillard, M. Garçon, L. Ghedira, G. Guillaume, F. Merchez, D. Rebreyend, and J. Yonnet. Cross section and deuteron analysing powers of the ^{1}H(d, 2p)n reaction at 200 and 350 MeV. *Nucl. Phys. A*, 556(4):621–640, 1993.

[75] A. M. Hernandez and W. W. Daehnick. Gamow-Teller strength in the ^{14}O→ ^{14}N(3.948 MeV) beta decay. *Phys. Rev. C*, 24:2235–2239, 1981.

[76] H. S. Wilson, R. W. Kavanagh, and F. M. Mann. Gamow-Teller transitions in some intermediate-mass nuclei. *Phys. Rev. C*, 22:1696–1722, 1980.

[77] R. G. T. Zegers, H. Akimune, Sam M. Austin, D. Bazin, A. M.van den Berg, G. P. A. Berg, B. A. Brown, J. Brown, A. L. Cole, I. Daito, Y. Fujita, M. Fujiwara, S. Galès, M. N. Harakeh, H. Hashimoto, R. Hayami, G. W. Hitt, M. E. Howard, M. Itoh, J. Jänecke, T. Kawabata, K. Kawase, M. Kinoshita, T. Nakamura, K. Nakanishi, S. Nakayama, S. Okumura, W. A. Richter, D. A. Roberts, B. M. Sherrill, Y. Shimbara, M. Steiner, M. Uchida, H. Ueno, T. Yamagata, and M. Yosoi. The (t,^{3}He) and (^{3}He, t) reactions as probes of Gamow-Teller strength. *Phys. Rev. C*, 74:024309, 2006.

[78] H. Fujimura, H. Akimune, I. Daito, M. Fujiwara, K. Hara, K. Y. Hara, M. N. Harakeh, F. Ihara, T. Inomata, K. Ishibashi, T. Ishikawa, T. Kawabata, A. Tamii, M. Tanaka, H. Toyokawa, T. Yamanaka, and M. Yosoi. Nuclear structure of the spin-isospin excited states in ^{13}N studied via the (^{3}He, t) and (^{3}He, tp) reactions at 450 MeV. *Phys. Rev. C*, 69:064327, 2004.

[79] R. G. T. Zegers, E. F. Brown, H. Akimune, S. M. Austin, A. M. V. den Berg, B. A. Brown, Y. Chamulak, D. A. Fujita, M. Fujiwara, S. Galés, M. N. Harakeh, H. Hashimoto, R. Hayami, G. W. Hitt, M. Itoh, T. Kawabata, K. Kawase, M. Kinoshita, K. Nakanishi, S. Nakayama, S. Okamura, Y. Shimbura, M. Uchida, H. Ueno, T. Yamagata, and M. Yosoi. Gamow-Teller strength for the analog transitions to the first T=1/2, $J^\pi = 3/2^-$ states in ^{13}C and ^{14}N and the implications for type Ia Supernovae. *Phys. Rev. C*, 77:024307, 2008.

[80] B. Bonin, N. Alamanos, B. Berthier, G. Bruge, H. Faraggi, D. Legrand, J. C. Lugol, W. Mittig, L. Papineau, A. I. Yavin, et al. Response functions of ^{58}Ni,^{116}Sn AND ^{208}Pb to the excitation of intermediate-energy -particles. *Nucl. Phys. A*, 430(2):349–396, 1984.

[81] M. A. Moinester, A. Trudel, K. Raywood, S. Yen, B. M. Spicer, R. Abegg, W. P. Alford, N. Auerbach, A. Celler, D. Frekers, et al. A study of spin isovector giant resonances with the^{208}Pb(n, p)^{208}Tl reaction. *Phys. Lett. B*, 230(1):41–45, 1989.

[82] B. A. Brown and W. D. M. Rae. The Shell-Model Code NuShellX@MSU. *Nucl. Data Sheets*, 120:115–118, 2014.

[83] M. A. Hofstee, S .Y. van der Werf, A. M. van den Berg, N. Blasi, J. A. Bordewijk, W. T. A. Borghols, R. De Leo, G. T. Emery, S. Fortier, S. Galès, M. N. Harakeh, P. den Heijer, C. W. de Jager, H. Langevin-Joliot, S. Micheletti, M. Morlet, M. Pignanelli, J. M. Schippers, H. de Vries, A. Willis, and A. van der Woude. Localized 1 particle-hole strength in nuclei. *Nucl. Phys. A*, 588(3):729–766, 1995.

[84] H. Okamura. Three-body treatment of the (d,^{2}He) reaction on the basis of the adiabatic approximation. *Phys. Rev. C*, 60:064602, 1999.

[85] B. A. Brown. Lecture Notes on Nuclear Physics. `http://nuclear.fis.ucm.es/PDFN/documentos/BAB-lecture-notes-NUCLEAR-PHYSICS.pdf`, Year.

[86] A. Poves and J. Retamosa. The onset of deformation at the N = 20 neutron shell closure far from stability. *Phys. Lett. B*, 184(4):311–315, 1987.

[87] N. Fukunishi, T. Otsuka, and T. Sebe. Vanishing of the shell gap in N = 20 neutron-rich nuclei. *Phys. Lett. B*, 296(3):279–284, 1992.

[88] E. Caurier, F. Nowacki, A. Poves, and J. Retamosa. Shell model study of the neutron rich isotopes from oxygen to silicon. *Phys. Rev. C*, 58:2033–2040, 1998.

[89] Y. Utsuno, T. Otsuka, T. Mizusaki, and M. Honma. Varying shell gap and deformation in N∼20 unstable nuclei studied by the Monte Carlo shell model. *Phys. Rev. C*, 60:054315, 1999.

[90] Y. Utsuno, 2024. Private communication.

[91] S. Y. van der Werf. computer program NORMOD, unpublished.

[92] R. G. T. Zegers. *Search for Isovector Giant Monopole Resonances*. PhD thesis, Rijksuniversiteit Groningen, 1999.

[93] H. Okamura, S. Fujita, Y. Hara, K. Hatanaka, T. Ichihara, S. Ishida, K. Katoh, T. Niizeki, H. Ohnuma, H. Otsu, H. Sakai, N. Sakamoto, Y. Satou, T. Uesaka, T. Wakasa, and T. Yamashita. Tensor analyzing power of the (d, ^{2}He) reaction at 270 MeV. *Phys. Lett. B*, 345(1):1–5, 1995.

[94] A. J. Koning and J. P. Delaroche. Local and global nucleon optical models from 1 keV to 200 MeV. *Nucl. Phys. A*, 713(3):231–310, 2003.

[95] A. J. Koning, S. Hilaire, and M. C. Duijvestijn. Talys-1.0. In *International Conference on Nuclear Data for Science and Technology*, pages 211–214, 2007.

[96] M. A. Franey and W. G. Love. Nucleon-nucleon t-matrix interaction for scattering at intermediate energies. *Phys. Rev. C*, 31:488–498, 1985.

[97] M. Hausmann, A. M. Aaron, A. M. Amthor, M. Avilov, L. Bandura, R. Bennett, G. Bollen, T. Borden, T. W. Burgess, S. S. Chouhan, V. B. Graves, W. Mittig, D. J. Morrissey, F. Pellemoine, M. Portillo, R. M. Ronningen, M. Schein, B. M. Sherrill, and A. Zeller. Design of the Advanced Rare Isotope Separator ARIS at FRIB. *Nucl. Instrum. Methods Phys. Res. B*, 317:349–353, 2013. XVIth International Conference on ElectroMagnetic Isotope Separators and Techniques Related to their Applications, December 2–7, 2012 at Matsue, Japan.

[98] D. J. Morrissey, B. M. Sherrill, M. Steiner, A. Stolz, and I. Wiedenhoever. Commissioning the A1900 projectile fragment separator. *Nucl. Instrum. Methods Phys. Res. B*, 204:90–96, 2003. 14th International Conference on Electromagnetic Isotope Separators and Techniques Related to their Applications.

[99] D. Bazin, J. A. Caggiano, B. M. Sherrill, J. Yurkon, and A. Zeller. The S800 spectrograph. *Nucl. Instrum. Methods Phys. Res. B*, 204:629–633, 2003. 14th International Conference on Electromagnetic Isotope Separators and Techniques Related to their Applications.

[100] K. C. Meierbachtol. *Parallel and Perpendicular Momentum Distributions in Projectile Fragmentation Reactions*. PhD thesis, Michigan State University, 2012.

[101] J. Yurkon, D. Bazin, W. Benenson, D. J. Morrissey, B. M Sherrill, D. Swan, and R. Swanson. Focal plane detector for the S800 high-resolution spectrometer. *Nucl. Instrum. Methods Phys. Res. A.*, 422(1):291–295, 1999.

[102] G. W. Hitt. *The ^{64}Zn(t,^{3}He) Charge-Exchange Reaction at 115 MeV Per Nucleon and Application to ^{64}Zn Stellar Electron-Capture*. PhD thesis, Michigan State Univeristy, 2008.

[103] G. F. Knoll. *Radiation Detection and Measurement, vol.3*. John Wiley and Sons, 2010.

[104] Y. Ayyad, N. Abgrall, T. Ahn, H. Álvarez Pol, D. Bazin, S. Beceiro-Novo, L. Carpenter, R. J. Cooper, M. Cortesi, A.O. Macchiavelli, W. Mittig, B. Olaizola, J.S. Randhawa, C. Santamaria, N. Watwood, J. C. Zamora, and R. G. T. Zegers. Next-generation experiments with the Active Target Time Projection Chamber (AT-TPC). *Nucl. Instrum. Methods Phys. Res. A.*, 954:161341, 2020. Symposium on Radiation Measurements and Applications XVII.

[105] E. Pollacco, S. Anvar, H. Baba, P. Baron, D. Bazin, C. Belkhiria, B. Blank, J. Chavas, P. Chomaz, E. Delagnes, F. Druillole, P. Hellmuth, C. Huss, E. Galyaev, B. Lynch, W. Mittig, T. Murakami, L. Nalpas, J-L Pedroza, R. Raabe, J. Pibernat, B. Raine, A. Rebii, A. Taketani, F. Saillant, D. Suzuki, N. Usher, and G. Wittwer. GET: A Generic Electronic System for TPCs for Nuclear Physics Experiments. *Physics Procedia*, 37:1799–1804, 2012. Proceedings of the 2nd International Conference on Technology and Instrumentation in Particle Physics (TIPP 2011).

[106] S. Anvar, P. Baron, B. Blank, J. Chavas, E. Delagnes, F. Druillole, P. Hellmuth, L. Nalpas, J-L Pedroza, J. Pibernat, E. Pollacco, A. Rebii, and N. Usher. AGET, the GET front-end ASIC, for the readout of the Time Projection Chambers used in nuclear physic experiments. 2011.

[107] J. W. Bradt. *Measurement of Isobaric Analogue Resonances of ^{47}Ar With the Active-Target Time Projection Chamber*. PhD thesis, Michigan State University, 2017.

[108] J. S. Randhawa, M. Cortesi, Y. Ayyad, W. Mittig, T. Ahn, D. Bazin, S. Beceiro-Novo, L. Carpenter, K. J. Cook, M. Dasgupta, S. Henderson, D. J. Hinde, J. J. Kolata, J. Sammut, C. Santamaria, N. Watwood, and A. Yeck. Beam-induced space-charge effects in time projection chambers in low-energy nuclear physics experiments. *Nucl. Instrum. Methods Phys. Res. A.*, 948:162830, 2019.

[109] S. Giraud, J. C. Zamora, R. G. T. Zegers, Y. Ayyad, D. Bazin, W. Mittig, A. Carls, M. DeNudt, and Z. Rahman. Simulations and analysis tools for charge-exchange (d, ^{2}He) reactions in inverse kinematics with the AT-TPC. *Nucl. Instrum. Methods Phys. Res. A.*, 1051:168213, 2023.

[110] M. Berz, K. Joh, J. A. Nolen, B. M. Sherrill, and A. F. Zeller. Reconstructive correction of aberrations in nuclear particle spectrographs. *Phys. Rev. C*, 47:537–544, 1993.

[111] O. B. Tarasov and D. Bazin. LISE^{++}: Exotic beam production with fragment separators and their design. *Nucl. Instrum. Methods Phys. Res. B*, 376:185–187, 2016. Proceedings of the XVIIth International Conference on Electromagnetic Isotope Separators and Related Topics (EMIS2015), Grand Rapids, MI, U.S.A., 11-15 May 2015.

[112] J. C. Zamora and G. F. Fortino. Tracking algorithms for TPCs using consensus-based robust estimators. *Nucl. Instrum. Methods Phys. Res. A.*, 988:164899, 2021.

[113] A. K. Anthony. *Fission in the Lead Region*. PhD thesis, Michigan State University, 2023.

[114] S. F. Biagi. A multiterm Boltzmann analysis of drift velocity, diffusion, gain and magnetic-field effects in argon-methane-water-vapour mixtures. *Nucl. Instrum. Methods Phys. Res. A.*, 283(3):716–722, 1989.

[115] Y. Ayyad, W. Mittig, D. Bazin, and M. Cortesi. Overview of the data analysis and new micro-pattern gas detector development for the Active Target Time Projection Chamber (AT-TPC) project. *Journal of Physics: Conference Series*, 876(1):012003, 2017.

[116] Y. Ayyad. ATTPCROOT. `https://github.com/ATTPC/ATTPCROOTv2`, 2022.

[117] FAIRROOT Framework. `https://github.com/FairRootGroup/FairRoot`, 2022.

[118] J. F. Ziegler, M. D. Ziegler, and J. P. Biersack. SRIM – The stopping and range of ions in matter (2010). *Nucl. Instrum. Methods Phys. Res. B*, 268(11):1818–1823, 2010. 19th International Conference on Ion Beam Analysis.

[119] National Nuclear Data Center. Evaluated Nuclear Structure Data File (ENSDF), URL: `https://www.nndc.bnl.gov/ensdf`, 2025. Accessed: 2025-03-20.

[120] E. W. Grewe, C. Bäumer, A. M. van den Berg, N. Blasi, B. Davids, D. De Frenne, D. Frekers, P. Haefner, M. N. Harakeh, M. Huynyadi, E. Jacobs, B. Junk, A. Korff, A. Negret, P. von Neumann-Cosel, L. Popescu, S. Rakers, and H. J. Wörtche. Gamow-Teller transitions to ^{32}P studied through the ^{32}S(d,^{2} He) reaction at E_d = 170 MeV. *Phys. Rev. C*, 69:064325, 2004.

[121] R. G. T. Zegers, T. Adachi, H. Akimune, Sam M. Austin, A. M. van den Berg, B. A. Brown, Y. Fujita, M. Fujiwara, S. Galès, C. J. Guess, M. N. Harakeh, H. Hashimoto, K. Hatanaka, R. Hayami, G. W. Hitt, M. E. Howard, M. Itoh, T. Kawabata, K. Kawase, M. Kinoshita, M. Matsubara, K. Nakanishi, S. Nakayama, S. Okumura, T. Ohta, Y. Sakemi, Y. Shimbara, Y. Shimizu, C. Scholl, C. Simenel, Y. Tameshige, A. Tamii, M. Uchida, T. Yamagata, and M. Yosoi. Extraction of Weak Transition Strengths via the (^{3}He, t) Reaction at 420 MeV. *Phys. Rev. Lett.*, 99:202501, 2007.

[122] B. A. Brown and W. A. Richter. New "USD" Hamiltonians for the *sd* shell. *Phys. Rev. C*, 74:034315, 2006.

[123] M. Honma, T. Otsuka, B. A. Brown, and T. Mizusaki. Effective interaction for pf-shell nuclei. *Phys. Rev. C*, 65:061301, 2002.

[124] N. E. White and F. E. Marshall. The unusually soft X-ray spectrum of LMC X-3. *Astrophys. J.*, 281:354–359, 1984.

[125] E. F. Brown. Nuclear Heating and Melted Layers in the Inner Crust of an Accreting Neutron Star. *Astrophys. J.*, 531(2):988, 2000.

[126] P. Haensel, A. D. Kaminker, and D. G. Yakovlev. Electron neutrino-antineutrino bremsstrahlung in a liquid phase of neutron star crusts. *Astron. Astrophys.*, 314:328–340, 1996.

[127] S. Gupta, E. F. Brown, H. Schatz, P. Möller, and K.-L. Kratz. Heating in the Accreted Neutron Star Ocean: Implications for Superburst Ignition. *Astrophys. J.*, 662(2):1188, 2007.

[128] C. Iliadis. *Nuclear Physics of Stars*. WILEY-VCH Verlag GmbH & Co. KGaA, 2007.

[129] P. Moller, J. R. Nix, W. D. Myers, and W. J. Swiatecki. Nuclear Ground-State Masses and Deformations. *At. Data Nucl. Data Tables*, 59(2):185–381, 1995.

[130] CERN. Geneva. *3rd International Conference on Nuclei Far from Stability*, volume CERN Yellow Reports: Conference Proceedings, Cargese, France, 1976. CERN. CC-BY-3.0.

[131] R. Lau, M. Beard, S. S. Gupta, H. Schatz, A. V. Afanasjev, E. F. Brown, A. Deibel, L. R. Gasques, G. W. Hitt, W. R. Hix, L. Keek, P. Möller, P. S. Shternin, A. W. Steiner, M. Wiescher, and Y. Xu. Nuclear Reactions in the Crusts of Accreting Neutron Stars. *Astrophys. J.*, 859(1):62, 2018.

[132] L. Valdez. *Electrion-captures in Supernovae*. PhD thesis, Michigan State University, 2012.

[133] H. Schatz, L. Bildsten, A. Cumming, and M. Ouellette. Nuclear physics in normal X-ray bursts and superblasts. *Nucl. Phys. A*, 718:247–254, 2003.

[134] M. Scott, Y. Shimbara, Sam M. Austin, D. Bazin, B. A. Brown, J. M. Deaven, Y. Fujita, C. J. Guess, S. Gupta, G. W. Hitt, D. Koeppe, R. Meharchand, M. Nagashima, G. Perdikakis, A. Prinke, M. Sasano, C. Sullivan, L. Valdez, and R. G. T. Zegers. Gamow-Teller transition strengths from ^{56}Fe extracted from the ^{56}Fe(t,^{3} He) reaction. *Phys. Rev. C*, 90:025801, 2014.